Title
Hadronic Production of J/psi at Large x{sub F} in 800 GeV p+Cu and p+Be Collisions

Author
Kowitt, M.S.

Publication Date
1992-12-01

LBL-33331
UC-414

Lawrence Berkeley Laboratory
UNIVERSITY OF CALIFORNIA

Physics Division

Hadronic Production of J/ψ at Large x_F in 800 GeV p+Cu and p+Be Collisions

M.S. Kowitt
(Ph.D. Thesis)

December 1992

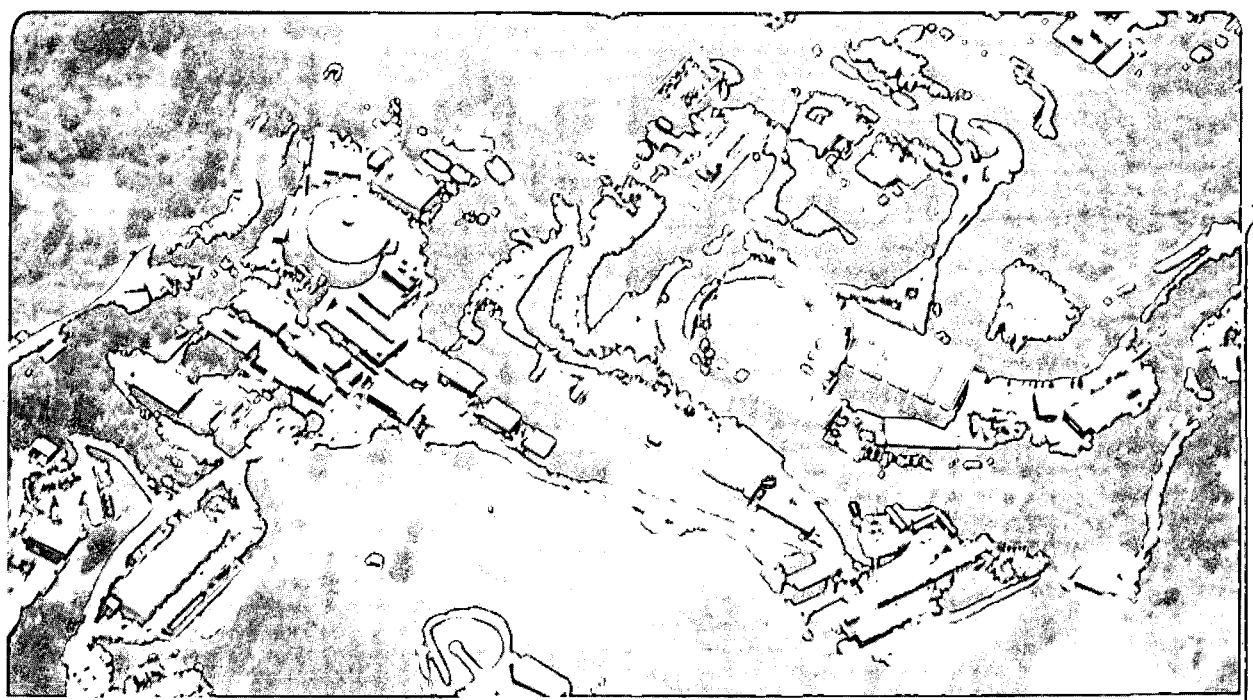

Prepared for the U.S. Department of Energy under Contract Number DE-AC03-76SF00098

DISCLAIMER

LBL-33331
UC-414

HADRONIC PRODUCTION OF J/ψ AT LARGE x_F IN 800 GeV p+Cu AND p+Be COLLISIONS

MATTHEW SCOTT KOWITT
Ph.D. Thesis

DEPARTMENT OF PHYSICS
University of California

and

PHYSICS DIVISION
Lawrence Berkeley Laboratory
University of California
Berkeley, CA 94720

December 1992

This work was supported by the Director, Office of Energy Research, Office of High Energy and Nuclear Physics, Division of High Energy Physics, of the U.S. Department of Energy under Contract No. DE-AC03-76SF00098.

Abstract

Hadronic Production of J/ψ at Large x_F in 800 GeV p+Cu and p+Be Collisions

by

Matthew Scott Kowitt
Doctor of Philosophy in Physics
University of California at Berkeley
Professor Kam-Biu Luk, Chair

The differential cross-section $d\sigma/dx_F$ for J/ψ production in 800 GeV proton-nucleus collisions has been measured in the kinematic range $0.30 \leq x_F \leq 0.95$ and $0 < p_\perp < 5$ GeV through the decay mode $J/\psi \rightarrow \mu^+\mu^-$. The nuclear dependence of J/ψ production over this range was measured using copper and beryllium targets. The differential cross sections are in good agreement with the predictions of the semilocal parton duality model. The data show no evidence for an intrinsic charm component in the proton. The ratio of the differential cross sections for copper and beryllium shows a suppression of J/ψ production in copper which increases with increasing x_F.

CONTENTS

List of Figures

List of Tables

ACKNOWLEDGEMENTS

First off, I would like to thank my thesis advisor, Kam-Biu Luk. His intense enthusiasm for physics is quite contagious, and has reinforced my own dedication to this business. His scientific standards are impeccable, and it would be a pleasure to collaborate in the future. It is an honor to be his first thesis student.

Fermilab Experiment 789 was a collaboration of over 40 physicists, all of whom contributed materially to this work. In particular, I would like to thank Chuck Brown for suggesting this thesis topic to me. His physical insights always helped to steer me away from nonsense. Pat McGaughey prepared the trigger matrix file used for this study, and offered many helpful suggestions during the analysis. I also want to thank George Gidal for many useful discussions throughout the analysis.

It was a great pleasure to work together with Tom Carey and Pak-Ming Ho on the data-acquisition upgrade project. We worked intensely and got the job done. Without that upgrade this thesis would not have been possible.

Before coming to work on E789, I spent two and a half years working on the Compton Polarimeter project at the S.L.C. I would like to thank my previous advisor, Herbert Steiner, for introducing me to real experimental physics. I learned a great deal of physics working with Herb, as well as with the other members of that team. I would particularly like to thank Max Zolotorev for many wonderful hours of working together. He helped to show me what a physicist is, and taught me the seemingly obvious lesson that in experimental physics, the goal is always to obtain the result. I wish him the best successes in the future, and look forward to the day when we

might work together again. I would also like to thank Ray Fuzesy, for teaching me things I couldn't have learned from a textbook.

I want to thank my committee members, Kam-Biu Luk, Herb Steiner, and Selig Kaplan, as well as George Gidal, for reading the earlier versions of this dissertation. Their helpful suggestions substantially improved what you are now holding.

In the $6\frac{1}{2}$ years since I first arrived at Berkeley, many things have changed. Some things, however, have remained the same. One of the constants of my graduate school career has been Dave Pripstein. From our early days as teaching assistants, through all of the trials and travails at SLAC, to midnight shifts in the cold Illinois winter, Dave and I have worked together. Yet despite Dave's best efforts, I still do not exercise or eat right. Oh well...

I am grateful to my friends—on both coasts—for helping me to keep in touch with reality while I've been off on this adventure in higher education. Despite the fact that I often dropped in unannounced, they always took me in and we picked up where ever we had left off.

Special thanks go to my in-laws, Les and Diane Inman, who graciously housed and fed me over the past year, and more importantly gave me a family to come home to every night.

My parents have my total gratitude for the 28 years of support and love they have given me. Well, I'm finally out of school (although I know you thought the day would never arrive). I guess I have to get a job now!

Finally, I want to thank my wife, Casey. Her love and encouragement, even from 3000 miles away, made it all possible. I'm looking forward to giving her the same support on her dissertation. Even more, I'm looking forward to finally settling down and living together, on the same side of the continent, for more than a week at a time. This thesis is dedicated to her.

CHAPTER 1

INTRODUCTION

In early November, 1974, the world of particle physics changed. Simultaneously at Brookhaven National Laboratory and the Stanford Linear Accelerator Center, groups led by Samuel Ting and Burton Richter independently discovered an exceedingly narrow resonance, with a mass of 3.097 GeV[1], which coupled to e^+e^- pairs [1,2]. Named J by Ting's MIT-Brookhaven collaboration, and ψ by Richter's SLAC-LBL collaboration, this particle (still referred to by the compound name J/ψ) was quickly established as the $1\,^3S_1$ bound state of a heavy quark-antiquark system, in analogy to positronium. More spectroscopic states were soon discovered, including the $2\,^3S_1$ state ψ' with a mass of 3.685 GeV, and three intermediate P-states denoted χ. Several years later, the discovery of open charmed mesons confirmed the interpretation of the heavy resonances—now collectively called charmonium—as being bound states of the charm quark first predicted by Bjørken and Glashow [3]. With the discovery of charm, the second generation of the Standard Model of Particle Physics was completed [4].

[1]Throughout this dissertation, we will employ units where $\hbar = c = 1$.

1.1 Hadronic Production

Starting with the discovery of charm, production of J/ψ by hadrons has remained an ongoing field of study. The large cross section for hadronic production of heavy quarks at high energies makes this technique appealing for studying both open and hidden charm and beauty physics. Also, heavy quark production can be understood at the parton level, making it a useful probe for investigating the internal structure of hadrons.

We will begin by considering the QCD-parton description of charm production. The formalism of the semilocal parton duality model will be developed in order to calculate the predicted J/ψ production cross section. Following that, various models for the nuclear dependence of J/ψ production will also be discussed.

1.1.1 Parton Model of Charm Production

Hadronic production of J/ψ can be understood in the context of quantum chromodynamics (QCD) together with the parton model of hadronic structure. At the energy scale $Q^2 = m^2_{J/\psi}$, $m_{J/\psi}$ being the mass of the J/ψ, the strong coupling constant α_s is small enough ($\approx 0.2 - 0.3$) to apply QCD perturbatively. To the lowest order in α_s, there are two leading processes for charm production, quark-antiquark annihilation (Figure 1.1) and gluon-gluon fusion (Figure 1.2).

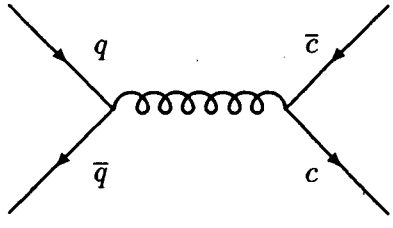

Figure 1.1: $q\bar{q}$ annihilation diagram

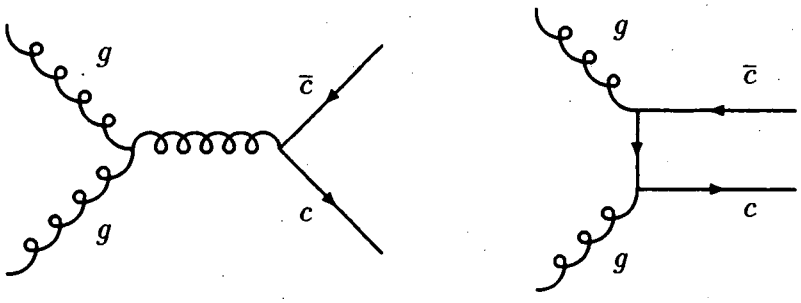

Figure 1.2: gg fusion diagrams

The QCD calculation of these diagrams gives the cross sections for producing a $c\bar{c}$ pair of mass m (averaged over initial spin and color) as

$$\hat{\sigma}(q\bar{q} \to c\bar{c}; m^2) = \frac{8\pi\alpha_s^2}{27m^6}(m^2 + 2m_c^2)\lambda \tag{1.1}$$

and

$$\hat{\sigma}(gg \to c\bar{c}; m^2) = \frac{\pi\alpha_s^2}{3m^6}\left\{(m^4 + 4m^2m_c^2 + m_c^4)\ln\left(\frac{m^2+\lambda}{m^2-\lambda}\right) - \frac{1}{4}(7m^2 + 31m_c^2)\lambda\right\} \tag{1.2}$$

where m_c is the charm quark mass and $\lambda^2 = m^4 - 4m^2m_c^2$ [5].

1.1.2 Semilocal Parton Duality

To make the connection between the parton-level reactions and a hadronic reaction such as $p+N \to J/\psi+X$, we first introduce parton distribution functions. Bjørken's x variable is used to parameterize the beam and target parton momenta—x_1 is the fraction of the beam hadron's momentum carried by a beam parton (formally in the infinite-momentum limit), while x_2 is the fraction of the target hadron's momentum carried by a target parton (again, formally in the infinite-momentum limit). x_1 and x_2 are both bounded between 0 and 1. The parton distribution functions $G_B(x_1), q_{Bi}(x_1), \bar{q}_{Bi}(x_1)$ are the probability densities for finding a gluon, a quark, or an antiquark with a momentum fraction x_1 in the beam hadron B (i

labels the quark flavor). Similarly, $G_T(x_2), q_{Ti}(x_2), \overline{q}_{Ti}(x_2)$ are the distributions for the partons in the target hadron T. The parton distribution functions evolve with the energy scale Q^2 of the reaction according to the Altarelli-Parisi QCD evolution equations [6]—here we fix the scale at $Q^2 = m^2_{J/\psi}$. We will use the recent parton distributions of Martin, Roberts, and Stirling, set S_0 [7,8]. This set of functions was tuned with newly available measurements of deep-inelastic scattering, giving a much more realistic behaviour at $x < 0.01$ than previously available parton distributions. Continuing as in Ref. 5, we can now construct a kernel from the parton-level cross sections and distribution functions,

$$H_{BT}(x_1, x_2, m^2) = G_B(x_1) G_T(x_2) \hat{\sigma}(gg \to c\bar{c}; m^2) + \sum_{i=u,d,s} \left(q_{Bi}(x_1)\overline{q}_{Ti}(x_2) + \overline{q}_{Bi}(x_1) q_{Ti}(x_2) \right) \hat{\sigma}(q\overline{q} \to c\bar{c}; m^2). \tag{1.3}$$

We now introduce the scaling variables $\tau = m^2/S$ and x_F, where S is the beam-target center-of-mass energy squared, and $x_F = p^*_L/(p^*_L)_{max}$ is the J/ψ longitudinal momentum divided by its maximum value in the beam-target center-of-mass frame. Assuming massless partons, but taking the finite J/ψ mass into account, we have the relations

$$x_1 - x_2 = x_F(1 - \tau) \approx x_F \tag{1.4}$$

and

$$x_1 x_2 = \tau = m^2/S. \tag{1.5}$$

Solving for x_1 and x_2,

$$x_{1,2} = \frac{1}{2} \left\{ \sqrt{x_F^2(1-\tau)^2 + 4\tau} \pm x_F(1-\tau) \right\}. \tag{1.6}$$

See Figure 1.3 for the values of x_1 and x_2 obtained from equation(1.6) for J/ψ production with 800 GeV protons.

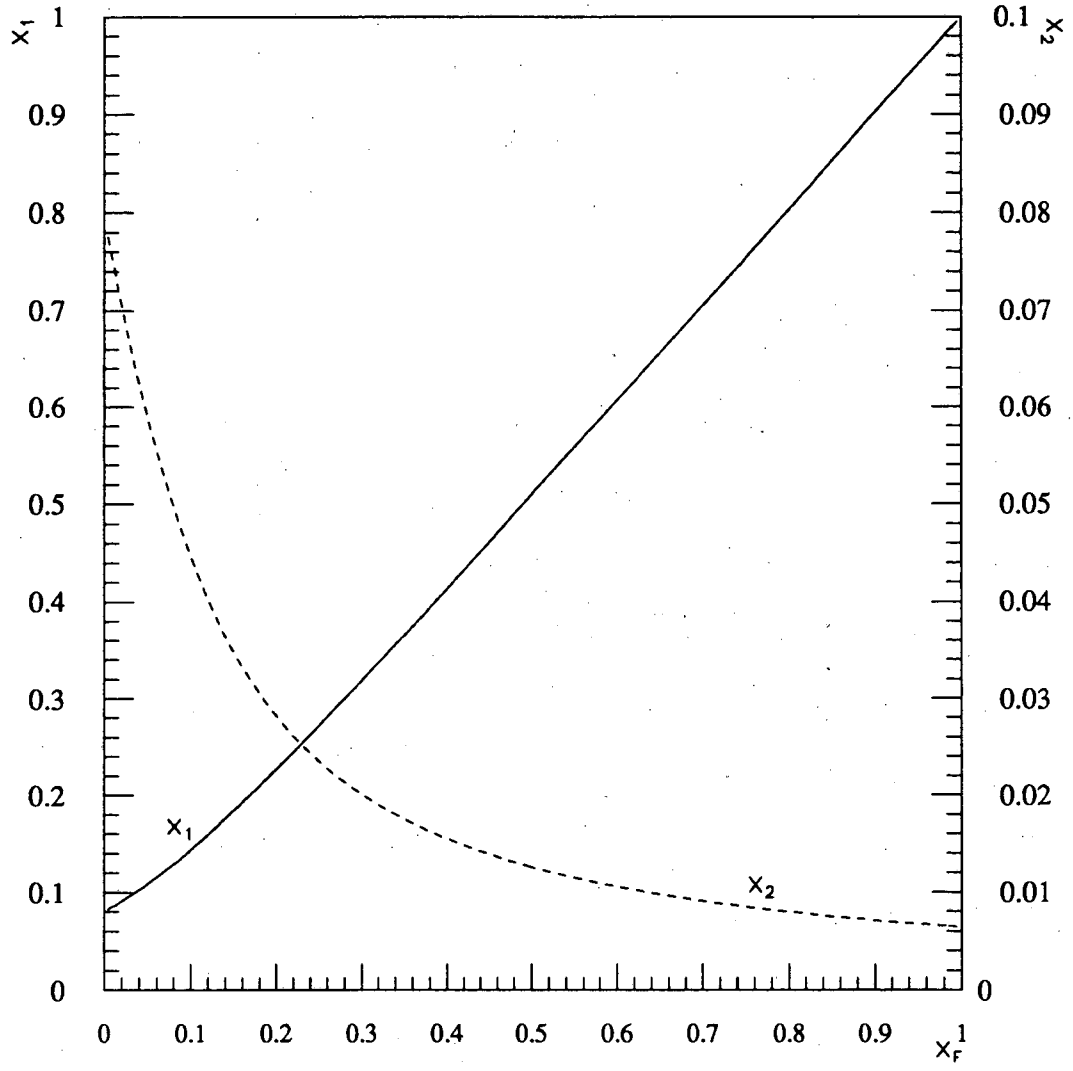

Figure 1.3: x_1 and x_2 versus x_F. The solid line shows x_1, while the dashed line shows x_2. Note the different axes for x_1 and x_2. x_1 and x_2 were calculated using equation (1.6) with $\tau = 0.0064 = m^2_{J/\psi}/S$.

The differential cross section for inclusive charm quark pair production in $B+T$ collisions is [5]

$$\frac{d\sigma}{dm^2 dx_F}(BT \to c\bar{c}X; S) = \frac{1-\tau}{S(x_1+x_2)} H_{BT}(x_1, x_2, m^2). \tag{1.7}$$

To go from equation (1.7) to a production cross section for charmonium, we use the semilocal parton duality hypothesis [9]. This scheme gives the physical cross section by integrating the charm quark production cross section from $m = 2m_c$, the bare quark production threshold, to the open charm threshold at $m = 2m_D = 2(1.86\text{GeV})$, where m_D is the mass of the D meson. A fixed fraction F of this integral is assumed to lead to J/ψ production, yielding

$$\frac{d\sigma}{dx_F}(BT \to J/\psi X; S) = F \int_{4m_c^2}^{4m_D^2} dm^2 \frac{d\sigma}{dm^2 dx_F}(BT \to c\bar{c}X; S). \tag{1.8}$$

Figure 1.4 shows the cross section obtained by equation (1.8) for an 800 GeV proton beam on a nucleon target. It is clear from the figure that gluon-gluon fusion is the dominant contribution to the total production cross section. However, at $x_F > 0.7$, the quark-antiquark annihilation channel becomes dominant. It is easy to understand this crossover in terms of the parton distribution functions and equation (1.6). As $x_F \to 1$, $x_1 \to \sim 1$. This corresponds to a beam parton carrying most of the momentum of the beam hadron. At values of Bjørken's x near 1, the valence quark contributions entirely dominate the parton distribution functions. Thus, the annihilation dominance predicted at large x_F is due to the beam *valence* quarks annihilating with the target sea antiquarks. The crossover point can shift slightly from $x_F = 0.7$ with other choices for the parton distribution functions. A similar crossover to annihilation dominance is expected in $\pi + N \to J/\psi$, although in that case the crossover is at $x_F \approx 0.85$, due to the harder gluon distribution in the pion.

It should be pointed out that the semilocal parton duality scheme does not directly treat the question of $c\bar{c}$ hadronization into the physical J/ψ state. Also, we

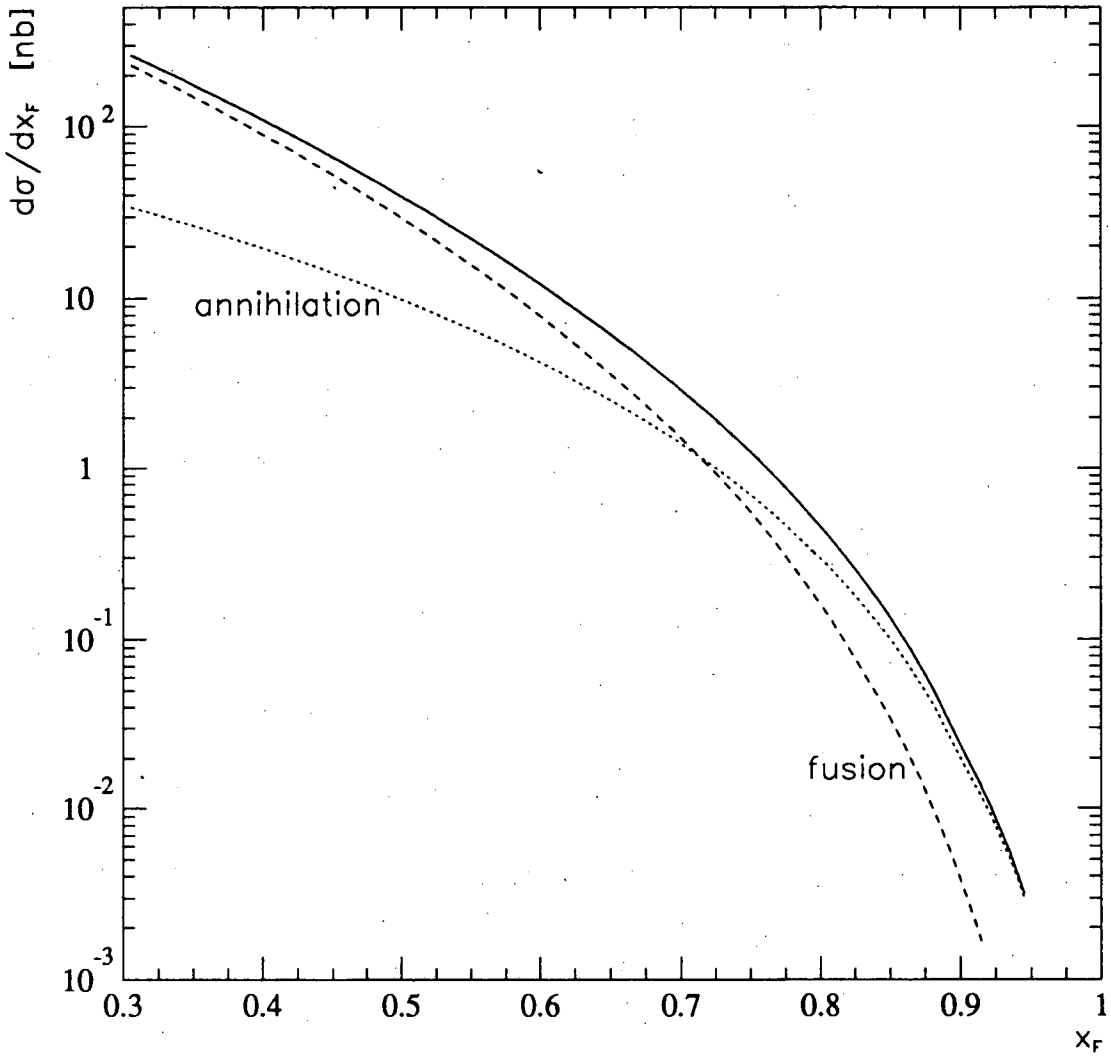

Figure 1.4: Parton model calculation of $d\sigma/dx_F(p + N \rightarrow J/\psi + X)$. The cross section is calculated from equation (1.8) with $F = 1/6$ and $m_c = 1.5$ GeV. A target isotopic ratio p:n of 4:5 is assumed. The solid curve shows the total production cross section, while the dashed line shows the gluon-gluon fusion contribution and the dotted line shows the quark-antiquark annihilation contribution. Notice the crossover to annihilation dominance at $x_F > 0.7$.

have not accounted for the indirect contribution to J/ψ production through decay of χ states—this has been estimated to account for as much as 30% of J/ψ production by protons [10]. The coefficient F in equation (1.8) must therefore be viewed as a tunable parameter of the model. Another important caveat is that the parton model offers no description of the transverse momentum, $p_\perp$, since the parton density functions introduced in equation (1.3) have effectively integrated over all parton transverse momenta [11]. Finally, it is important to recognize that the magnitude of the integral in equation (1.8) depends strongly on the value chosen for m_c, the charm quark mass. Varying m_c over the currently accepted range $1.3 < m_c < 1.7$ GeV [12], the magnitude of the integral varies by roughly a factor of 10. The shape of the distribution, however, is relatively unaffected by this choice. We will choose the central value of $m_c = 1.5$ GeV, but other choices require a further adjustment of F.

1.2 Nuclear Effects

The parton calculation of the previous section considers the case of hadron-nucleon production of J/ψ. Often, however, experiments are performed in which one (or both) colliding particles are atomic nuclei rather than bare hadrons. To a good approximation, the nuclear dependence of hard processes such as heavy quark production is a function only of the size of the nucleus, determined by the atomic number A. Hence, nuclear dependence is often referred to as "A–dependence."

Experimentally, J/ψ production (in fact, most particle production) is seen to be partially suppressed in heavy nuclei compared with nucleons. This is often expressed in terms of the ratio

$$R(A) = \frac{(1/A)d\sigma_A/dx_F}{(1/2)d\sigma_D/dx_F} \tag{1.9}$$

where, in general $R(A)$ is a function of x_F. A similar definition can be used for $d\sigma/dp_\perp$ or $d^2\sigma/dx_F dp_\perp$. Note that $R(A)$ is usually normalized to the deuterium cross section rather than the hydrogen cross section, since most nuclear targets A are nearly isoscalar. Another common parameterization of the A–dependence, which is at least partially supported by the experimental data [13], is

$$\frac{d\sigma_A}{dx_F} = \frac{d\sigma_0}{dx_F} A^\alpha, \tag{1.10}$$

where $d\sigma_0/dx_F$ is the bare nucleon cross section, and α characterizes the nuclear dependence. The limit of pure hard scattering with no nuclear effects is $\alpha = 1$, while the diffractive limit of $\alpha = 2/3$ gives a $d\sigma_A/dx_F$ which scales with the nuclear surface area. Any value $\alpha < 1$ corresponds to suppression in heavy nuclei. In general, α depends on kinematic variables such as x_F and $p_\perp$.

Models which attempt to explain the nuclear suppression of J/ψ production generally fall into two categories based on the x_F region they address. At low and negative x_F, the $c\bar{c}$ spends a relatively long time in the nuclear medium. Final state effects are usually invoked in this region, in which nuclear material somehow disrupts the charmonium state. We will discuss these models only very briefly, since we are focusing on large x_F production.

At large values of x_F, the $c\bar{c}$ state emerges from the nucleus well before it has hadronized into a J/ψ, and so initial state nuclear modifications to the parton distribution functions have been proposed. Alternate production mechanisms, speculated to dominate at the largest values of x_F, have also been proposed to explain the large x_F behavior.

1.2.1 SUPPRESSION AT LOW x_F—FINAL STATE INTERACTIONS

Most of the models proposed to explain low x_F suppression rely on final state interactions between the produced J/ψ and the nucleus or comoving nuclear fragments, and explain the suppression of charmonium in terms of disrupting the $c\bar{c}$ system into an open pair of charmed hadrons (such as D or Λ_c). Some combination of nuclear absorption and comover interactions might be required to describe the observed suppression.

These models may be ruled out soon, however, due to new results on nuclear suppression of open charm production at low and negative x_F which seem to show the *same* suppression with A as seen in charmonium production [14].

1.2.2 SUPPRESSION AT HIGH x_F—PARTON SHADOWING

At large values of x_F, initial state effects can explain the nuclear suppression of J/ψ production. The most straightforward effect is due to nuclear shadowing of low-x gluons and sea-quarks in the nucleus. From equation (1.6), we can see that production at large x_F corresponds to values of x_2 near zero. At low x_2, the target partons have low momenta and therefore large de Broglie wavelengths. When the parton wavelength exceeds the nucleon size, partons from neighboring nucleons within the nucleus start to overlap and interact. This effect is maximized when the parton wavelength grows to the size of the entire nucleus.

We will use an empirical estimate of this effect to relate the effective parton distribution functions in a nucleus to those of the nucleon [15]. Thus,

$$(1/A)x_2G^A(x_2) = x_2G(x_2)R_g(x_2, A) \tag{1.11}$$

$$(1/A)x_2q_s^A(x_2) = x_2q_s(x_2)R_s(x_2, A) \tag{1.12}$$

where G^A and q_s^A are the gluon and sea-quark distribution functions inside nucleus A, G and q_s are the gluon and sea-quark distribution functions inside the bare nucleon, and R_g and R_s fully describe the shadowing in A as a function of x_2.

If the momentum per nucleon of a nucleus is p, then the longitudinal size for a nucleus of proper radius $R_A = rA^{2/3}$ is Lorentz contracted to $\Delta z \approx 2R_A m_p/p$. Similarly, the longitudinal size of a constituent nucleon of radius r (=1.3 fm) is contracted to $\Delta z \approx 2rm_p/p$. The longitudinal size of a sea parton with momentum fraction x_2 is $\Delta z \approx 1/k_z = 1/(x_2 p)$. Eliminating p from these expressions, we now see that shadowing should begin when the partons from different nucleons within the nucleus begin to overlap,

$$x_2 < \frac{1}{2rm_p} \equiv x_n = 0.081 \tag{1.13}$$

and should saturate when they fill the entire volume of the nucleus,

$$x_2 < \frac{1}{2R_A m_p} \equiv x_A. \tag{1.14}$$

We quantify this with an *ad hoc* parton overlap function, R_{over}, defined in Ref. 15 as

$$R_{over} = \begin{cases} 0 & x_n < x_2 < 1 \\ \frac{1/x_2 - 1/x_n}{1/x_A - 1/x_n} & x_A < x_2 < x_n \\ 1 & 0 < x_2 < x_A \end{cases} \tag{1.15}$$

We take the A-dependence of parton shadowing as approximately $A^{1/3} - 1$ based on parton evolution corrections, and obtain the parton shadowing as

$$R_{s,g}(x_2, A) = 1 - K_{s,g}(A^{1/3} - 1)R_{over}. \tag{1.16}$$

We take the values $K_s = 0.1$ and $K_g = 0.05$ as determined in References 15 and 16, respectively. Figure 1.5 shows the predicted α obtained from this model of parton shadowing, based on calculations for p+Cu $\rightarrow J/\psi$ and p+Be $\rightarrow J/\psi$ using equation (1.8).

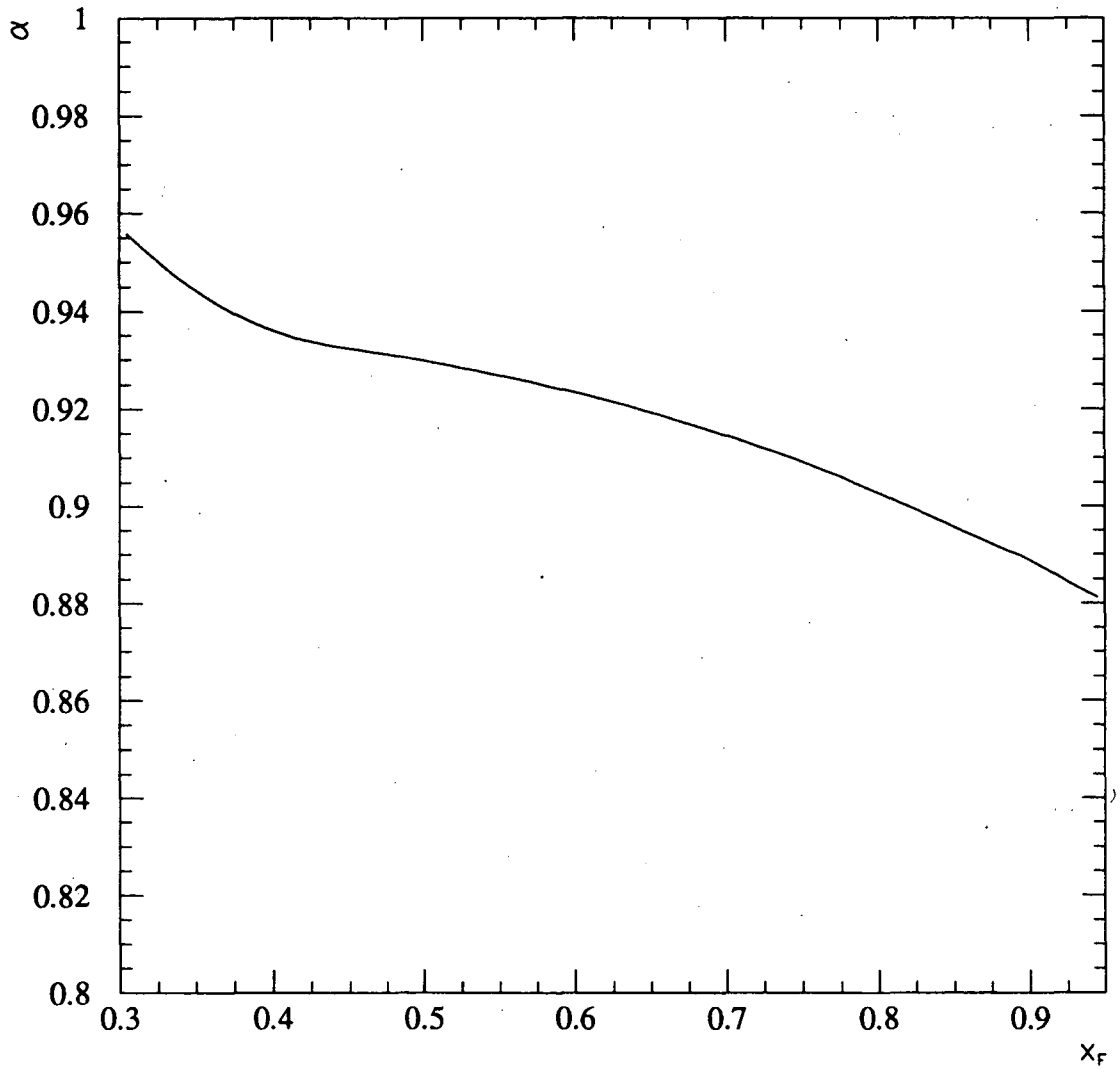

Figure 1.5: A–dependence of J/ψ production predicted by target parton shadowing. Assuming $d\sigma/dx_F \propto A^\alpha$, the prediction was determined by a semilocal duality calculation for p+Cu and p+Be collisions. MRS set S_0 parton distribution functions were used, with target distribution functions modified according to equations (1.11) and (1.12).

1.2.3 Intrinsic Charm

An additional contribution to J/ψ production at large x_F which has been proposed to explain nuclear suppression is the intrinsic charm model [16–19]. In this framework, virtual $c\bar{c}$ fluctuations in the beam hadron wavefunction are materialized into physical charmonium states due to soft interactions between the target nucleus and the remaining beam partons. Quantum fluctuations of $c\bar{c}$ will be suppressed due to the large charm quark mass, so that $c\bar{c}$ constitutes only a small fraction of the total hadron wavefunction. However, kinematical arguments require the $c\bar{c}$ fluctuations to carry a large fraction of the beam momentum during their brief existence—thus, any physical charm produced from this intrinsic charm component is expected to emerge at large x_F.

This has been quantified in terms of a Fock state wave function for the intrinsic charm state of the proton, $|uudc\bar{c}\rangle$ [16]. Based on that treatment, the x_F distribution of the $c\bar{c}$ state within the proton was calculated to be

$$\frac{d\sigma_{IC}}{dx_F} = N_5 x_F^3 (1-x_F)^4 \int_0^1 \prod_{i=1}^{3} dy_i (1-y_2) \left[x_F(1-x_F)m_p^2 - \frac{(1-x_F)\widehat{m}_c^2}{y_3(1-y_3)} - x_F \widehat{m}_q^2 \left(\frac{1}{y_2} + \frac{1}{y_1(1-y_2)} + \frac{1}{(1-y_1)(1-y_2)} \right) \right]^{-2} \quad (1.17)$$

where N_5 is the normalization for the 5–quark proton state $|uudc\bar{c}\rangle$, m_p is the proton mass, $\widehat{m}_q = 0.45$ GeV is the effective constituent valence quark mass, and $\widehat{m}_c = 1.8$ GeV is the effective constituent charm quark mass of the theory.

The A–dependence that is predicted from the intrinsic charm model is based on the hardness of the distribution predicted by equation (1.17). Since the parton momenta must add up to the total proton momentum ($\sum_i x_i = 1$) and the $c\bar{c}$ is expected to occur at large x, during a fluctuation into the $|uudc\bar{c}\rangle$ state, the non-charmed partons (including the valence quarks) will tend to be soft. It is then

expected that some or all of the light partons can be scattered away by a soft interaction with the nuclear surface (i.e., diffracted). In breaking the coherence of the $|uudc\bar{c}\rangle$ wavefunction, the $c\bar{c}$ are free to emerge on-shell as a real charmonium (or open charm pair) state. Thus, the A–dependence is expected to scale roughly with the nuclear surface area, giving an $A^{2/3}$ behaviour. A more detailed treatment, based on a nuclear diffusion model, predicts the nuclear dependence for intrinsic charm to scale as $A^{.71}$ for proton beams [16].

Figure 1.6 shows the calculation of equation (1.17), with the normalization given for both p+Cu and p+Be. The normalization was estimated based on the so-called diffractive component for hadroproduction of J/ψ reported by the NA3 experiment (see § 1.3.1). The contribution to the total cross section for J/ψ production attributed to the intrinsic charm of the proton was determined from the NA3 data to be

$$\sigma_{IC} = \int_0^1 \frac{d\sigma_{IC}}{dx_F} dx_F = (0.1 \pm 0.02)\sigma(\mathrm{H_2}), \tag{1.18}$$

where σ_{IC} is the intrinsic charm contribution to the cross section for p+N$\rightarrow J/\psi + X$, and $\sigma(\mathrm{H_2})$ is the measured cross section for 200 GeV p+p$\rightarrow J/\psi + X$ from NA3 [20, 21]. The intrinsic charm contribution to the cross section was assumed to be independent of the proton energy [20]. Using the nuclear dependence of $A^{.71}$, independent of x_F, we can obtain the predicted intrinsic charm contribution to J/ψ production in copper and beryllium,

$$\sigma_{IC}(\mathrm{p + Cu} \rightarrow J/\psi + X) = 1.8\,\mathrm{nb/nucleon} \tag{1.19}$$

$$\sigma_{IC}(\mathrm{p + Be} \rightarrow J/\psi + X) = 3.2\,\mathrm{nb/nucleon}. \tag{1.20}$$

These values determine the area of the curve shown in Figure 1.6. Figures 1.7 and 1.8 show, for p+Cu and p+Be, respectively, the result of adding the predicted intrinsic charm contribution to the semilocal parton duality model. The effect of shadowing

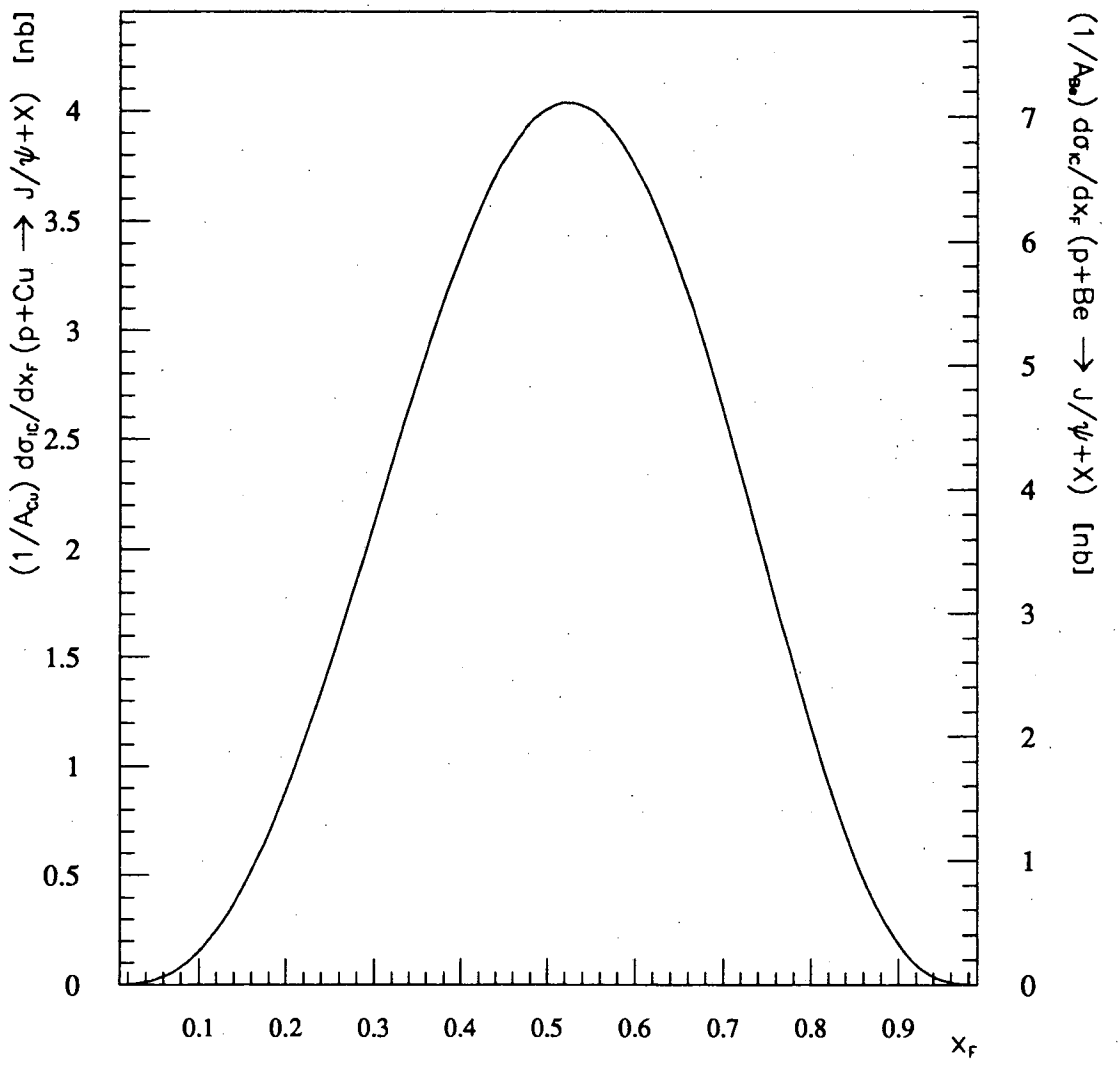

Figure 1.6: Calculation of the intrinsic charm component of the proton. The shape of the curve is obtained from equation (1.17). The two vertical axes give the normalizations for 800 GeV protons colliding with copper and beryllium targets, as discussed in the text.

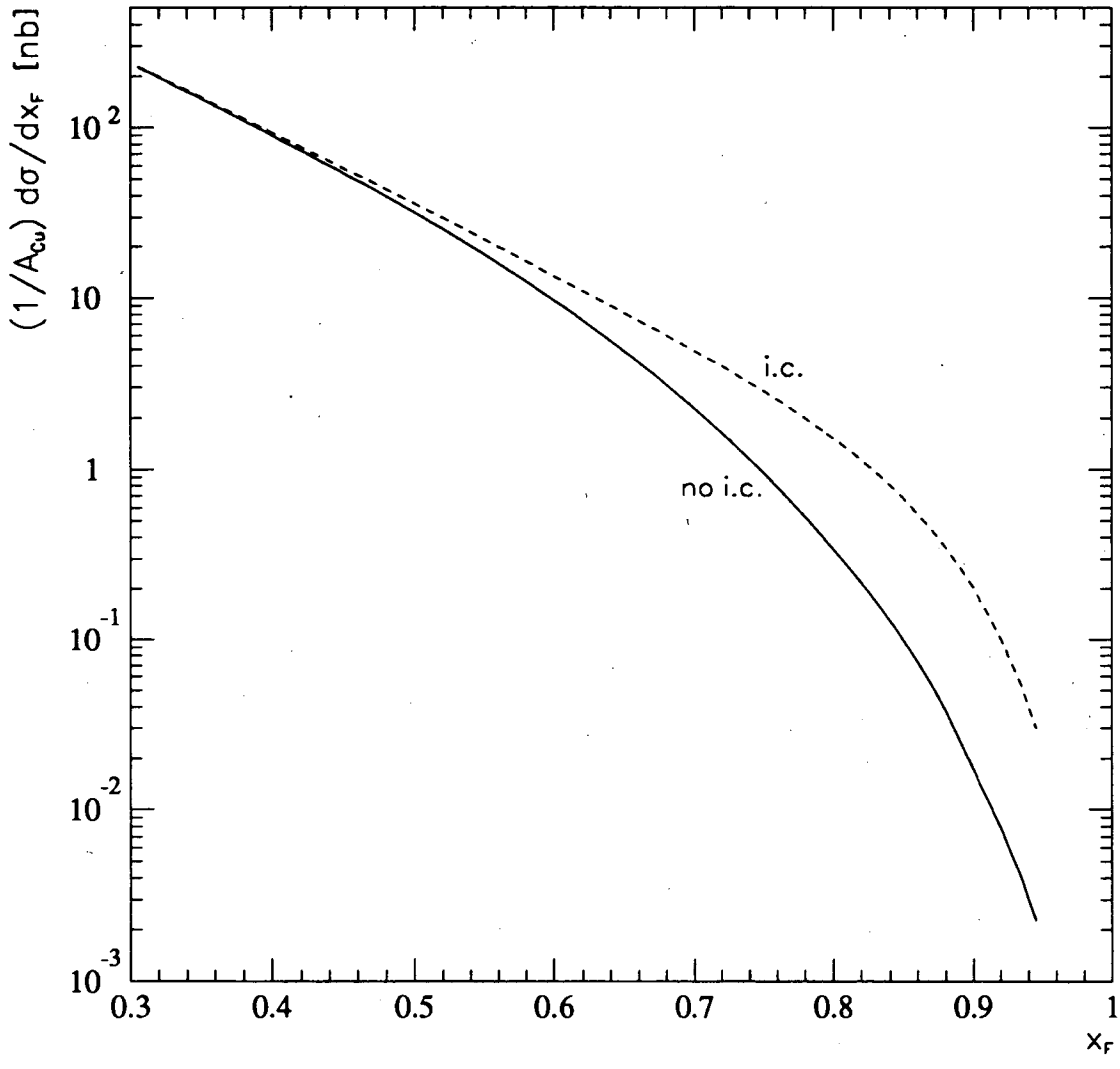

Figure 1.7: Intrinsic charm model calculation of $d\sigma/dx_F(\mathrm{p} + \mathrm{Cu} \rightarrow J/\psi + X)$. The solid curve shows the prediction of the semilocal parton duality model, including the effect of target parton shadowing. The dashed curve shows the cross section including the additional contribution predicted by the intrinsic charm model.

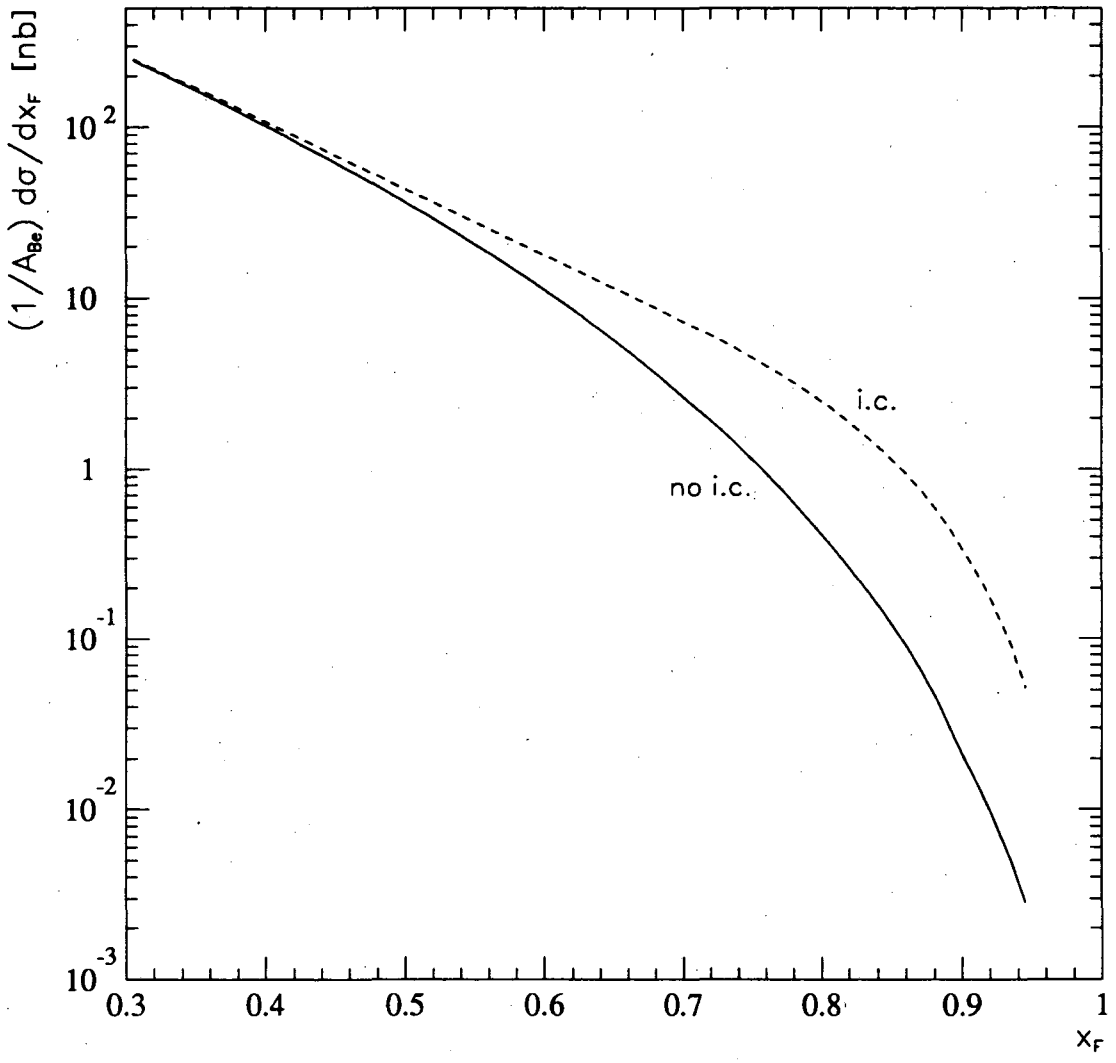

Figure 1.8: Intrinsic charm model calculation of $d\sigma/dx_F(\mathrm{p} + \mathrm{Be} \rightarrow J/\psi + X)$. The solid curve shows the prediction of the semilocal parton duality model, including the effect of target parton shadowing. The dashed curve shows the cross section including the additional contribution predicted by the intrinsic charm model.

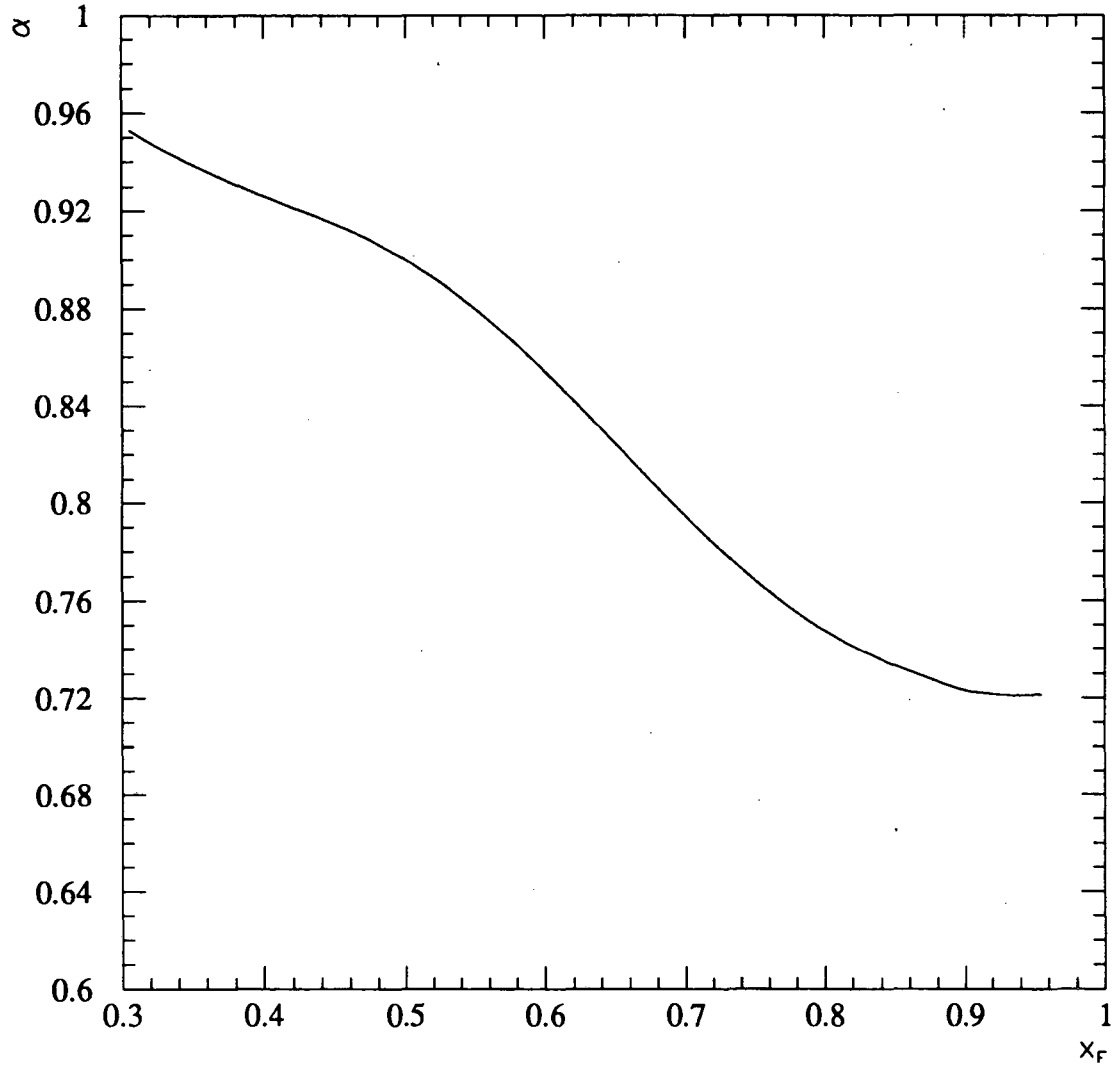

Figure 1.9: A–dependence of J/ψ production predicted by the intrinsic charm model. Assuming $d\sigma/dx_F \propto A^{\alpha}$, the prediction was determined by a semi-local duality calculation for p+Cu and p+Be collisions, with the additional contribution predicted by the intrinsic charm model.

in the target parton distribution functions, as described in § 1.2.2, has also been included in these calculations. Note the striking excess predicted by the intrinsic charm model above the parton model for $x_F > 0.6$. Figure 1.9 shows the predicted overall A–dependence for J/ψ production, based on the curves of Figures 1.7 and 1.8, in terms of the exponent α in equation (1.10).

1.3 Earlier Experimental Work

A number of experiments have studied hadronic production of J/ψ, using pion and kaon beams as well as proton beams. Many early studies were performed in the 1970's in the wake of the original discovery of charmonium, but we will only look at more recent works. This study is distinguished from earlier experiments in the relatively high statistics obtained at large x_F with *protons*.

1.3.1 NA-3

The CERN fixed-target experiment NA-3 performed a comprehensive study of hadroproduction of J/ψ with pion, kaon, proton, and anti-proton beams [21]. Two targets, platinum and liquid hydrogen, were used to determine the A–dependence. Beam energies of 150, 200, and 280 GeV were used for pions, while proton and kaon beams were studied at 150 and 200 GeV only. Production cross sections and nuclear production ratios were obtained for $x_F > 0$. For the proton production data, the statistics seem to run out around $x_F \sim 0.6$, although points were published with large uncertainties all the way out to $x_F \rightarrow 1$.

Rather than describing the A–dependence with equation (1.10), this group expresses the nuclear-dependent cross section in terms of two-components,

$$\frac{d\sigma_A}{dx_F} = A^{\alpha}\frac{d\sigma_h}{dx_F} + A^{\beta}\frac{d\sigma_d}{dx_F} \tag{1.21}$$

where α was fixed at 0.97 based on data at $x_F = 0$, and β was chosen as 0.71 for protons (0.77 for pions) on the basis of a nuclear rescattering model calculation. $d\sigma_h/dx_F$ and $d\sigma_d/dx_F$ were then fully determined from the measured cross sections $d\sigma_{H_2}/dx_F$ and $d\sigma_{Pt}/dx_F$. Both α and β were held constant, and any x_F dependent nuclear suppression was contained in $d\sigma_d/dx_F$ (the so-called diffractive component to the production). It must be pointed out that with only the two nuclear targets used, the data cannot decide between the parameterizations (1.10) and (1.21). The latest version of the intrinsic charm model associated $d\sigma_d/dx_F$ with equation (1.17).

1.3.2 E-615

The Fermilab experiment E615 studied dimuon production at large x_F with 252 GeV pions [22–24]. Only a thick tungsten alloy target was used, so no nuclear dependent effects could be studied. However, by using a closed-aperture spectrometer with beryllium and carbon absorber, this experiment was able to accumulate extremely high statistics with good mass resolution, obtaining a data set which included more than 1200 reconstructed J/ψ events at $x_F > 0.95$. From that sample of events at $x_F > 0.95$, they reported evidence for longitudinal polarization in the produced J/ψ's based on the angular distribution of the decay muons [22]. It was speculated that this was a signature for a QCD higher-twist process in J/ψ hadroproduction. This experiment also reported the production cross section for ψ', over the same range in x_F [24].

1.3.3 E-772

Fermilab experiment E772 performed a dedicated study of the nuclear dependence of dimuon production from 800 GeV protons, studying both the charmonium and

bottomonium systems, as well as the Drell-Yan continuum [13, 25, 26]. Five different nuclear targets (tungsten, iron, calcium, carbon, and liquid deuterium) were alternated frequently during the course of the experiment, providing a relatively systematics–free measurement of the production ratios as a function of x_F, $p_\perp$, and A. No absolute normalization of the J/ψ production cross section was reported by this experiment.

1.4 FERMILAB E789

The present work was performed by the E789 collaboration at Fermilab during the 1990-1991 fixed-target running period, using the E605/772/789 spectrometer[2]. The principal experimental goals of E789 were the search for charmless two-body decays of beauty ($B \to hh$), measurement of the beauty production cross section by 800 GeV protons from the inclusive decay $B \to J/\psi + X$ with $J/\psi \to l^+l^-$, and a high statistics study of open charm production through the observation of two-body decays of D mesons [27].

To facilitate these goals, the E605/772 spectrometer was substantially upgraded for the new run. A 10,000–channel, 16–plane silicon microstrip detector system was installed just downstream of the target region to measure charm and beauty decay vertices spatially separated from the production target. The first station of tracking chambers was rebuilt, replacing the old multi-wire proportional chambers with a set of new drift chambers. The Ring Imaging Čerenkov Detector, used for E605 but decommissioned during E772, was recommissioned with a new Fastbus ADC readout. A new vertex trigger processor was built to reconstruct the event decay vertices on-line, based on hits in the silicon microstrip detectors. Finally, the data

[2]See the next chapter.

acquisition system of E605/772 was replaced with a new VMEbus-based system, increasing the data taking capacity tenfold.

During the course of the 1991 run, it became clear that a high statistics study of J/ψ production at large x_F was possible by looking at $J/\psi \rightarrow \mu^+\mu^-$ decays with the J/ψ produced inside the spectrometer's copper beam dump. After a study run of a few hours in October 1991, a set of final beam dump triggers was developed. Nuclear dependence of J/ψ production at large x_F was also measured during the beam dump runs. On the last day of the Fermilab fixed-target run, a 91 cm long beryllium target was placed directly in front of the copper beam dump. In the 5-month long fixed-target run, a total of four 8-hour experimental shifts were devoted to the beam dump runs, during which the present data set was collected.

Despite being tangential to the proposed experimental goals of E789, the beam dump runs provided an opportunity to contribute to the field of hadroproduction of charmonium with minimal impact on the principal operating priorities of the experiment. This was only possible because of the upgraded data acquisition system, which permitted the present data to be collected in a few shifts, rather than in a few weeks.

CHAPTER 2

EXPERIMENTAL APPARATUS

The E789 spectrometer, shown in Figure 2.1, was the direct descendent of E772, which itself was the descendent of E605. Major upgrades were made for E789. However, for the beam-dump studies, many of these upgrades were not used. This chapter will discuss only those experimental components needed for this study.

Throughout, we will make reference to the spectrometer-fixed coordinate system. The E789 coordinate system aligns the Z-axis horizontally with the incident proton beam and the Y-axis with vertical. The X-axis is then chosen to form a proper right-handed Cartesian system. The positive Z direction, the beam direction, is also referred to as "downstream." The origin is located at the center of the upstream face of the first spectrometer magnet, SM12.

2.1 ACCELERATOR AND BEAM

The high-energy protons for E789 came from the Fermilab Tevatron, a 2 km diameter superconducting proton synchrotron. This accelerator, capable of operation in either colliding-beam or fixed-target mode, delivered beam simultaneously to over a dozen experiments during the 1990-1991 fixed-target running period. Due to the short cycle time required for the fixed-target operation of the Tevatron magnets, the maximum

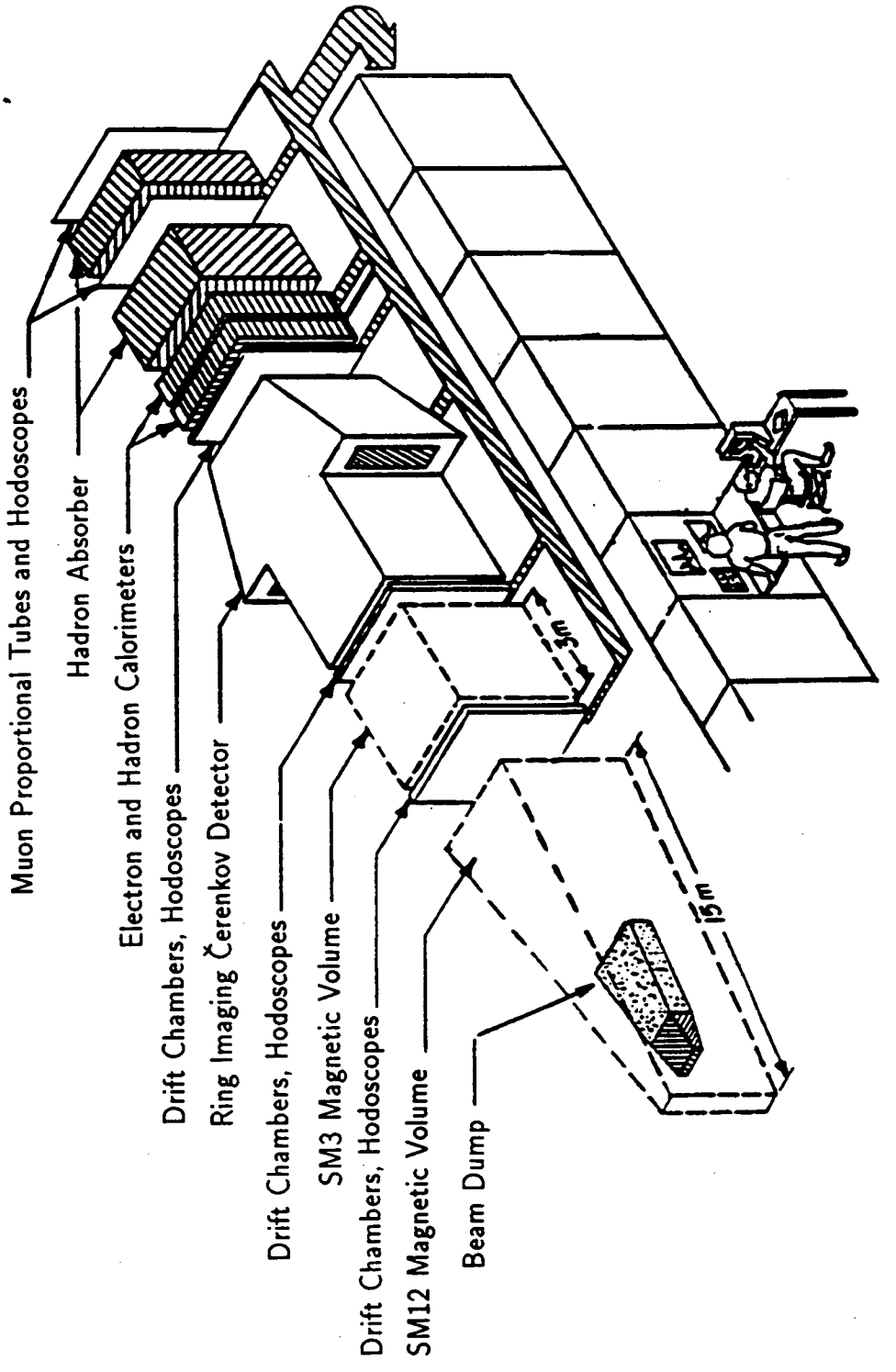

Figure 2.1: The E789 spectrometer

proton energy was lower than that during the colliding-beam mode (800 GeV rather than 900 GeV).

The Tevatron bunched and accelerated protons in 18.87 ns RF packets known as "buckets". It took ~25 seconds to accelerate a fill of protons up to 800 GeV. These protons were then smoothly extracted from the accelerator for 20 seconds. After that the superconducting magnets ramped back down for ~15 seconds—thus, the entire cycle time was approximately one spill per minute. Typical proton intensity in the Tevatron was 1-2$\times 10^{13}$ protons per spill. The accelerator operators strove to uniformly populate the RF-buckets, but the typical duty factor was 0.25–0.5. E789 monitored the duty factor by scaling the in-time and out-of-time coincidences between two highly uncorrelated hodoscope counters.

Beam was delivered to the three major fixed-target areas[1] simultaneously during the spill. Within the Meson area, a three-way split divided the proton beam between the Meson East line and the rest of the Meson lines. E789 was the sole user of the Meson East beam. Narrow upstream apertures and a string of superconducting magnets in the far-upstream area of Meson East helped to define the very low emittance proton beam that was delivered to the experiment. Beamline calculations, verified by upstream profile monitors, established the beam's angular divergence at the target as $\Delta\theta_X < 4\,\mu$rad and $\Delta\theta_Y < 200\,\mu$rad [28]. The large asymmetry was due to the elongated beam spot of 1 cm $\times$ 0.2 mm—this was chosen for efficient targeting during the D and B running modes.

For the beam-dump running mode the typical beam intensity was 5×10^{10} protons per spill. Beam intensity was monitored by two separate upstream counters located

[1]The Fermilab fixed-target yard is divided into the Meson, Proton, and Neutrino areas. These names are historical.

in the ME3 sector of the Meson East beamline—an ion chamber (ME3IC) and a secondary-emission monitor (SEM3).

2.2 Beam-Dump Targets

The E789 spectrometer was designed for running with high-intensity beam. The portion of the primary proton beam that did not interact in any upstream target continued into SM12 and was stopped by the beam dump. The dump was suspended midway through the SM12 magnet by two of the central magnet inserts, beginning at Z=173 cm, and extended 427 cm downstream. It was constructed out of pure copper, with cooling water tubes running through the sides. A 30 cm deep beam hole in the upstream face of the dump helped to contain backscattering, so beam protons did not enter the dump material until Z=203 cm. This still left nearly 4 m of copper (26.5 interaction lengths) to stop the protons and secondaries. The probability for a primary proton to punch through the entire dump was $< 4 \times 10^{-12}$.

For this study the beam dump itself was the primary target. Most primary protons would interact in the first few interaction lengths of the dump. Secondary hadrons, electrons, and photons from the primary interaction would further interact to form showers and eventually stop in the dump, but any high-energy muons produced would tend to continue moving through the dump with little interaction. These muons would lose energy and suffer multiple scattering on their way through the dump, and would then emerge from the downstream end of the dump and continue through the spectrometer. The typical equivalent transverse momentum kick due to multiple scattering received by a high-energy muon in traversing 4 m of copper was about 250 MeV. The most likely energy loss had a linearly rising contribution due to radiative effects such as bremsstrahlung and pair-production, and a flat con-

tribution due to ionization. For a 50 GeV muon the most likely energy loss was just under 7 GeV, whereas for a 500 GeV muon it was over 10 GeV (see Figure 2.2). Fluctuations in the actual energy lost by the muon were substantial, especially at high energies. This dominated the uncertainty in reconstructed x_F.

To study nuclear dependence, a thick beryllium target was added in front of the copper beam dump. This was done on the last day of the 1991 experimental run. A long piece of aluminum channel was balanced inside the beam hole in the upstream face of the copper dump and held level to the Z–axis about 1 cm below the primary proton beam by a wooden support at the face of the magnet. A total of 6 beryllium blocks, each measuring $2 \times 4 \times 6$ inches, for a total length of 91.4 cm (2.25 interaction lengths), were slid down this aluminum rail to be nearly flush against the upstream face of the copper beam dump. The upstream face of the beryllium was located at Z=60 cm. During this dedicated final running mode, primary protons were incident on the beryllium, where about 90% of them interacted. A statistical subtraction must be made to the data for the estimated 10% primary punch-through from the beryllium into the copper.

2.3 Spectrometer Magnets SM12 and SM3

The principal bending magnet used for E789 was the SM12 dipole magnet. This 1200 ton, 14.5 meter long tapered conventional magnet was constructed from iron originally used for the Columbia University / Nevis Laboratory cyclotron. Hollow aluminum windings carried large currents to generate the field, allowing cooling water to flow through the center of the conductor. The magnet produced an average horizontal field of up to 1.3 Tesla at a maximum current of 4000 amperes, delivering a 7 GeV transverse momentum kick to relativistic particles traversing its entire length.

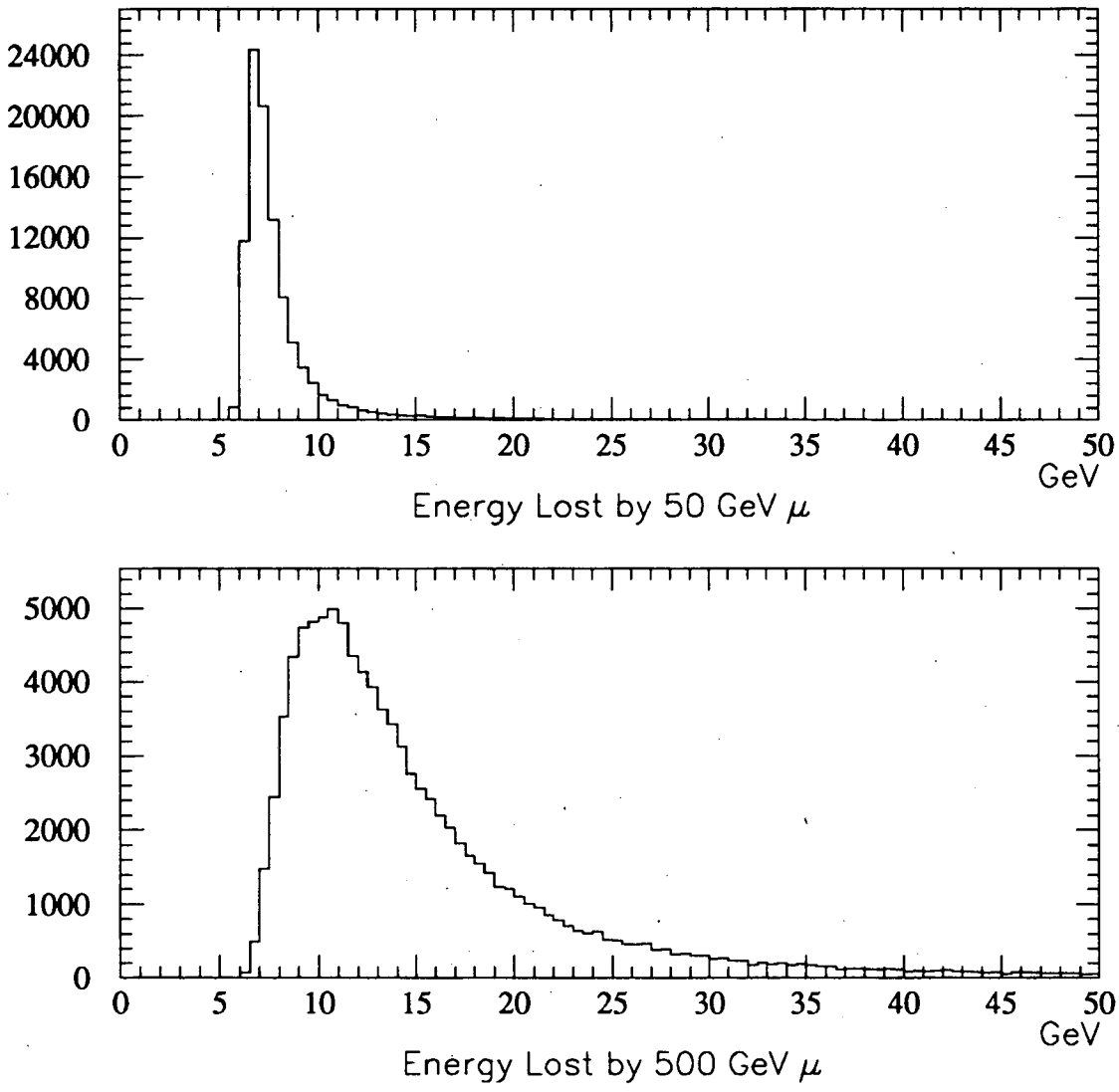

Figure 2.2: Simulation of energy loss for muons traversing the beam dump. The upper plot shows the energy loss spectrum for 50 GeV muons, the lower plot for 500 GeV muons.

For the beam dump runs, SM12 was operated at 2400 amperes. For tracks originating at the beginning of the beam dump, this delivered a transverse momentum kick of 3.64 GeV.

To analyze events, a detailed field map was needed to accurately retrace the tracks backwards through the magnet. To obtain this, the Fermilab "Ziptrack" system was used. The Ziptrack consisted of three orthogonal coils mounted on a movable rail that was inserted into the magnet. The coils traveled ("zipped") through the field, and integrators converted the induced coil currents into digital counts for the corresponding magnetic field values. The track was then moved to another position, and the coils scanned across the field again. In this way, nearly the entire field volume was measured. The measurements were then regularized to give a usable field map for event reconstruction.

The track momentum measurement was provided by the downstream analyzing magnet, SM3. This 3.4 m long conventional magnet, with horizontal field but opposite polarity to SM12, delivered a nearly uniform transverse momentum kick of 0.914 GeV across its entire aperture when operated at its maximum excitation current of 4268 amperes. The Ziptrack system was used to measure the field for this magnet as well. The field was sufficiently uniform that a single bend-plane approximation for describing a particle trajectory through the field volume provided good track reconstruction.

Both magnets were filled with helium bags to minimize the effect of multiple scattering. The SM12 helium bag, however, was removed for the last run to allow the installation of the beryllium target.

2.4 Tracking Stations

Tracking detectors record the passage of charged particles in space (and time) across their active area. It is from these discrete points that trajectories through the spectrometer are determined, allowing the 4-momentum of the individual downstream tracks to be measured (using the angular deflection of the track through the magnetic field of SM3). Off-line, a trace-back through the SM12 field established the momentum at the production point. Together with particle-ID for establishing the mass of the particle associated with the track, this determined each track's 4-momentum, from which the kinematics of the event was reconstructed. Coarse-resolution detectors, scintillator hodoscopes, were used to determine the rough event topology in real-time for triggering, while fine-resolution detectors, drift chambers, gave the final event reconstruction.

The arrangement of tracking detectors into distinct stations simplified the event reconstruction by constraining all projections of the track to be consistent with a single point in space in each station. Stations 1–3 each consisted of hodoscopes and drift chambers, while Station–4, located behind thick hadron absorbers, consisted of hodoscopes and proportional tubes. Station–4 was used for muon identification and triggering, while the first three stations were used for general triggering and tracking.

2.4.1 Scintillator Hodoscopes

Each tracking station, as well as the muon station, had one or two planes of scintillator hodoscope. These detectors provided fast tracking signals on a coarse granular scale for use in triggering. The detector elements were constructed of NA-110 plastic

Table 2.1: Scintillator Hodoscopes

detector name	position (cm)	# counters	cell width (cm)	aperture (cm)	
				X	Y
$Y1$	1995.80	2×12	6.35	120.35	77.95
$X1$	1959.61	12× 2	10.16	120.75	76.20
$Y2$	2831.95	2×16	7.62	163.83	123.51
$X3$	4627.88	12× 2	22.05	267.16	233.68
$Y3$	4653.28	2×13	19.05	264.16	233.68
$Y4$	5170.17	2×14	20.32	294.64	254.00
$X4$	5413.04	16× 2	18.10	320.04	289.56

scintillator. Each hodoscope plane was arranged into two half planes of parallel scintillator paddles, providing measurements of the track Y–intercepts (X–intercepts) on the left and right (top and bottom) sides of the spectrometer. Scintillation photons were collected from the ends of the active material by plexiglass light guides and were transported onto Hamamatsu R329 fast photomultiplier tubes. Table 2.1 gives the layout for the seven scintillator planes used. Only a single bit (hit or not hit) was obtained from each paddle.

2.4.2 Drift Chambers

Each tracking station was constructed with 6 planes of drift chambers, arranged in three pairs of parallel offset planes. Each pair was mechanically supported by a single aluminum frame, providing a rigid half-cell offset between the two parallel planes. The upstream plane of each pair was the "unprimed" plane, while the downstream plane was the "primed" one. The Y–Y' pair of each station was constructed of horizontal wires to measure the Y-intercept of the tracks. Additionally, each station had a pair of planes tilted at a slope of +0.25 (U–U') and -0.25 (V–V') with respect to the horizontal. These stereo-view planes determined the X–intercept of the track and provided a consistency check on the Y–intercept. Time-to-Digital Converters,

TDCs, were used to measure the drift time of liberated electrons from the track to the anode sense wires. The combination of good hits together with their associated drift times in all three views gave a "triplet" hit for a station – these triplets were later used to reconstruct track segments and ultimately full tracks.

The drift chambers were all operated with a gas mixture (by volume) of 49.7% argon, 49.6% ethane, and 0.7% ethanol, mixed at $-7°$ C and flowing at 3 standard cubic feet per hour. The Station–1 anode wires were gold-plated tungsten wire, 25 μm diameter, while Stations 2 and 3 used silver-coated beryllium-copper wires, also of 25 μm diameter. The cathode wires for all three stations were made of 62.5 μm diameter silver-coated beryllium-copper wire, operated at between -1600 and -2200 volts. Typical drift velocity was 50 μm/ns. Table 2.2 gives the configuration of drift chambers used in the E789 spectrometer.

2.4.3 Muon Proportional Tubes

To aid in off-line muon identification, three planes of proportional tubes were located in Station–4. The three planes were arranged into 2 Y planes of horizontal wires (PTY1 and PTY2) and one X plane of vertical wires (PTX). All three planes were made of aluminum extrusions with two layers of 2.54×2.54 cm cells, offset by a half-cell spacing to cover the dead region between adjacent cells. Table 2.3 gives the proportional tube arrangement. These detectors used the same argon/ethane/ethanol gas mixture as the drift chambers.

In order to reach the $Y4$ hodoscope and the $PTY1$ proportional tube planes, a particle had to punch through the entire calorimeter as well as thick concrete, zinc, and lead absorbers. This provided a total of 16.6 interaction lengths upstream of $Y4$. Thus, in general, the only charged tracks which could reach the Station–4

Table 2.2: Drift Chambers

detector name	position (cm)	# wires	cell size (cm)	aperture (cm) X	aperture (cm) Y	operating voltage
$V1$	1879.8	208	0.508	119.4	81.3	-1600
$V1'$	1885.0	208	0.508	119.4	81.3	-1600
$Y1$	1904.5	160	0.508	119.4	81.3	-1600
$Y1'$	1909.7	160	0.508	119.4	81.3	-1600
$U1$	1930.3	208	0.508	119.4	81.3	-1600
$U1'$	1935.5	208	0.508	119.4	81.3	-1600
$U2$	2751.8	160	0.986	167.6	130.0	-2000
$U2'$	2757.2	160	0.986	167.6	130.0	-2000
$Y2$	2776.8	128	1.016	167.6	130.0	-2000
$Y2'$	2782.1	128	1.016	167.6	130.0	-2000
$V2$	2802.3	160	0.986	167.6	130.0	-2000
$V2'$	2807.6	128	0.986	167.6	130.0	-2000
$U3$	4546.8	144	2.021	269.2	242.6	-2200
$U3'$	4553.8	144	2.021	269.2	242.6	-2200
$Y3$	4572.5	112	2.083	269.2	233.3	-2200
$Y3'$	4579.5	112	2.083	269.2	233.3	-2200
$V3$	4598.0	144	2.021	269.2	242.6	-2200
$V3'$	4605.0	144	2.021	269.2	242.6	-2200

Table 2.3: Proportional Tubes

detector name	position (cm)	# wires	cell size (cm)	aperture (cm)	
				X	Y
$PTY1$	5186.04	120	2.54	297.2	304.8
PTX	5425.12	135	2.54	343.9	308.6
$PTY2$	5589.90	143	2.54	359.4	363.2

detectors were muons. Additional layers of shielding concrete between the planes in Station–4, giving a total of 21.6 interaction lengths, added further rejection.

2.5 TRIGGERING

For the beam-dump runs, only the lowest level trigger was needed to select events for archiving. This trigger, known as the Trigger Fan In (TFI), cycled at the full rate of the accelerator RF, 53 MHz, without any dead time. The higher level triggers were set to force-through all TFI-generated triggers, so that during the beam-dump running periods, a TFI-signal would initiate the readout and the archiving of an event.

Two distinct logical combinations of hodoscope signals were used to define the TFI for these runs, and these two triggers were logically OR'ed to form the final trigger. Each of these triggers was monitored with a single bit in a coincidence-register called the Trigger-Bit Latch, and was recorded with the event. Triggers were inhibited during event readout at the next stage of the trigger, the Trigger Generator Output (TGO), by the assertion of the System Busy signal. Spill scalers counted the total number of TFI's generated during each spill, as well as those generated in coincidence with System Busy being false—this allowed for an estimate of the overall live time for the runs.

The two trigger combinations were chosen principally to be satisfied by any pair of muons. Thus, both triggers made some requirement for hits in the Station–4 hodoscopes. Additionally, the two triggers were chosen to be complementary, so that the trigger efficiency could approach the geometrical acceptance for dimuon events from the beam dump.

2.5.1 $3/4\mu L \bullet 3/4\mu R$

The first of the two triggers used for beam-dump running was $3/4\mu L \bullet 3/4\mu R$. This trigger itself was formed by the logical AND of two lower level signals, $3/4\mu L$ and $3/4\mu R$. Each of these signals was generated by a coincidence logic circuit which required at least 3 out of the 4 hodoscope planes $X1$, $Y2$, $X4$, $Y4$, to have a hit in them on the left (right) side of the spectrometer. Since two of the four planes in this trigger were in Station–4, and only one plane was allowed to have no hits, this trigger effectively selected muons on either side of the spectrometer. By allowing one of the four planes not to fire, this trigger allowed for some inefficiency in the hodoscopes. More importantly, this made it possible to *measure* the efficiency of all hodoscope planes, since the trigger bias could be removed from those planes in the trigger. This would not be possible if the trigger required 4-out-of-4 planes fired.

The disadvantage of this trigger was that it required the dimuon event to "straddle" the center line of the spectrometer, with one muon falling on the left side, and the other on the right. This requirement became inefficient for dimuon events produced with moderate or high $p_\perp$ at high x_F, since it effectively restricted the azimuthal orientation of the decay plane to be more and more horizontal. For this reason, a second beam dump trigger was defined.

2.5.2 $2M4 \bullet 2Y4$

The $2M4 \bullet 2Y4$ trigger was based on a hodoscope matrix circuit that compared hodoscope patterns with predefined "roads" found in detailed Monte-Carlo simulations. Four very high speed ECL memory circuits stored patterns for the $Y1$ hodoscope as a function of possible hit patterns of hits in the $Y2$ and $Y3$ hodoscope planes. Real hit patterns in $Y2$ and $Y3$ were combined to form an "address" in this matrix memory, which then returned the predicted hit pattern for $Y1$. A coincidence circuit then compared the actual pattern of hits in $Y1$ with that predicted by the memory lookup, and any coincidence would satisfy the matrix. The four separate memory circuits divided the spectrometer into four quadrants (up-left, up-right, down-left, and down-right), so there were finally four matrix signals, one corresponding to each quadrant in the spectrometer. These signals indicated a hodoscope pattern in that quadrant consistent with a "good" track (as determined by the Monte-Carlo simulation). For the beam-dump running, a special matrix file was generated for patterns consistent with tracks originating in the beam dump.

The $2M4$ signal was formed by a coincidence logic circuit requiring any 2 out of the 4 matrix quadrant signals fired. To ensure that only muons had fired this trigger, a Station–4 requirement was added to the final trigger. The multiplicity signal $2Y4$ would fire whenever at least two of the paddles within the $Y4$ hodoscope were hit. By requiring this signal be in coincidence with the $2M4$ signal, the matrix trigger was turned into a beam-dump dimuon trigger, $2M4 \bullet 2Y4$.

This trigger had the distinct advantage of not biasing against events with high $p_\perp$ and high x_F. A drawback, though, was that it had no redundancy in it. Thus, any inefficient hodoscope counters would directly translate into regions with poor acceptance. The effect on the efficiency of the trigger was estimated with the detailed

Table 2.4: Trigger Rates per 10^{10} incident protons

	Copper	Beryllium
$3/4\mu L \bullet 3/4\mu R$:	6240	9770
$2M4 \bullet 2Y4$:	6048	10590
events written to tape:	9531	15730

Monte-Carlo simulation, where individual hodoscope efficiencies were modeled. The hodoscope efficiencies could only be measured, however, by considering events which fired the $3/4\mu L \bullet 3/4\mu R$ trigger.

The combination of these two triggers gave a clean and efficient trigger for dimuon events from the beam dump, and permitted the archiving of over 50 million events to tape during the roughly 30 hours of beam-dump running. Table 2.4 summarizes the trigger rates for the copper and beryllium running periods. Note that for many events, both triggers fired, so the rate of events written to tape is less than the sum of the two separate trigger rates. The higher trigger rates during the beryllium running period were mostly due to single hadrons produced in the beryllium and travelling *around* the copper beam dump. These tracks, together with single muons and noise hits in the Station-4 hodoscopes, could accidentally satisfy the trigger. These events were easily eliminated from the data set off-line during the analysis.

2.6 Readout and Data Acquisition

Upon triggering, event readout would commence. This process consisted of two distinct phases – digitization of event information, and transfer of that information to the archiving system. The two phases were pipelined, so that some parts of the readout system would transfer data to archive while the other parts were still digitizing.

In addition to the event data, a bank of several dozen scalers counted hits in a variety of detectors for the duration of the spill, and these were recorded, then reset, at the end of each spill.

2.6.1 Nevis Transport

The backbone of the E789 readout was a Nevis Transport system [29]. All detector subsystems ultimately fed data onto the Transport. Bus arbitration was maintained by a hard-wired daisy chain, with the bus mastership determined by the Carry signal. In addition to preventing multiple subsystems from attempting to place data on the Transport simultaneously, this scheme guaranteed that events appeared on the readout bus in a well-defined format. A synchronous 10 MHz clock regulated data transfer on the 16-bit wide bus, which carried a distinct data word on each clock cycle.

Upon receipt of the TGO signal, a dedicated device on the Transport bus—the Event Generator Source (EGS)—would raise the System Busy signal to inhibit any further triggers and take control of the Carry signal. The EGS then wrote a special "first-word" onto the Transport bus to indicate the beginning of a new event in the data stream. After a few more words from the EGS, the Carry signal was passed to the first branch of the readout system to begin transferring event data onto the Transport.

The TGO signal, together with a "START" signal from the EGS, would also signal the beginning of the digitization process. The hodoscopes and muon proportional tube signals were all amplified and discriminated, and then recorded by a bank of coincidence registers (CRs). Each hit in the CR would generate one word in the event output, containing the hodoscope or wire number of the muon proportional-tube hit. The Trigger Bit Latch was recorded in a similar way, so that each event

contained a record of which trigger circuit(s) caused it to be read out. This data was transferred from the CR crate onto the Transport bus.

In addition to the CR's, time-to-digital converters ("TDC"s) recorded event information from the drift chambers. On receiving the START signal, each TDC would begin incrementing a grey-code counter once every ~4 ns. Signals from the drift chamber wires were amplified and discriminated, and the output of the discriminators generated the stop signal for the TDC's. Each hit in the drift chamber produced one word in the event output, containing the wire number of the hit along with the grey-code value of the TDC timer. This measured the drift time of the track's liberated electrons to the sense wire.

2.6.2 Scalers

Scalers recorded information such as beam intensity, trigger rates, and duty factor during the spill. E789 used a single CAMAC crate containing 20 four-channel gated scalers. The CAMAC crate was connected through a Branch Highway directly to an interface on the online PDP-11/45, which read out the scaler values at the end of each spill and transferred them via a direct link to the VAX system, where they were recorded to disk by a background job known as Rasputin.

2.6.3 VME Data Archiving

The original archiving system for E605 and E772 was based on a custom-built 1 megabyte (later expanded to 4 megabytes) dual-ported memory unit, the "MegaMemory". The MegaMemory could store up to 4 megabytes of event data or 4096 actual events per spill (whichever came first), and would stream data to 6250-BPI magnetic tape between spills. The online PDP could also sample a small fraction of these events between spills for real-time monitoring and analysis. While

this system performed well for those earlier experiments, the limitations imposed both on the number of events and the volume of data that could be recorded per spill had become unacceptable for the present experiment.

For E789, the MegaMemory and the 6250 tape drive were replaced with a new VME-based archiving system [30]. The new system shared the Transport output stream with the old MegaMemory, which was retained to continue real-time monitoring, but could record an order of magnitude more data. This new system, coded entirely in C and built with commercial hardware, was layered on top of the VxWorks real-time operating system. Events streamed into the VME through a pair of "ping-ponging" triple-ported VME high-speed memory boards by way of a front panel ECL interface. Interrupt-driven software would initiate DMA transfers of packets of events from the high speed memories across the VMEbus into a 64 megabyte ring-buffer. This buffer was continuously being drained across the VMEbus into a single-board computer by a concurrent task which performed all the formatting previously handled by the MegaMemory hardware. From there, formatted packets of events were queued in a small pool for distribution to the taping subsystem, where up to four Exabyte 8mm tape drives would record the data. Under test conditions, this system was capable of a maximum sustained throughput of 1 megabyte/second, but real data taking yielded a practical maximum of 40 megabytes/spill written to tape, due mostly to the limitations of the Exabyte drives. Data tapes written with the new VME system were compatible with the older 9-track magnetic tape format, and could be read by the existing off-line analysis software.

For the beam dump running, the VME Data Archiving system recorded over 50,000 events per spill. The average event size during the beam dump runs was 188 16-bit words.

CHAPTER 3

DATA ANALYSIS

The analysis presented in this study was performed on a cluster of four 75-MIPS Hewlett-Packard apollo 9000/730 UNIX workstations located at the Lawrence Berkeley Laboratory. The analysis was divided into two full passes through the data, with each pass reducing the volume of data. A third, final pass was performed using the CERN Physics Analysis Workstation software package (PAW). For the data presented in this study, 357 CPU-hours (26,800 MIPS-hours) were used for the first pass, while each trial of the second pass took 15 CPU-hours.

In addition to the multiple passes of analysis code, a detailed Monte-Carlo simulation of the experiment was used to normalize the acceptance of the spectrometer as well as the efficiency of the triggers and reconstruction. Several hundred CPU-hours were spent on various Monte-Carlo studies, but the final normalization runs used a total of 26 CPU-hours.

3.1 PASS–1

The version of Pass–1 used for this analysis was restricted to simply unpacking raw event data, finding good tracks through the drift chambers, and requiring all tracks be identified as muons. Events surviving this pass were written to one of several "micro-Data Summary Tape" (μDST) files, based on the number of muon tracks

found in the event. The μDST recorded 64-bits of summary information for each event, along with the position at the SM3 bend plane and momentum of each track. Events stored in this format were on the average a factor of 6 smaller than the original raw events. This permitted large data sets to be stored online in μDST format disk files, rather than having to stage latter passes of the data through Exabyte tapes.

3.1.1 Unpacking

Before any analysis of an event could begin, the raw data from a tape was "unpacked." The readout system was optimized for speed and efficiency, which meant that every bit of every word was utilized to carry experimental information. At the analysis stage, however, it was much more convenient to expand the data a little, so that full 32-bit real (or integer) variables would contain the geometrical information encoded in the original raw words. The first step of the analysis loop unpacked the raw hit information into predefined Fortran COMMON blocks, and ensured that events conformed to the proper format.

3.1.2 Tracking

The core of the first pass analysis was the tracker. The track finding algorithm used in Pass–1 was divided into three stages, each of which consumed a roughly equal fraction of the total CPU time.

The first step in track finding consisted of searching through all the drift chambers in Station–2 and Station–3 for hit clusters. This process, performed in the subroutine DCTRIPS, required hits in 4 out of the 6 planes of a station to register a cluster. Clusters were categorized as either doublets (having hits in only two views) or triplets (having hits in all three views). All clusters were required to have at least one hit in the Y view.

Once a list of triplets (and doublets) was made, the second step was to link combinations of clusters from Station–2 and Station–3 into track candidates. The subroutine DCTRAX constructed these track candidates, selecting only those combinations of clusters which were loosely consistent with the hypothesis that the track came from the production target. For this study, the production target was the beam dump, and very loose cuts were made to simply require the track candidate point back to the beam dump in the XZ-view (the non-bend view).

The final step in the tracking process was to link track candidates found in Station–2 and Station–3 with hit clusters in the Station–1 drift chambers. The subroutine WCTRAX performed this step in the reconstruction. Each track candidate found in DCTRAX was projected through SM3 in the XZ-view to a vertical band in Station–1. Only clusters found within this band were further considered—this cut reduced by more than a factor of 6 the number of combinations which needed to be tested for the final track reconstruction. Once a cluster was found in Station–1, the entire track was refit using all 18-planes of drift chambers, and allowing the Z-coordinate of the SM3 bend plane to vary. All tracks were required to have hits in at least 14 out of the 18 planes. The result of this final fit gave the position of the track in X, Y, and Z at the SM3 bend plane, and the slopes θ_X, θ_Y^{U}, and θ_Y^{D}, where "U" and "D" refer to upstream and downstream of the SM3 bend plane. The difference θ_Y^{U} - θ_Y^{D}, together with the field map of SM3, determined the Y-Z projection of the track momentum. This, together with θ_X, fully determined the momentum at Station–1. A final cut was made on the reduced χ^2 from the 18-plane fit, requiring the track to have $\chi^2/\mathrm{NDF} < 5$. The χ^2/NDF for each track was recorded to the μDST file as part of the 64-bit control field.

3.1.3 Muon Identification

Once tracking was completed, particle identification was performed to select only those tracks consistent with being muons. Since the calorimeter readout was disabled for beam dump running, muon identification was performed only on the basis of hits in Station–4. This took advantage of the many interaction lengths present in the calorimeter, as well as the additional absorber placed after the calorimeter, to stop all particles other than muons and neutrinos. After the tracking stage was completed, each track was projected into Station–4 to determine the most likely hit locations in the proportional tubes and hodoscopes. A window wide enough to allow for the effects of multiple scattering to within 5 standard deviations was determined for each detector plane in Station–4 centered on the projected track intercept. For high momentum muons, these windows were never greater than a few cells wide. The detectors were then scanned for hits within these windows.

A field of 5 bits, corresponding to the 5 detector planes in Station–4 (PTX, $PTY1$, $PTY2$, $X4$, and $Y4$), was set for each track to record which detectors had hits in the windows. A muon was identified by a minimum of 3 of the 5 bits fired, along with the requirement that at least one of the bits correspond to a scintillator hodoscope ($X4$ or $Y4$). This cut was found to be greater than 99% efficient, based on the copper dump running period. Studies based on the D and B running modes, in which the calorimeter readout was enabled, showed the Station–4 cuts to have good rejection against hadrons. Further cuts in the second pass, which required the tracks to trace through the length of the beam dump, eliminated any residual hadronic contamination.

3.1.4 Hodoscope Fiducials

To help better define the acceptance, a fiducial zone was defined on each hodoscope paddle. These fiducial zones excluded the last 1–3 mm from the edges of each paddle, eliminating the effect of small misalignments between the scintillators. Each good quality track was projected to every hodoscope plane, and a bit was set based on whether the track crossed the hodoscope within the fiducial zone or not. Finally, the trigger condition was imposed on the fiducial bits. If the fiducial bits fulfilled the trigger requirements, another bit in the event was set before outputting the event to the μDST. By cutting on this bit in the second pass for both real data as well as the Monte Carlo simulation, it was possible to significantly eliminate the systematic uncertainties due to small gaps and misalignments between the paddles in the hodoscope planes.

A study was performed to test this cut, in which the fiducially excluded regions on each hodoscope were doubled. This of course led to lower statistics, but the acceptance normalized yield from this study was in good agreement with the results of the nominal fiducial cut.

3.1.5 Study Runs

In addition to the main analysis runs, special studies were performed with the Pass-1 code to understand the data better. Hodoscope efficiencies were determined for each running mode by analysing only those events which had fired $3/4\mu L \bullet 3/4\mu R$. All tracks used in the efficiency study were required to cross the hodoscope planes within the fiducial zones. For those planes which were *not* part of this trigger, the efficiency was calculated simply as the ratio of tracks with hodoscope hits divided by all tracks, binned across each hodoscope paddle. To eliminate the trigger bias from the four

planes which constituted the trigger, an event was only considered for a given plane (as either a hit or a miss) if *the remaining three trigger planes had also fired.* If one of the other three planes was missing, then the event was not considered in the efficiency calculation for that plane. Hodoscope efficiencies were recorded for each paddle for later use in the detailed Monte Carlo. Most of the hodoscope paddles were more than 95% efficient, but a few had efficiencies below 80%.

Drift chamber efficiencies were calculated in a similar way, except that no trigger bias needed to be removed. However, there were several dozen missing wires in the spectrometer. Since these wires were explicitly modeled in the detailed Monte Carlo, it was important to exclude them from the plane-by-plane efficiency calculation to avoid double-counting. Any track pointing back to one of the known dead wires was discarded from the efficiency determination for that plane. Each chamber was divided into four parts, and the efficiency for each part was also recorded for later use in the Monte Carlo. All of the drift chambers had an overall efficiency greater than 95%, apart from the dead wires. Fewer than 1% of all the wires in the drift chambers were dead.

Additionally, the raw hit multiplicity and hit distributions were recorded for each hodoscope and drift chamber plane. These distributions were used to generate additional random hits in the detector planes in the Monte Carlo simulation. This provided a measure of the efficiency of the track-finding software for finding good tracks in the presence of additional hits in the drift chambers. The chamber multiplicities were low enough in the beam dump runs that accidental hits were not a problem.

3.2 PASS–2

The second pass analysis code was written exclusively for the study of dimuons from the beam dump. The code was optimized for the HP–730 computers, and made extensive use of the double-precision (64-bit) vectorized hardware. Pass–2 read the μDST files produced from Pass–1, and determined physics variables for each event. These physics variables, such as the invariant mass, x_F, and $p_\perp$, were then binned and histogrammed using the CERN HBOOK library. A histogram file was recorded to disk for final analysis using PAW.

Only events with two oppositely charged muon tracks were considered for the Pass–2 analysis. Like-sign pairs and three-muon events, consistent with accidentals, accounted for 4% of all events.

3.2.1 SM12 TRACEBACK

Upon reading an event from the μDST, Pass–2 would begin its analysis by tracing each muon track from the SM3 bend plane toward the upstream end of the beam dump. The SM12 field map was used for this procedure, with corrections for the effects of energy loss and multiple scattering in the dump material applied to the track. See Figure 3.1 for a typical beam dump J/ψ event display.

The effect of multiple scattering of the muons in the dump made it impossible to accurately reconstruct the event vertex. This can be seen in Figure 3.2, which shows the distributions of Z_{vtx} (as determined from the Y-Z view) of the copper dump and beryllium dump data, for two regions in x_F. Note that the true scale factor for the Z_{vtx} distribution is the nuclear interaction length λ_I, which is 15.1 cm in copper and 40.7 cm in beryllium. The actual distributions observed in the data are much wider than this, due to multiple scattering. This is especially true at high x_F, where the

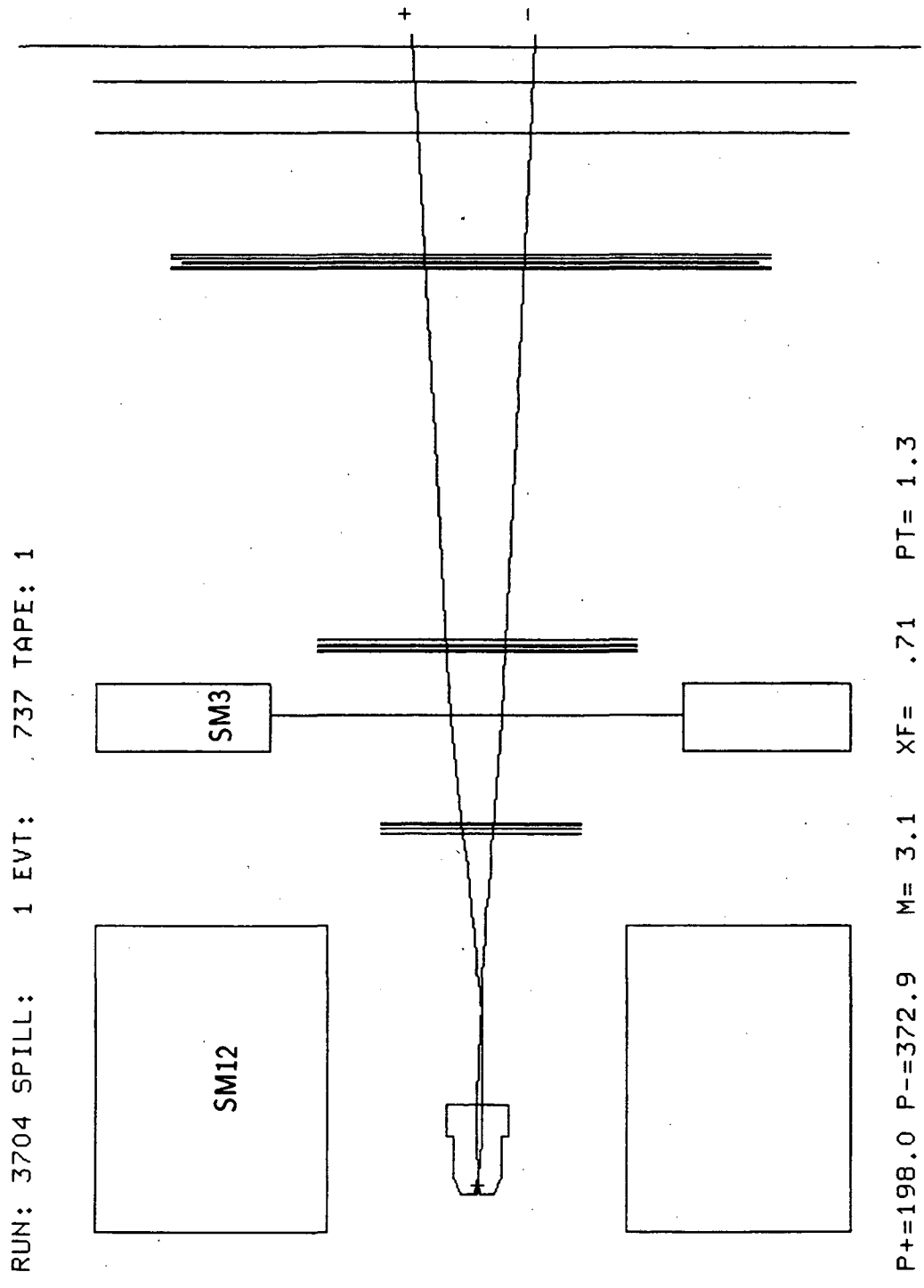

Figure 3.1: A typical J/ψ event, viewed in the Y-Z plane. Note the greatly compressed horizontal scale.

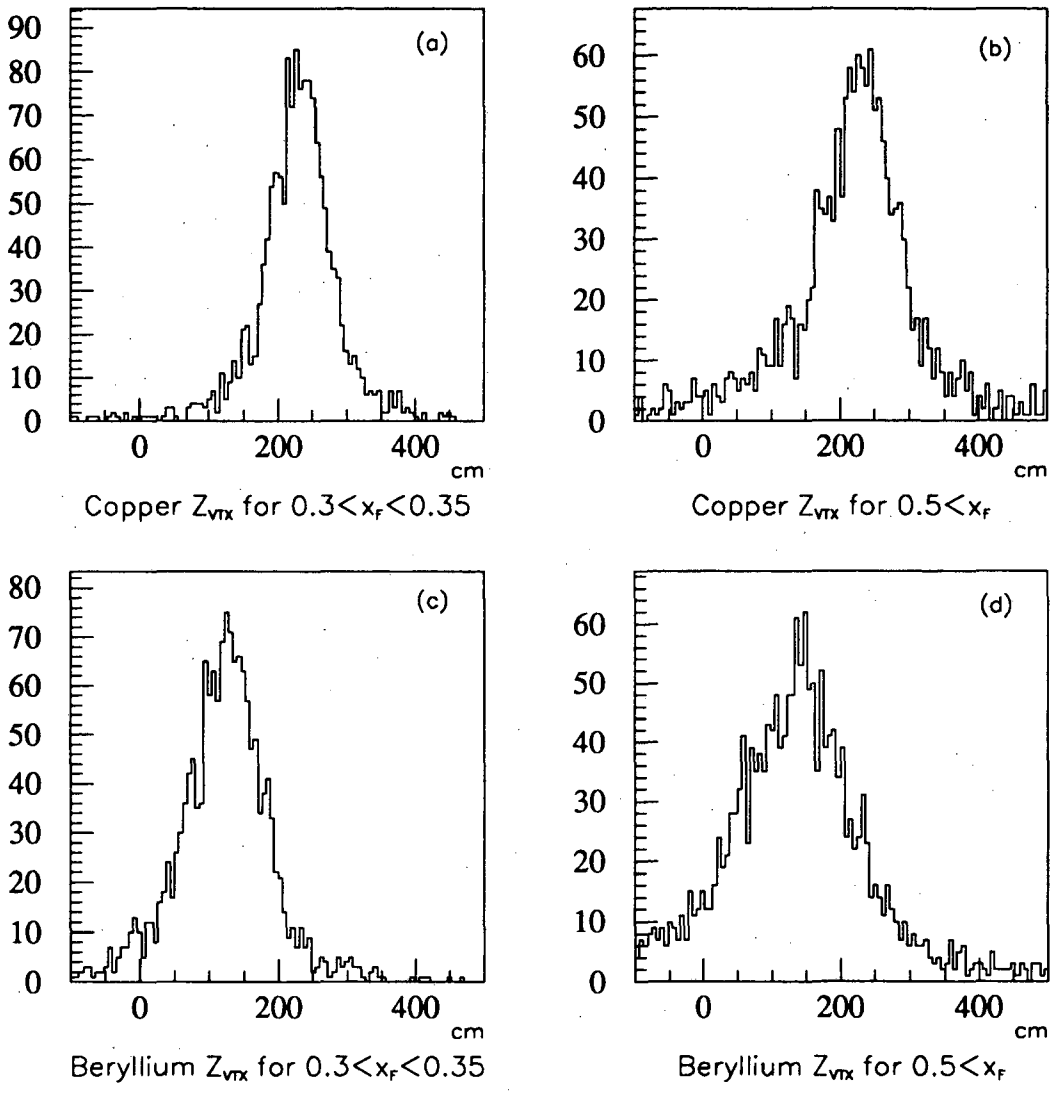

Figure 3.2: Z_{vtx} determined from the track traceback in the Y-Z view. (a) and (b) show the distributions in the copper dump data for two regions in x_F, while (c) and (d) show the same regions in x_F for the beryllium dump data. Note that the beam dump extends from $Z = 203$ cm to $Z = 599$ cm, and the beryllium extends from $Z = 60$ cm to $Z = 151$ cm.

average opening angle between the J/ψ decay muons is the smallest. Rather than attempting to reconstruct the vertex of each event on the basis of the traceback, a statistical hypothesis was used, whereby all events were assumed to come from one interaction length into the dump (the nominal target plane, Z_{TGT}). Monte-Carlo studies, shown in Figures 3.3 and 3.4, demonstrated that this technique did not bias the reconstructed mass or x_F distributions.

After the traceback, the track was required to have gone through at least 1 m of copper dump material. An additional cut required the intercepts, X_0 and Y_0, of the track at Z_{TGT} be within 3 standard deviations of the beam centroid values, X_{TGT} and Y_{TGT}. (See § 3.2.3 for the distributions of X_0 and Y_0, and the determination of X_{TGT} and Y_{TGT}.) These cuts eliminated any tracks originating from upstream of the beam dumps, as well as any hadrons which might have been produced in the beryllium but travelled around the dump.

The energy loss correction was based on the most likely energy lost by the muon in traversing the entire 4 m copper dump. This correction was tuned with Monte-Carlo data to ensure that no bias in x_F was introduced. At each point in the traceback, the track was tested to see whether it was currently inside or outside the beam dump. For each step in which the track was inside the copper dump, a fraction of the total estimated energy loss, proportional to the step size, was added back to the muon energy.

To correct for the effects of multiple scattering, a transverse constraint was applied to each track. After the initial traceback, the intercepts of the track at Z_{TGT} were compared with the beam centroid,

$$\begin{pmatrix} \Delta X \\ \Delta Y \end{pmatrix} = \begin{pmatrix} X_{TGT} - X_0 \\ Y_{TGT} - Y_0 \end{pmatrix}. \tag{3.1}$$

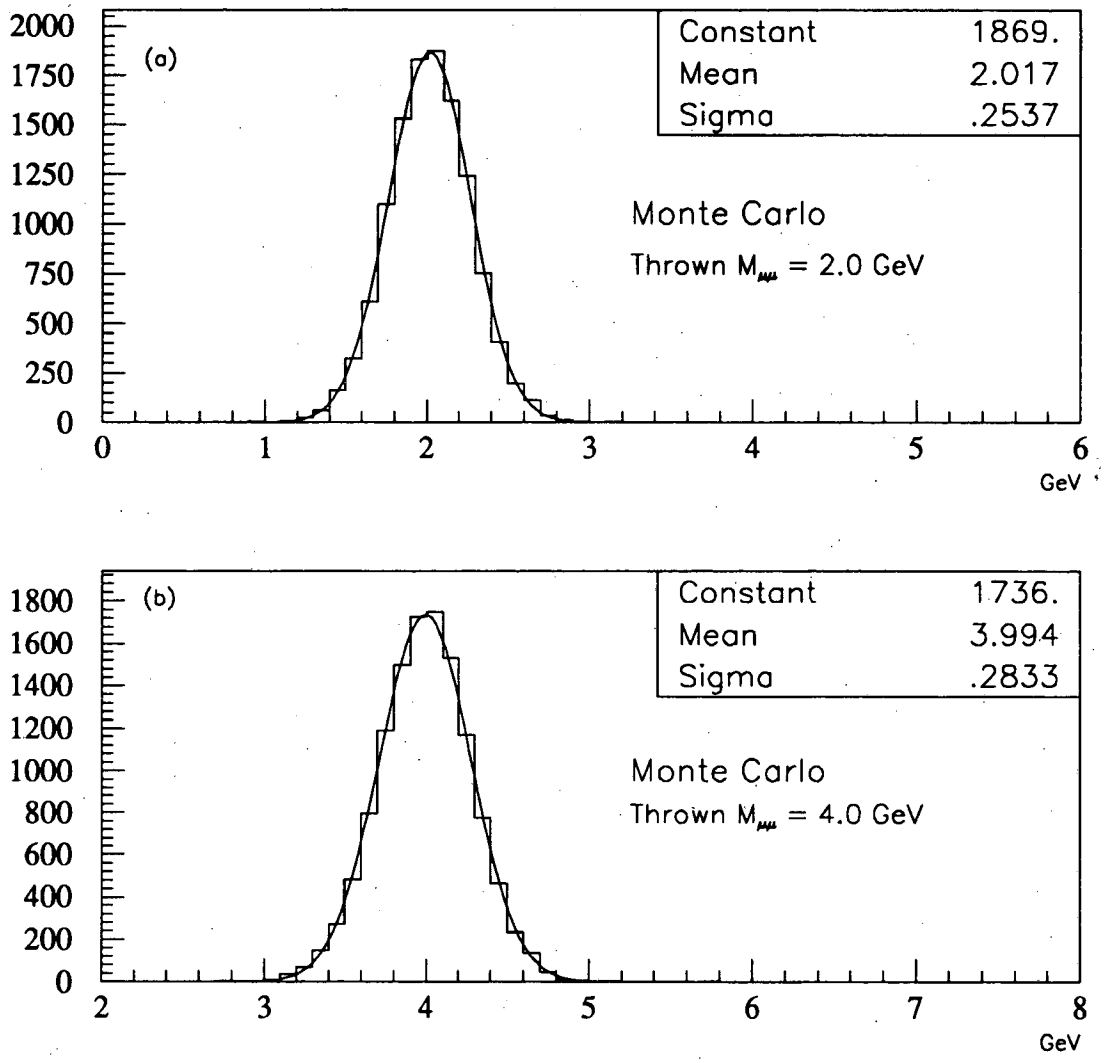

Figure 3.3: Reconstructed dimuon mass of Monte Carlo events. (a) shows the reconstructed mass spectrum for Monte Carlo dimuons generated with $m_{\mu\mu} = 2.0$ GeV, while (b) shows the one for $m_{\mu\mu} = 4.0$ GeV. The inset values are from a gaussian fit.

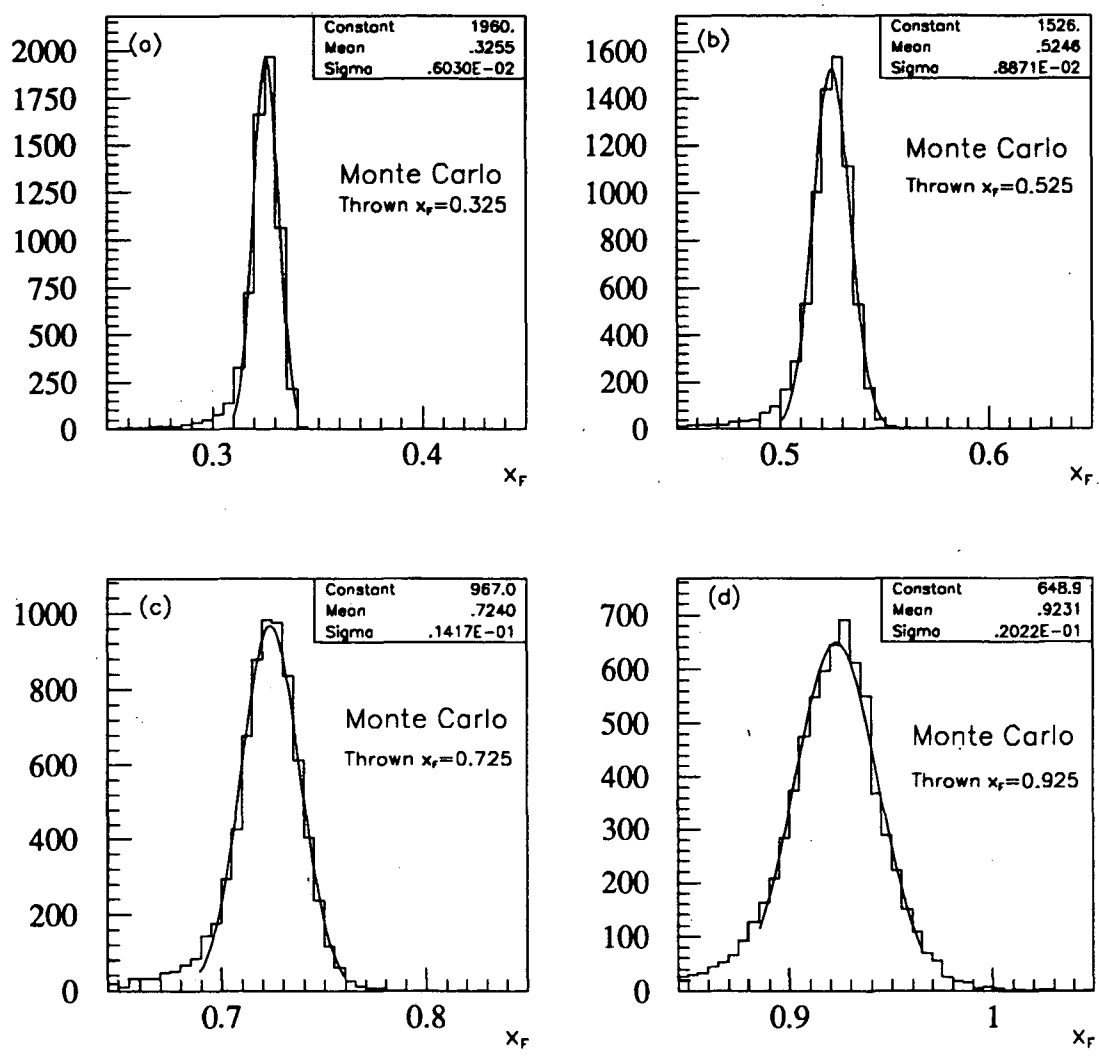

Figure 3.4: Reconstructed x_F of Monte Carlo events. (a)–(d) show the reconstructed values of x_F for Monte Carlo $J/\psi \rightarrow \mu^+\mu^-$ events generated with $x_F = 0.325, 0.525, 0.725, 0.925$. The inset values are from a gaussian fit. Notice the presence of a non-gaussian tail on the low-x_F side of each distribution as well as the increased width of the distributions going from (a) to (d). These effects can be understood in terms of the growing fluctuations in the energy loss process in traversing the beam dump. See also Figure 2.2.

Based on these differences, an angular correction to the track direction was calculated at an effective scattering plane located at Z_{SCAT}, near the downstream end of the beam dump,

$$\begin{pmatrix} \Delta\theta_X \\ \Delta\theta_Y \end{pmatrix} = \frac{1}{Z_{TGT} - Z_{SCAT}} \begin{pmatrix} \Delta X \\ \Delta Y \end{pmatrix}. \tag{3.2}$$

The track was then rolled back to its state at Z_{SCAT}. After the angular correction was applied, the track was traced again to Z_{TGT}. The intercept errors (3.1) became negligible after one iteration. The value of Z_{SCAT} was determined by optimizing the mass resolution for real data (see Figure 3.5). Based on Figure 3.5, the value $Z_{SCAT} = 635\ cm$ was chosen for the reconstruction. The effect of the correction was to reduce the gaussian width of the J/ψ mass peak from ~400 MeV to ~270 MeV. This powerful technique was first developed by John Rutherfoord of the E605 collaboration [see, e.g., 31].

3.2.2 Physics Variables

After tracing both muon tracks back to the effective target point with energy loss and multiple scattering corrections, physics variables of the event were calculated. The 4–momentum was determined for each muon track using the reconstructed 3–momentum and the muon mass assumption $m_\mu = 0.1057$ GeV.

$$p_{\mu+} = (\vec{p}_{\mu+}, \sqrt{|\vec{p}_{\mu+}|^2 + m_\mu^2}) \tag{3.3}$$

$$p_{\mu-} = (\vec{p}_{\mu-}, \sqrt{|\vec{p}_{\mu-}|^2 + m_\mu^2}) \tag{3.4}$$

These 4–momenta were then combined to form the 4–momentum of the pair,

$$p = p_{\mu+} + p_{\mu-} = (\vec{p}, E). \tag{3.5}$$

The invariant mass of the pair was given by

$$m_{\mu\mu}^2 = p_\alpha p^\alpha = E^2 - |\vec{p}|^2. \tag{3.6}$$

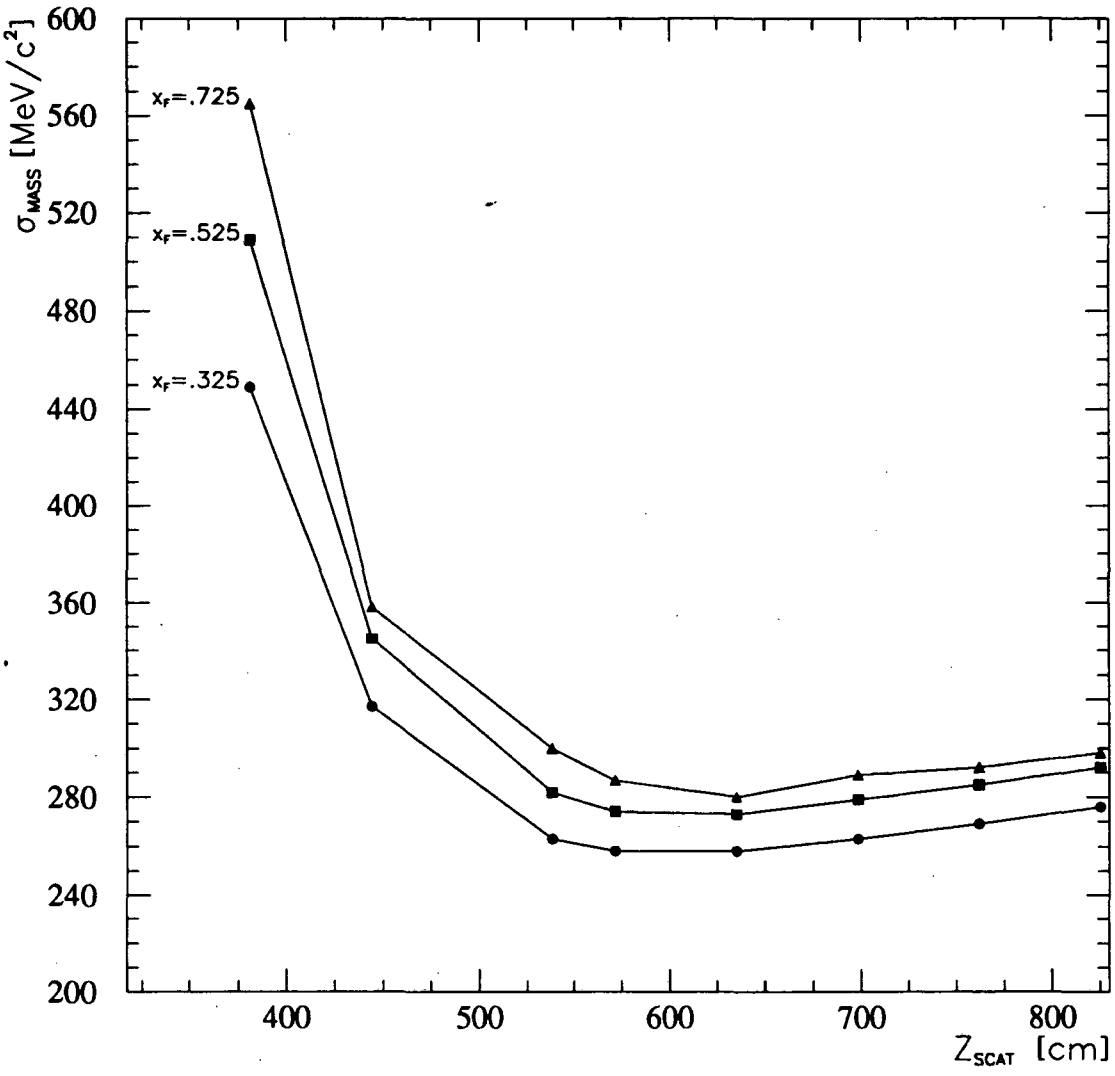

Figure 3.5: Optimization of Z_{SCAT} with data from the copper dump running. σ_{mass} is the standard deviation of the the gaussian distribution fitted to the reconstructed mass peak. Three values of x_F are shown as a function of Z_{SCAT}, in cm.

The transverse and longitudinal momenta ($\vec{p}_\perp$, p_L) of the pair were calculated with respect to the proton beam, which was deflected slightly by the magnetic field of SM12. Using the unit vector $\hat{e}_B$ along the beam direction, the transverse momentum $\vec{p}_\perp$ was

$$\vec{p}_\perp = \vec{p} - \hat{e}_B(\hat{e}_B \cdot \vec{p}), \tag{3.7}$$

while the longitudinal momentum p_L was

$$p_L = \hat{e}_B \cdot \vec{p} \tag{3.8}$$

To calculate x_F for the event, the pair 4–momentum was Lorentz boosted from the laboratory frame into the beam-target center-of-mass frame. For both beryllium and copper running, the target mass was taken to be an effective nucleon mass, $m_T = (Z/A)m_p + ((A-Z)/A)m_n \approx (4/9)m_p + (5/9)m_n = 0.9390\text{GeV}$. The effects of Fermi motion and binding energy of the target nucleon were neglected. With the beam momentum $\vec{p}_B = (800\text{GeV})\hat{e}_B$ and energy $E_B = \sqrt{|\vec{p}_B|^2 + m_p^2}$, the 4-momentum of the center-of-mass was

$$p_{CM} = (\vec{p}_{CM}, E_{CM}) = (\vec{p}_B, E_B + m_T). \tag{3.9}$$

The total energy squared in the center-of-mass frame was

$$S = (p_{CM})_\alpha (p_{CM})^\alpha = (E_B + m_T)^2 - |\vec{p}_B|^2 = (38.78\text{GeV})^2. \tag{3.10}$$

The Lorentz factor and velocity for the center-of-mass system in the laboratory frame were then

$$\gamma_{CM} = \frac{E_{CM}}{\sqrt{S}} = \frac{(E_B + m_T)}{\sqrt{S}} = 20.65 \tag{3.11}$$

and

$$\vec{\beta}_{CM} = \beta_{CM}\hat{e}_B = \frac{\vec{p}_{CM}}{E_{CM}} = 0.9988\hat{e}_B. \tag{3.12}$$

Denoting the 4-momentum of the dimuon in the center-of-mass frame by p^*, with

$$p^* = (\vec{p}^*, E^*) \ , \ \vec{p}^* = p_L^* \hat{e}_B + \vec{p}_\perp^*, \tag{3.13}$$

p^* was related to p by the Lorentz transformation

$$\begin{pmatrix} E^* \\ p_L^* \end{pmatrix} = \begin{pmatrix} \gamma_{CM} & -\gamma_{CM}\beta_{CM} \\ -\gamma_{CM}\beta_{CM} & \gamma_{CM} \end{pmatrix} \begin{pmatrix} E \\ p_L \end{pmatrix} \ , \ \vec{p}_\perp^* = \vec{p}_\perp, \tag{3.14}$$

After transforming to the center-of-mass system, x_F of the dimuon was calculated from the definition

$$x_F = \frac{p_L^*}{(p_L^*)_{max}}. \tag{3.15}$$

The quantity $(p_L^*)_{max}$ was calculated with the final state masses taken into account. The dimuon had an invariant mass $m_{\mu\mu}$, while the minimum mass of the recoil system was required by baryon number conservation to be $2m_p$. Thus, we have

$$(p_L^*)_{max} = \frac{\sqrt{(S-(m_{\mu\mu}+2m_p)^2)(S-(m_{\mu\mu}-2m_p)^2)}}{2\sqrt{S}}. \tag{3.16}$$

For $m_{\mu\mu} = m_{J/\psi}$, this gave $(p_L^*)_{max} = 19.222\text{GeV}$. This should be compared with the approximation $(p_L^*)_{max} \approx \sqrt{S}/2 = 19.391\text{GeV}$. Thus, the values of x_F calculated here were 1% greater than that obtained by neglecting all final state masses.

As can be seen from the Monte Carlo results shown in Figure 3.4, the x_F resolution degraded with increasing x_F. This was due to the increasing fluctuations in the muon energy loss in the beam dump. As $x_F \to 1$, the statistical uncertainty in x_F was about 0.02. Based on this, the binning in x_F was chosen to be $\Delta_{x_F} = 0.05$.

For each event, an entry was made in a 2-dimensional histogram binned by mass and x_F. This histogram was written to a disk file at the end of Pass-2 for final analysis with the interactive program, PAW.

3.2.3 Study Runs

In addition to the main analysis runs of Pass–2, study runs were performed to determine the beam direction and centroid. The beam direction $\hat{e}_B$ was determined from the distributions of θ_X and θ_Y in the spectrometer frame with high x_F dimuon pairs. Monte Carlo studies confirmed that the spectrometer acceptance was sufficiently symmetric for this to be an unbiased estimator of the true beam direction. Similarly, the beam centroid position (X_{TGT}, Y_{TGT}) at the effective target plane was determined from the distribution of the uniterated track intercepts. Figure 3.6 shows the results of these studies.

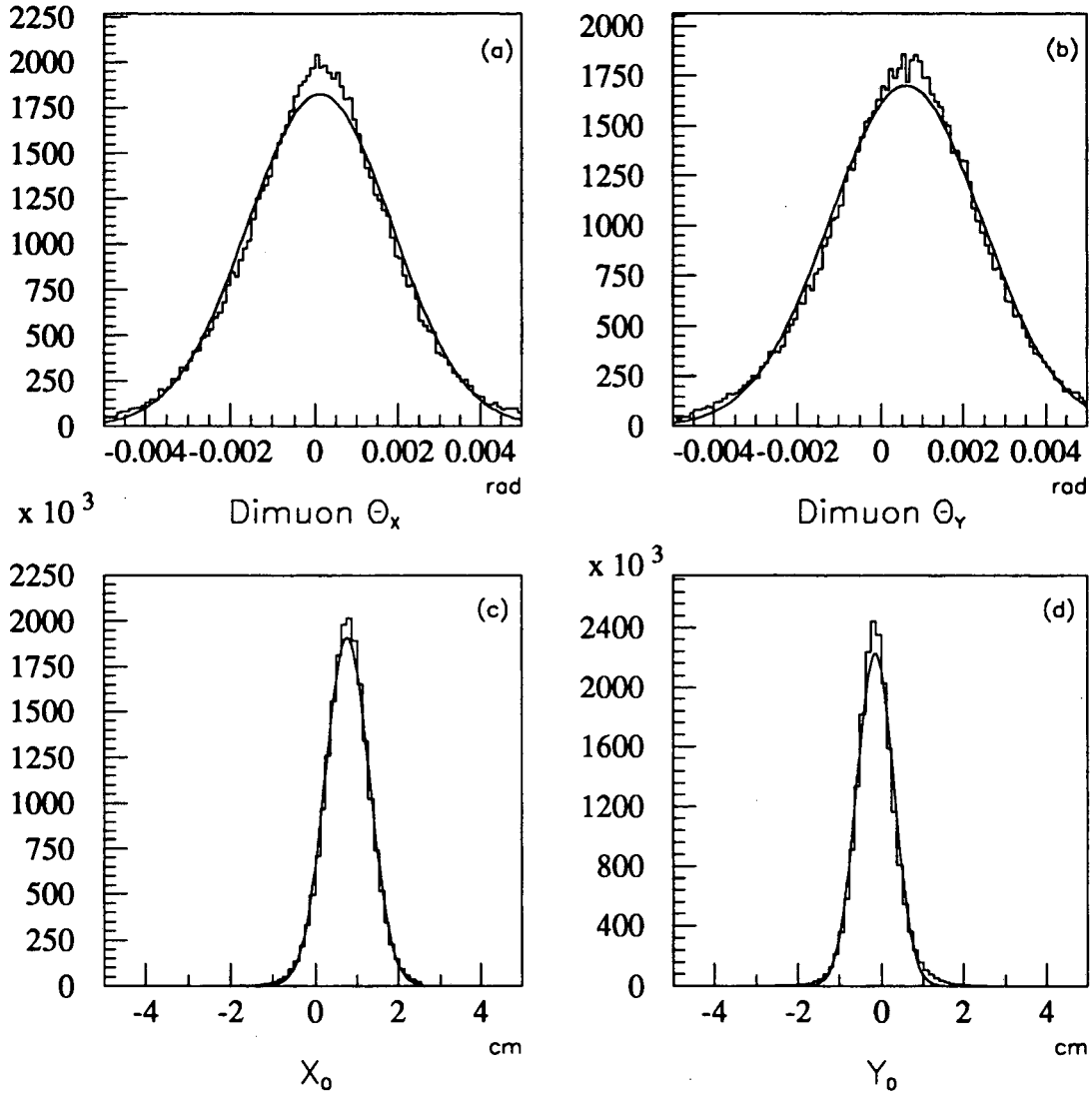

Figure 3.6: Survey of beam direction and beam centroid. (a) and (b) show the distibutions of dimuon directions θ_X and θ_Y at the nominal target plane, Z_{TGT}, for all pairs with $x_F > 0.5$. (c) and (d) show the uncorrected track intercepts, X_0 and Y_0, at Z_{TGT}. The fitted curves were only used to determine the centroids of the distributions. For (a) and (b) this determined the beam direction $\hat{e}_B$, while for (c) and (d) this determined X_{TGT} and Y_{TGT}.

3.3 Cut Summary

Table 3.1 summarizes the number of events surviving each stage of the Pass–1 and Pass–2 analysis for the copper dump and beryllium dump runs. The various cuts were:

Pass–1

Tracking: Tracks were required to have hits in at least 14 out of the 18 drift chamber planes and a fit quality of $\chi^2/\mathrm{NDF} < 5$.

Muon ID: Tracks not satisfying the muon identification requirements of § 2.4.3 were eliminated.

Track Quality: Each track was required to have a momentum in the range $20 < |\vec{p}| < 800$ GeV, and to have fired least three hodoscopes. Events with less than two quality tracks failed this cut.

2 Tracks: Events with more than two tracks were written to a separate output stream, and were not further considered in this study.

Pass–2

Opposite Sign: The two muon tracks were required to have opposite charges at this point.

Target Cuts: Each track was required to trace back through at least 1 meter of copper in the beam dump, and to intercept the nominal target plane Z_{TGT} within 3 standard deviations from the beam centroid.

Hodoscope Fiducials: Each event was required to have the hodoscope fiducial bit set, as described in § 3.1.4.

Table 3.1: Cut Summary

	— Copper —		— Beryllium —	
Cut	Pass	Fail	Pass	Fail
Triggers				
	1.64×10^7		1.20×10^7	
Pass–1				
Tracking	1.16×10^7	4.80×10^6	5.78×10^6	6.26×10^6
Muon ID	1.15×10^7	7.80×10^4	5.26×10^6	5.16×10^5
Track Quality	1.04×10^7	1.18×10^6	4.26×10^6	1.00×10^6
2 Tracks	1.03×10^7	1.01×10^5	4.23×10^6	3.20×10^4
Pass–2				
Opposite Sign	1.00×10^7	2.89×10^5	4.06×10^6	1.73×10^5
Target Cuts	9.46×10^6	5.42×10^5	3.65×10^6	4.03×10^5
Hodoscope Fiducials	7.47×10^6	2.00×10^6	2.72×10^6	9.33×10^5

3.4 Pass–3: PAW

The final pass in the analysis chain was performed with the Physics Analysis Workstation program, PAW [32]. This program allowed easy manipulation of histogram files created in Pass–2 with the HBOOK library [33], and provided a simple way to prepare graphical output of results. Extensive use of the macro programming features of PAW was made to perform fits to large sets of histograms in a simple, consistent way.

At its essence, measuring a differential cross-section comes down to counting events. J/ψ events produced in the beam dump were observed through the exclusive decay mode $J/\psi \rightarrow \mu^+\mu^-$. To count the number of J/ψ events in a given kinematic bin, the invariant mass of the dimuon events in that kinematic bin were plotted. A clear peak in the mass spectrum at $m_{J/\psi} = 3.1$ GeV, as can be seen in Figure 3.7, indicated the presence of J/ψ's. The task at this stage was to quantify the number of signal events in that peak.

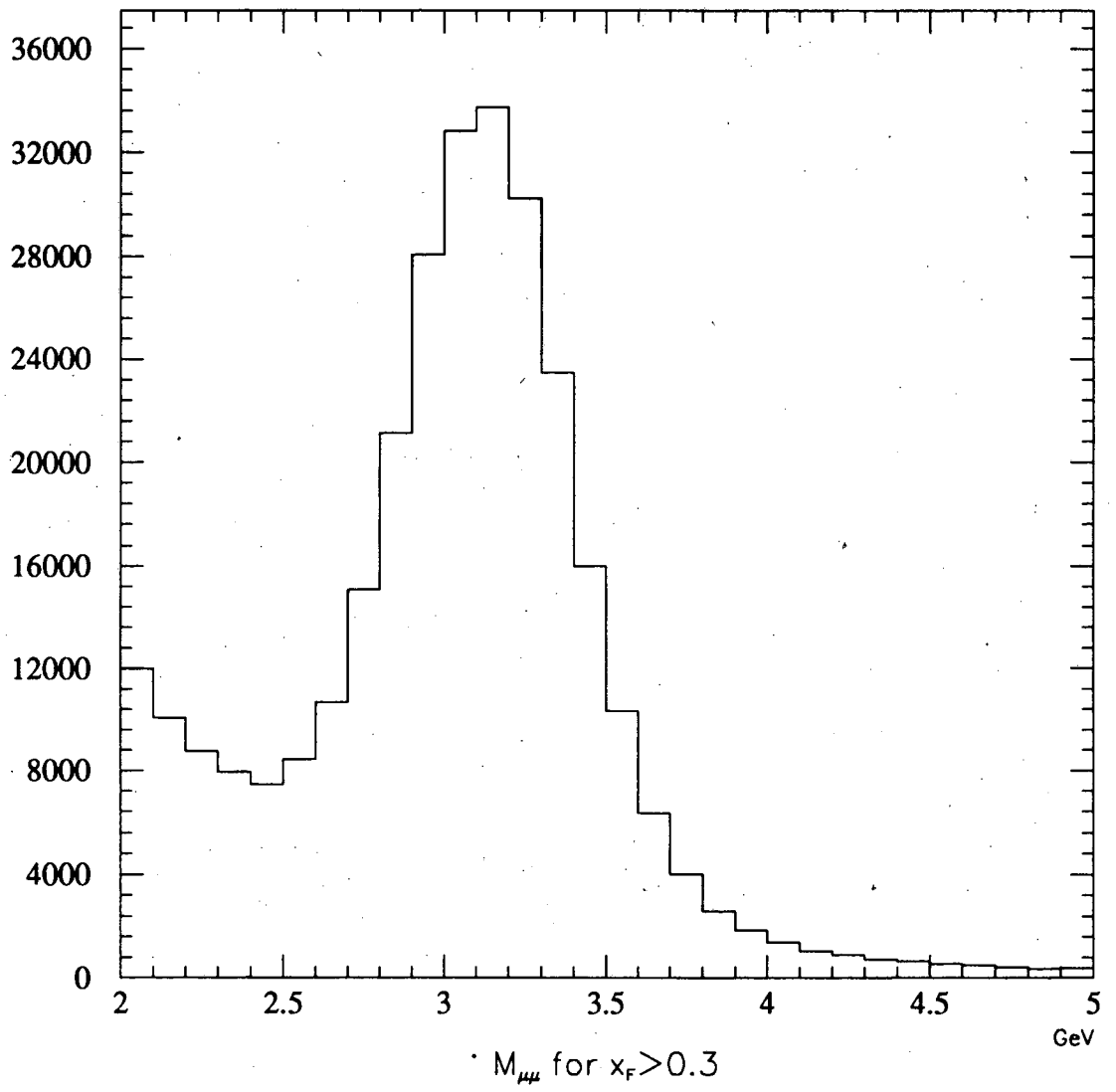

Figure 3.7: Invariant $\mu^+\mu^-$ mass spectrum of events with $x_F > 0.3$ in p+Cu collisions.

3.4.1 Beam Punch-Through in Beryllium

For the beryllium data, the first step in the PAW analysis was to correct for the effect of punch-through of beam protons. The 91 cm long beryllium target constituted 2.2 interaction lengths. Thus, about 10% of the beam protons passed through the beryllium without interacting, and were subsequently absorbed in the copper beam dump. Some of these punch-through protons would produce J/ψ events in the copper, and so a subtraction scheme was needed to correct for this. To estimate the contamination of the beryllium data due to events produced inside the copper dump, a special Pass–2 run was performed. Events taken from the copper-only data set were subjected to the beryllium data reconstruction procedure. The resulting distribution in $m_{\mu\mu}$ and x_F was rescaled to correspond to the fraction of the beam flux which punched through the beryllium. This estimate of the punch-through contamination was then subtracted from the beryllium data. Figure 3.8 shows this subtraction for a typical bin in x_F. The punch-through background events were reconstructed with smaller opening angles between the muons in the beryllium data reconstruction procedure, leading to a broad invariant mass distribution that was shifted away from the nominal value of $m_{J/\psi}$.

3.4.2 Fits to the Mass Spectra

The background continuum of dimuons in the vicinity of the J/ψ peak were fitted to an exponential, whereas Monte-Carlo studies showed that the J/ψ peak itself was consistent with a gaussian. Therefore, the mass spectrum of each bin in x_F was fitted to a function of the form

$$N(m_{\mu\mu}) = \exp(a + bm_{\mu\mu}) + \frac{N_{fit}\Delta_m}{\sigma_{fit}\sqrt{2\pi}} \exp\left[-\frac{(m_{\mu\mu} - m_{fit})^2}{2\sigma_{fit}^2}\right] \qquad (3.17)$$

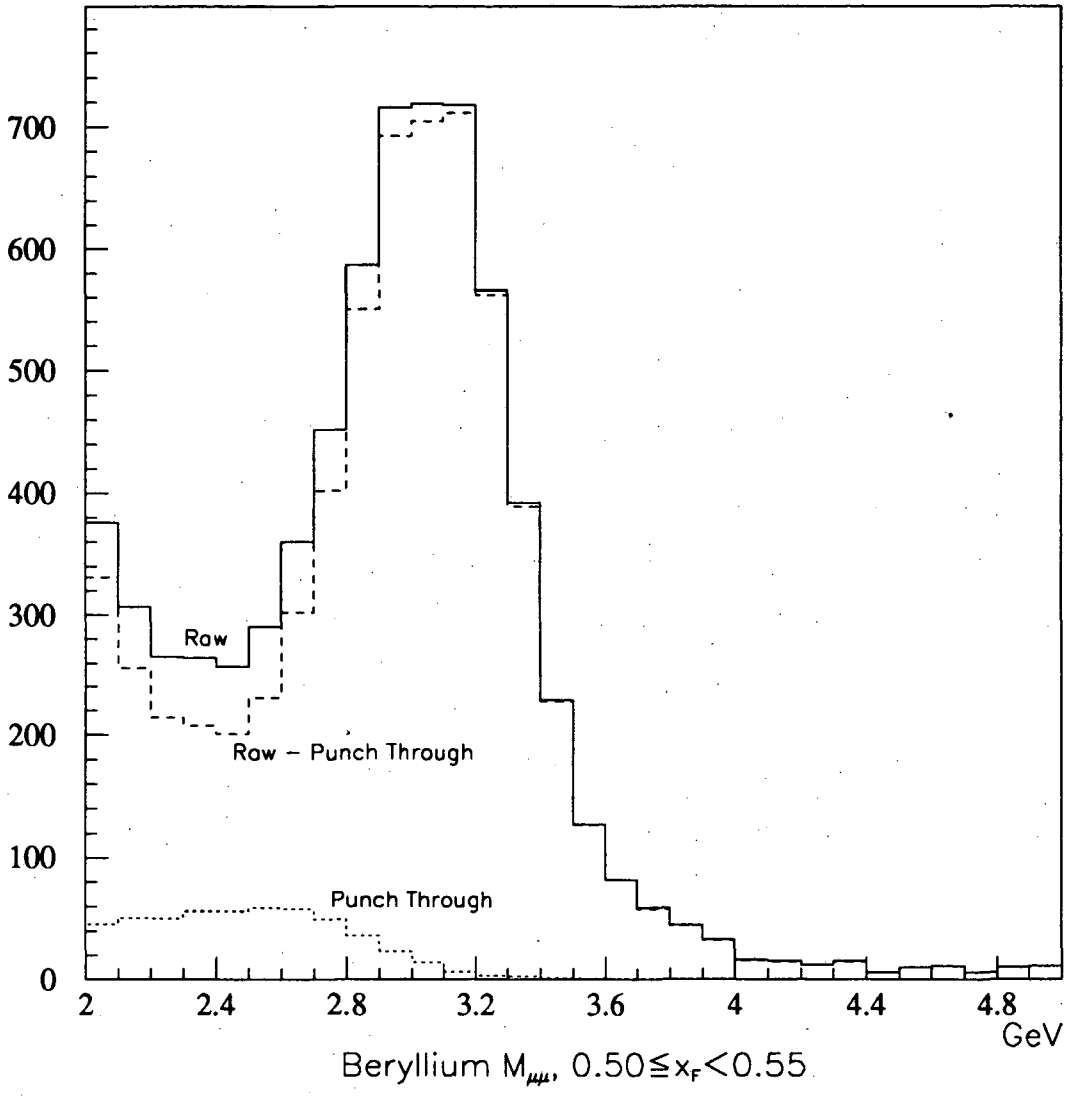

Figure 3.8: Correction for punch-through in beryllium. The solid line shows the invariant dimuon mass obtained directly from the beryllium dump, for $0.50 < x_F < 0.55$. The dotted line shows the estimate of contamination in the beryllium data due to protons that punched through into the copper dump, while the dashed line shows the result of subtracting this estimated contamination from the raw beryllium mass spectrum.

where $N(m_{\mu\mu})$ is the number of events reconstructed with the invariant mass in the interval $(m_{\mu\mu} - \frac{\Delta_m}{2}) \leq m < (m_{\mu\mu} + \frac{\Delta_m}{2})$, and a, b, m_{fit}, σ_{fit}, and N_{fit} are free parameters of the fit. The binning Δ_m was fixed at 100 MeV. Casting the gaussian in this form, N_{fit} gave the number of J/ψ events as determined by the fit. Fits were performed using the method of maximum likelihood to the data in the mass region $2.0 < m_{\mu\mu} < 5.0$ GeV. The results of the fits to the copper and beryllium dump data are shown in Figures 3.9 - 3.16. The obtained value of N_{fit} was then taken as the signal for that kinematic bin. Note that events in the copper data with $x_F > 0.95$, and in the beryllium data with $x_F > 0.90$, are not considered in the analysis because of poor statistics.

3.5 Monte Carlo

To convert the number of reconstructed J/ψ events to the number produced in the beam dump, the overall acceptance and efficiency must be determined. This was accomplished with a Monte-Carlo simulation of the spectrometer. $J/\psi \rightarrow \mu^+\mu^-$ events were generated in the target. The decay muons were traced through a detailed model of the spectrometer. The trigger conditions, described in § 2.5, were then imposed on the events. For the surviving events, the detector hit information was packed into the raw data format of the readout and written to disk. This output was then analyzed by the same Pass-1 and Pass-2 codes used for the real data. The efficiency of the reconstruction program and the effect of the event selection process could then be studied with the Monte Carlo events.

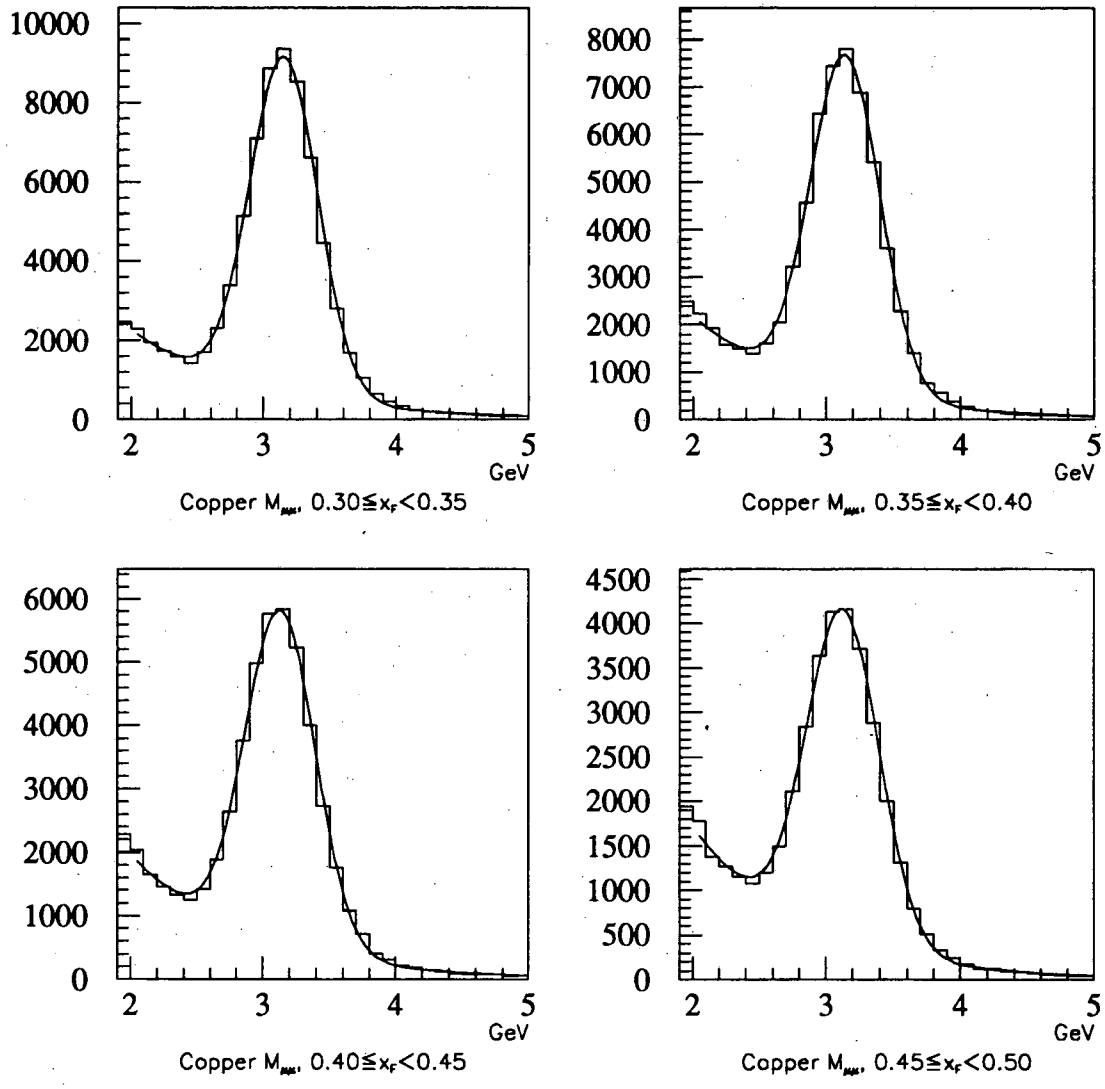

Figure 3.9: Fits to dimuon mass spectra with $0.3 < x_F < 0.5$, for the copper dump data. The ordinate shows the number of events per 100 MeV bin.

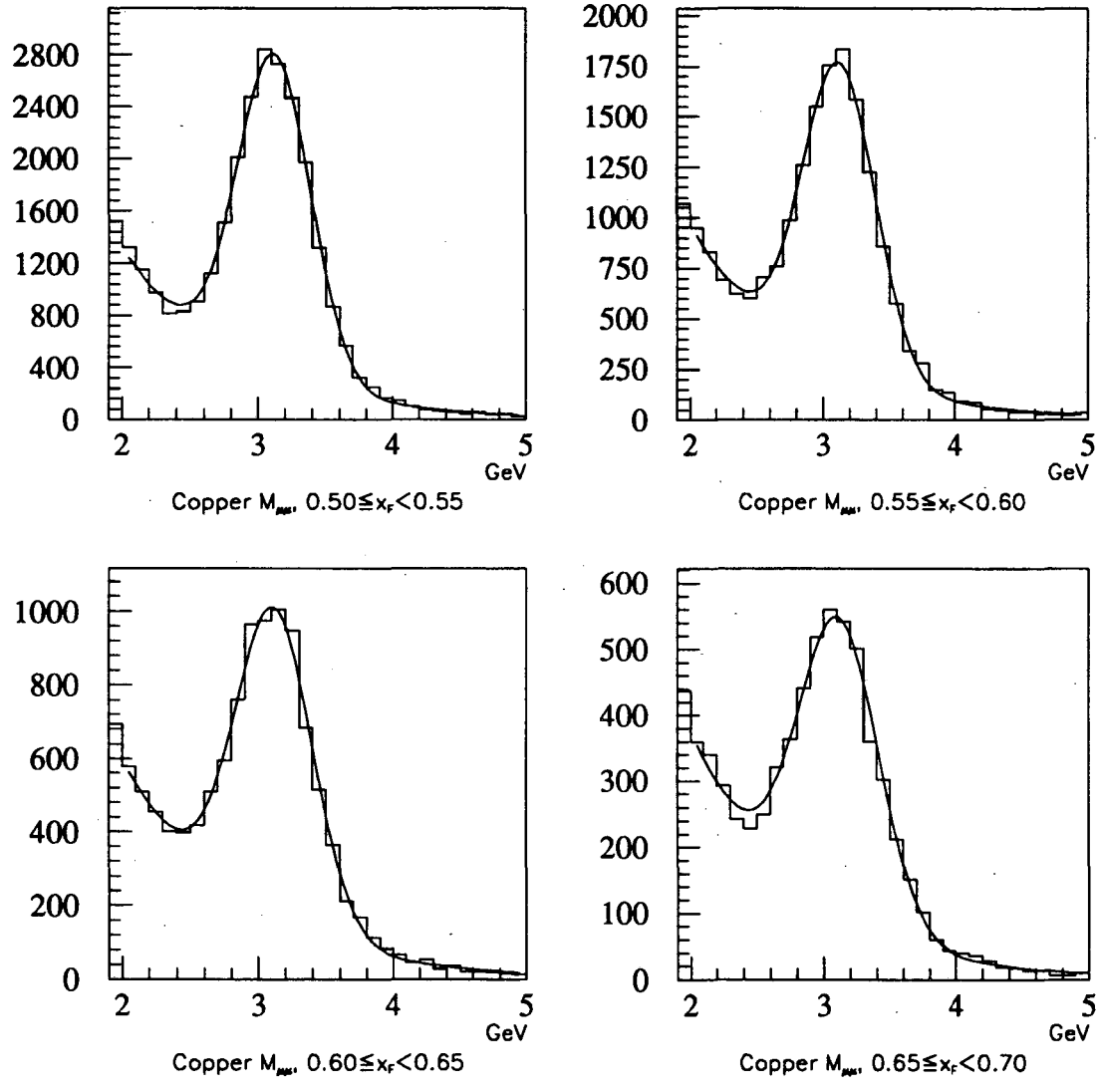

Figure 3.10: Fits to dimuon mass spectra with $0.5 < x_F < 0.7$, for the copper dump data. The ordinate shows the number of events per 100 MeV bin.

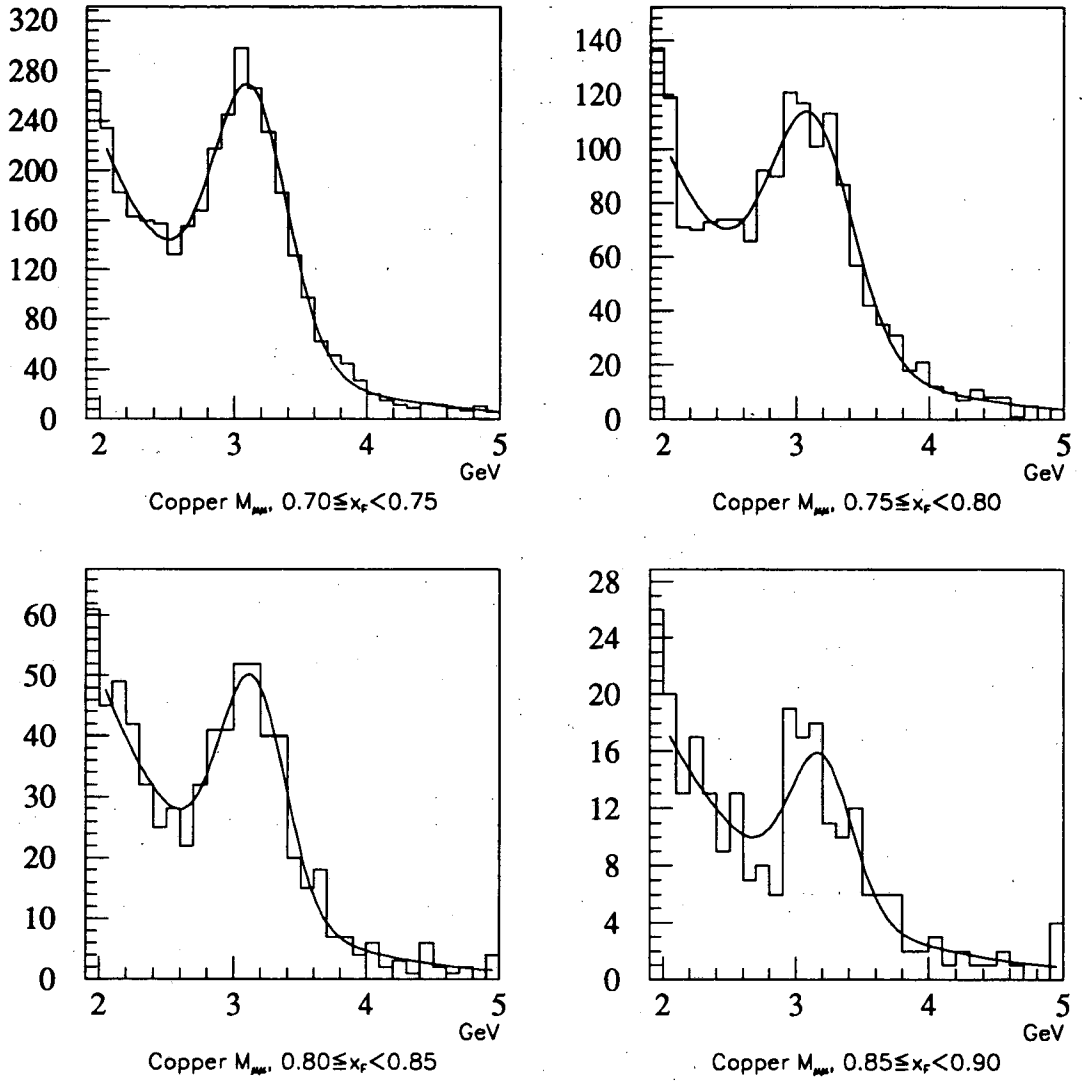

Figure 3.11: Fits to dimuon mass spectra with $0.7 < x_F < 0.9$, for the copper dump data. The ordinate shows the number of events per 100 MeV bin.

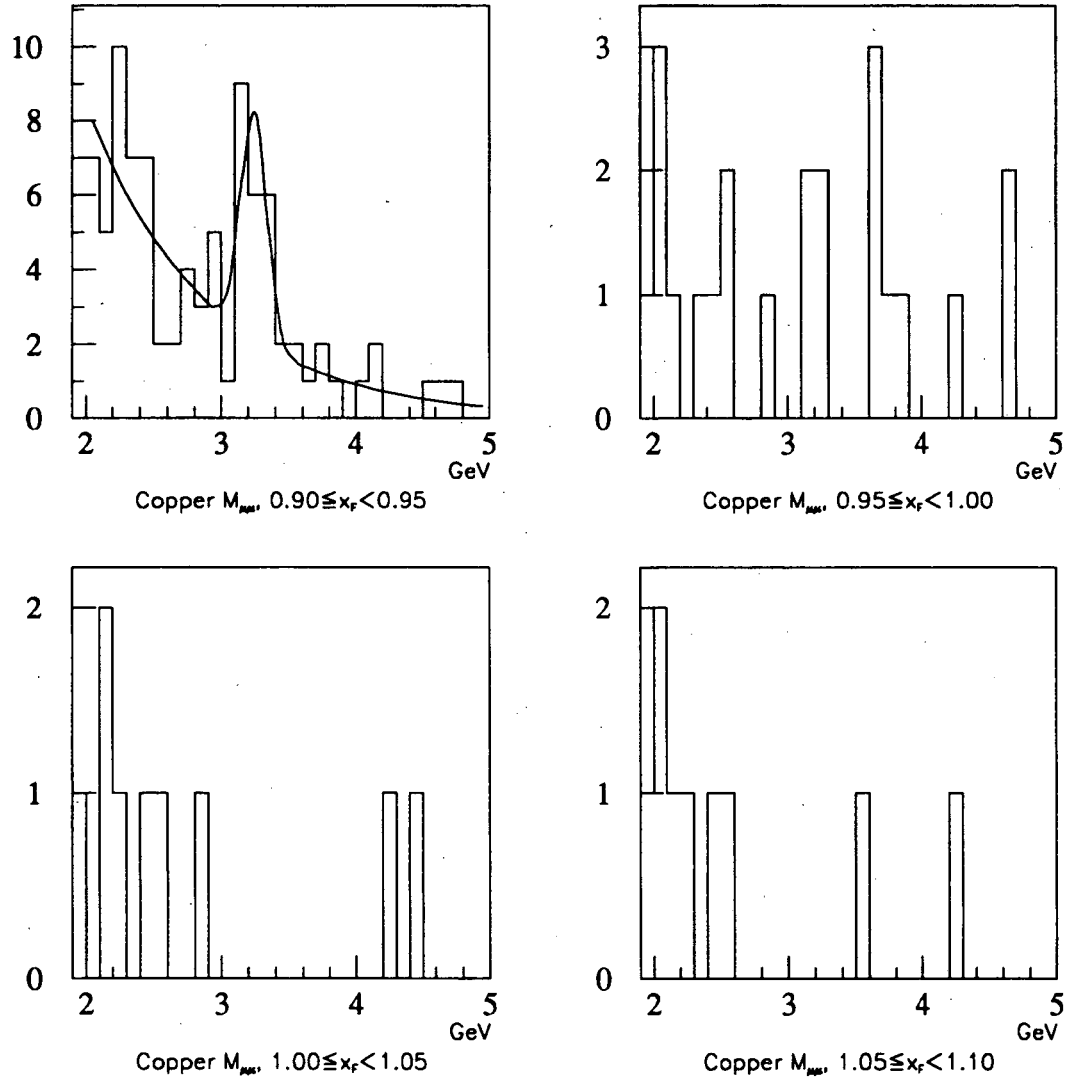

Figure 3.12: Fits to dimuon mass spectra with $x_F > 0.9$, for the copper dump data. The ordinate shows the number of events per 100 MeV bin.

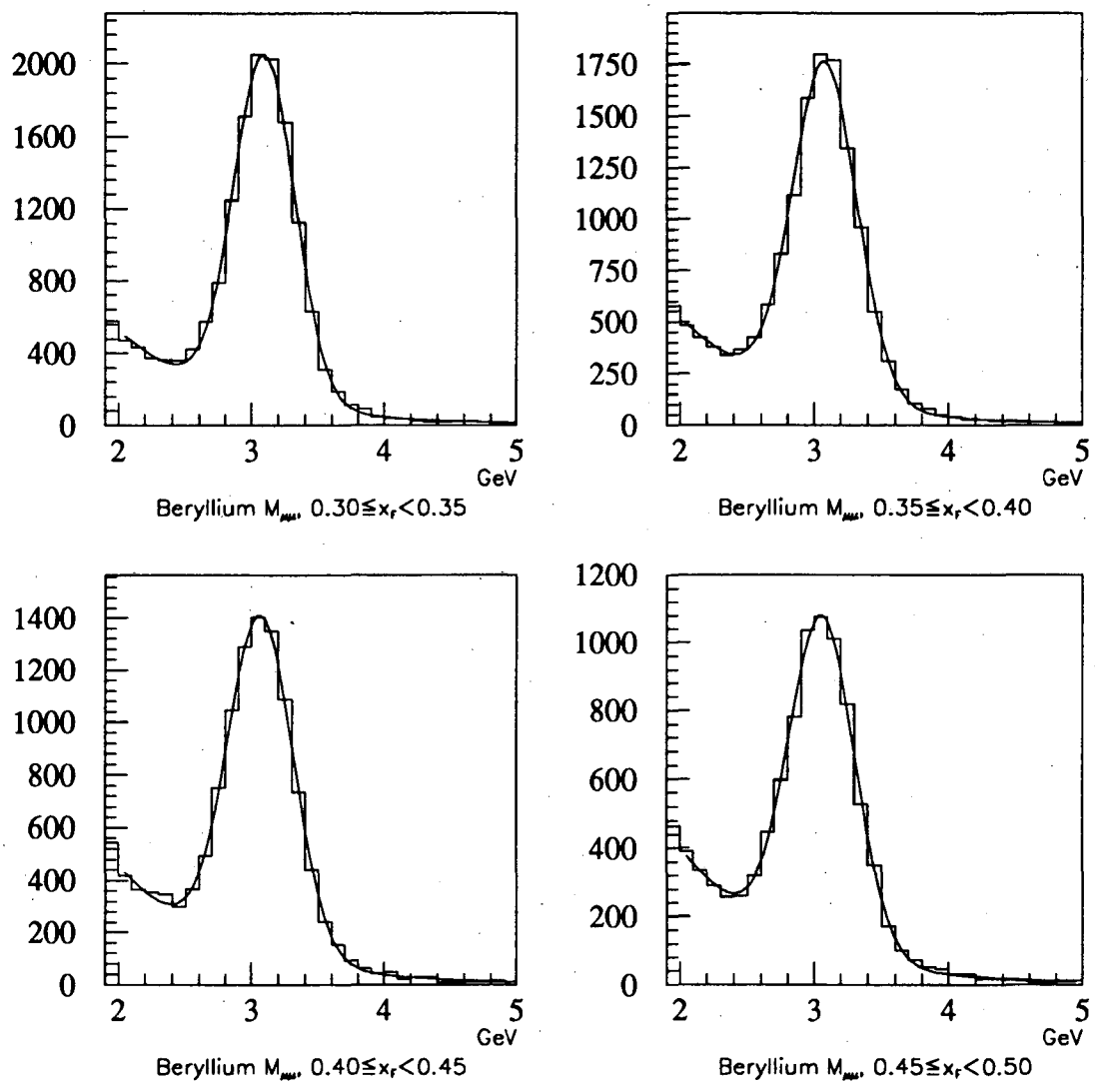

Figure 3.13: Fits to dimuon mass spectra with $0.3 < x_F < 0.5$, for the beryllium dump data. The ordinate shows the number of events per 100 MeV bin.

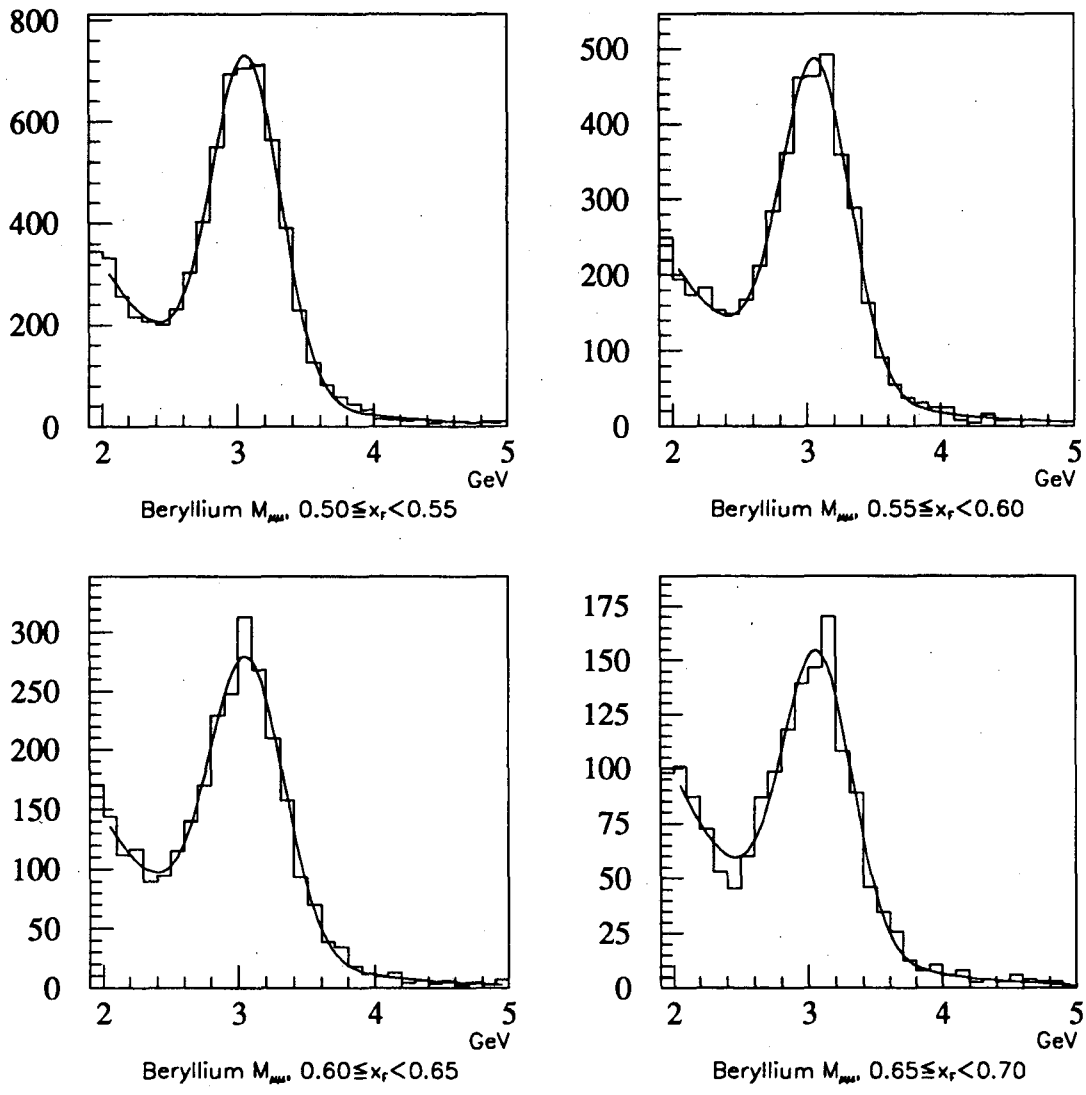

Figure 3.14: Fits to dimuon mass spectra with $0.5 < x_F < 0.7$, for the beryllium dump data. The ordinate shows the number of events per 100 MeV bin.

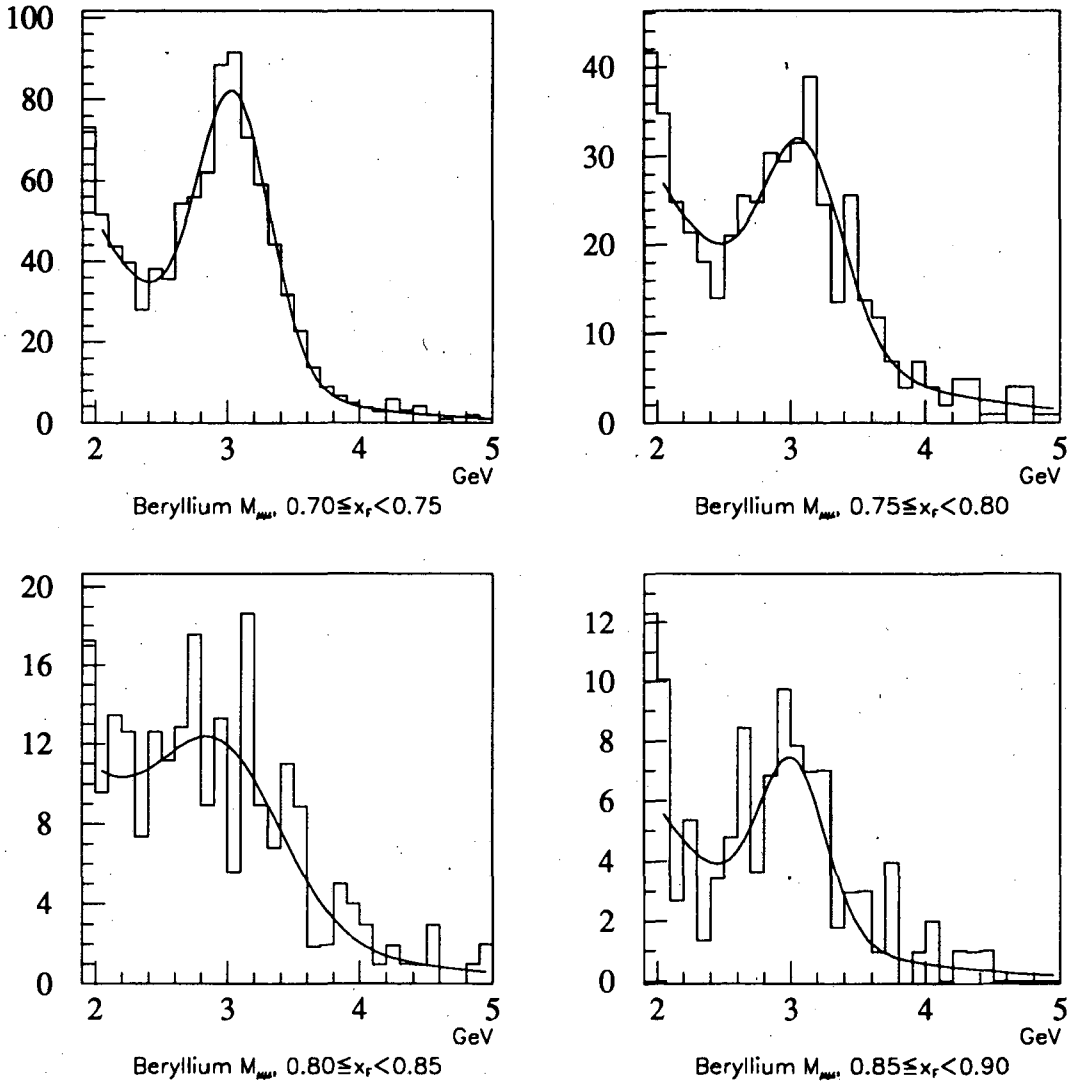

Figure 3.15: Fits to dimuon mass spectra with $0.7 < x_F < 0.9$, for the beryllium dump data. The ordinate shows the number of events per 100 MeV bin.

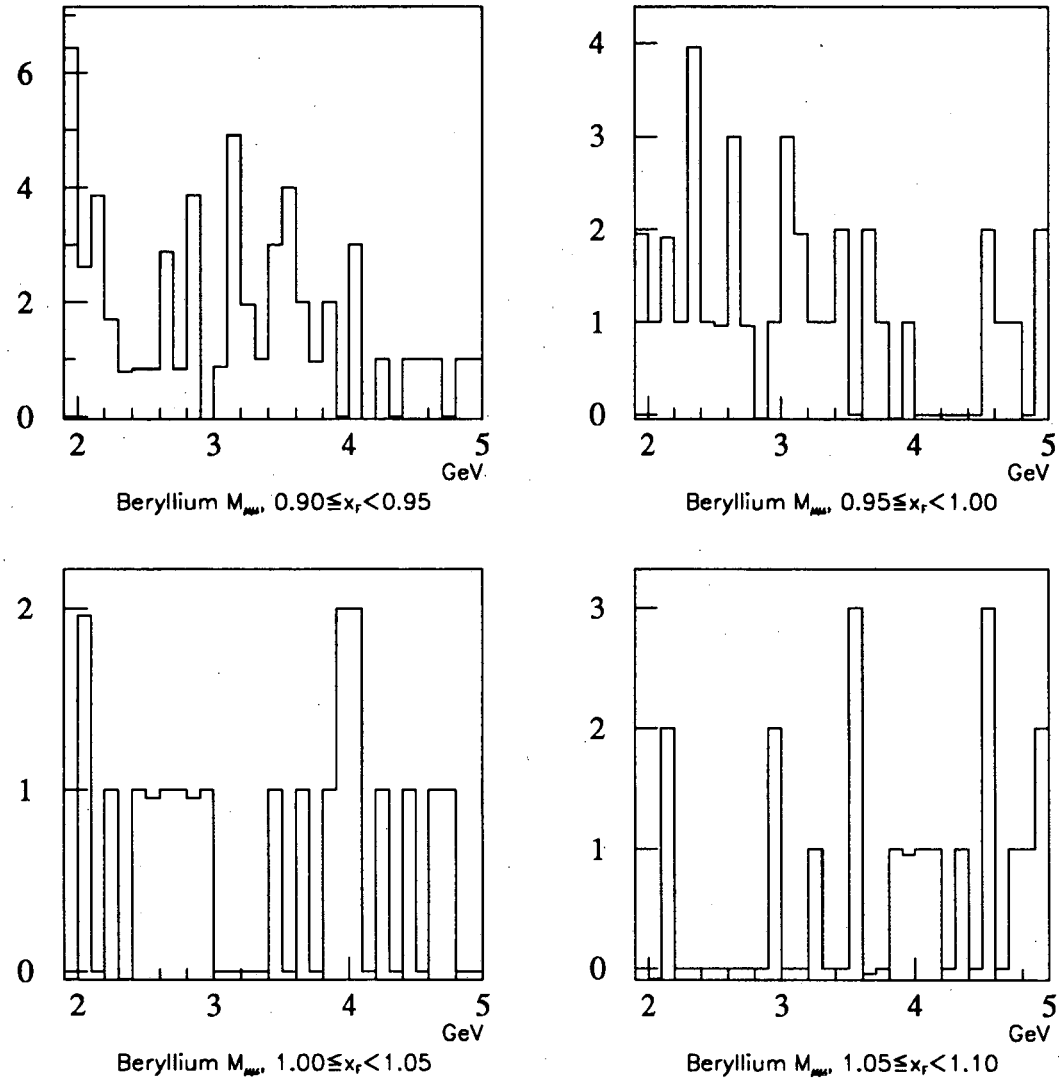

Figure 3.16: Dimuon mass spectra with $x_F > 0.9$, for the beryllium dump data. The ordinate shows the number of events per 100 MeV bin.

3.5.1 Event Generation

The first step in the simulation was the event generation. A grid scheme was used to generate x_F for the simulated J/ψ events, with each grid point corresponding to one of the bins of x_F. Within each bin, the value of x_F was varied according to the distribution found in the data. Since the binning in x_F was rather fine, the results were not very sensitive to the procedure.

The transverse momentum $p_\perp$ of the J/ψ was generated according to the distribution [34],

$$d\sigma(p_\perp) \propto \frac{p_\perp dp_\perp}{\left(1-\left(\frac{p_\perp}{p_0}\right)^2\right)^6}, \tag{3.18}$$

where the parameter p_0 was tuned so that the reconstructed $p_\perp$ distribution of the Monte Carlo agreed with that of the data. By fitting the reconstructed data and Monte Carlo $p_\perp$ distributions to the same form as equation (3.18), the agreement between data and Monte Carlo could be quantified in terms of p_0. The rms difference between the fitted values of p_0 from the data and the Monte Carlo was 4.3%. Figure 3.17 shows the comparison of the reconstructed $p_\perp$ distributions of the data and the Monte Carlo events. Monte-Carlo estimates showed that there was reasonable acceptance for forward J/ψ events with $p_\perp < 5$ GeV, although only a small fraction of the real events had $p_\perp > 4$ Gev.

A uniform distribution was assumed for the azimuth of $\vec{p}_\perp$. The $J/\psi \rightarrow \mu^+\mu^-$ decay was generated according to an isotropic angular distribution in the J/ψ rest frame [35].

3.5.2 Track Simulation

After generating the event, each muon from the J/ψ decay was traced forward through the spectrometer. While in the beam dump, the effects of energy loss and

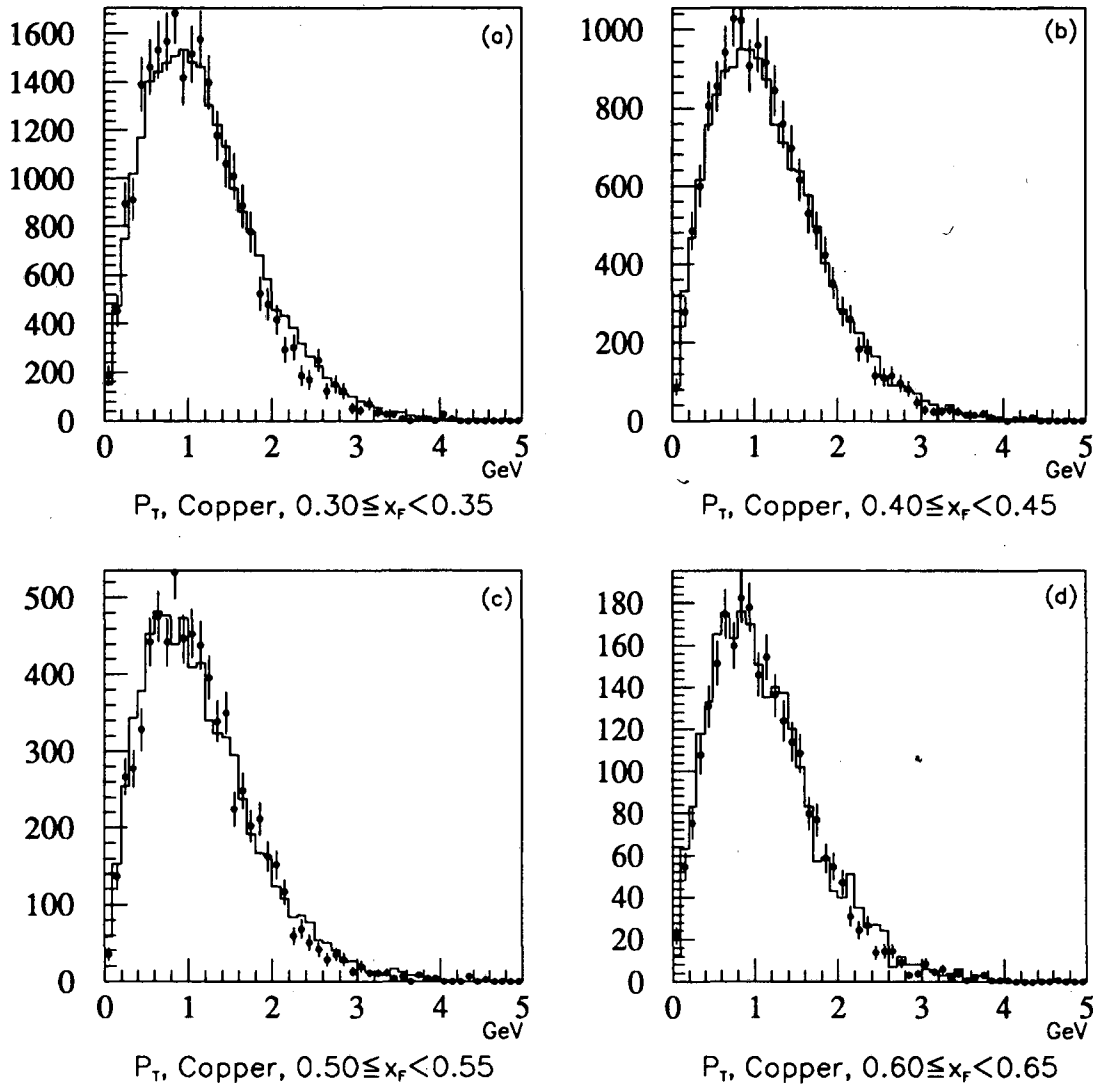

Figure 3.17: Reconstructed $p_\perp$ distributions for copper dump data and Monte Carlo events. (a) – (d) show x_F bins with mean x_F at 0.325, 0.425, 0.525, and 0.625. The solid line is data from the copper beam dump, and the points are reconstructed Monte Carlo events. Monte Carlo events were generated according to the distribution of equation (3.18), with $p_0 = 2.79$ GeV at low x_F, and slowly decreasing to $p_0 = 2.60$ GeV at $x_F = 0.925$.

multiple scattering were modeled using realistic distributions including non-gaussian tails (see, for example, Figure 2.2). Events in which one or both muons left the experimental aperture were discarded. The deflection of the muons by the magnetic field of SM12 was calculated using the Ziptrack field map. At each hodoscope and drift chamber plane, the X and Y intercept of the track was recorded for later use. Multiple scattering was simulated, accounting for the effects of traversing air, helium bags in the spectrometer, and scattering in the detector planes. The tracks were also scattered through the calorimeter and hadron absorbers. Hit locations of the tracks at the Station–4 detectors were recorded. The number of events surviving the simulation to this point, divided by the number of events thrown, gave the spectrometer acceptance for that kinematic bin.

3.5.3 Trigger Simulation

If both tracks were successfully traced through the spectrometer to the end of Station–4, hits in the hodoscope planes were digitized and the corresponding struck paddles determined. With a pseudo-random number, the experimentally measured efficiency for each paddle was used to decide whether the struck hodoscope paddle should be fired or not. After all the hodoscope planes had been digitized for both tracks, the trigger conditions described in § 2.5 were applied. Events that did not satisfy the trigger were discarded. The number of events surviving the simulation to this point, divided by the number of events thrown, gave the product of the spectrometer acceptance and the trigger efficiency.

3.5.4 Digitization and Readout Simulation

The next step was to digitize the hit information in the drift chambers for both tracks. The experimentally determined resolution of each chamber, determined from

the track residuals, was used to "smear" the exact hit location of the track before digitization. Again, detector efficiencies were modeled using the pseudo-random number technique. Dead wires were explicitly modeled independent of the quarter-by-quarter chamber efficiency. A similar procedure was used for the Station–4 proportional tubes.

Random hits were also thrown in all drift chambers and hodoscope planes according to the multiplicity and hit distributions observed in the data. Then all detector hit information, together with the trigger bit information, was packed according to the experimental readout format. The event was written to disk in "raw" format.

3.5.5 Reconstruction of Simulated Events

The analysis chain described in § 3.1 – 3.4 was then applied to the Monte Carlo "raw event" file, with the exception that no background distribution was used in the fits to the mass spectra. The overall (acceptance × trigger × reconstruction) efficiency, $\epsilon_{overall}$, was given by

$$\epsilon_{overall} = \frac{N_{recon}}{N_{thrown}} \tag{3.19}$$

where N_{recon} was the number of reconstructed Monte Carlo J/ψ events surviving the full analysis, and N_{thrown} was the number of events originally thrown. The overall acceptance for the copper and beryllium dump data are shown in Figures 3.18 and 3.19, with the smoothing done by fitting $\epsilon_{overall}$ to a third-order polynomial.

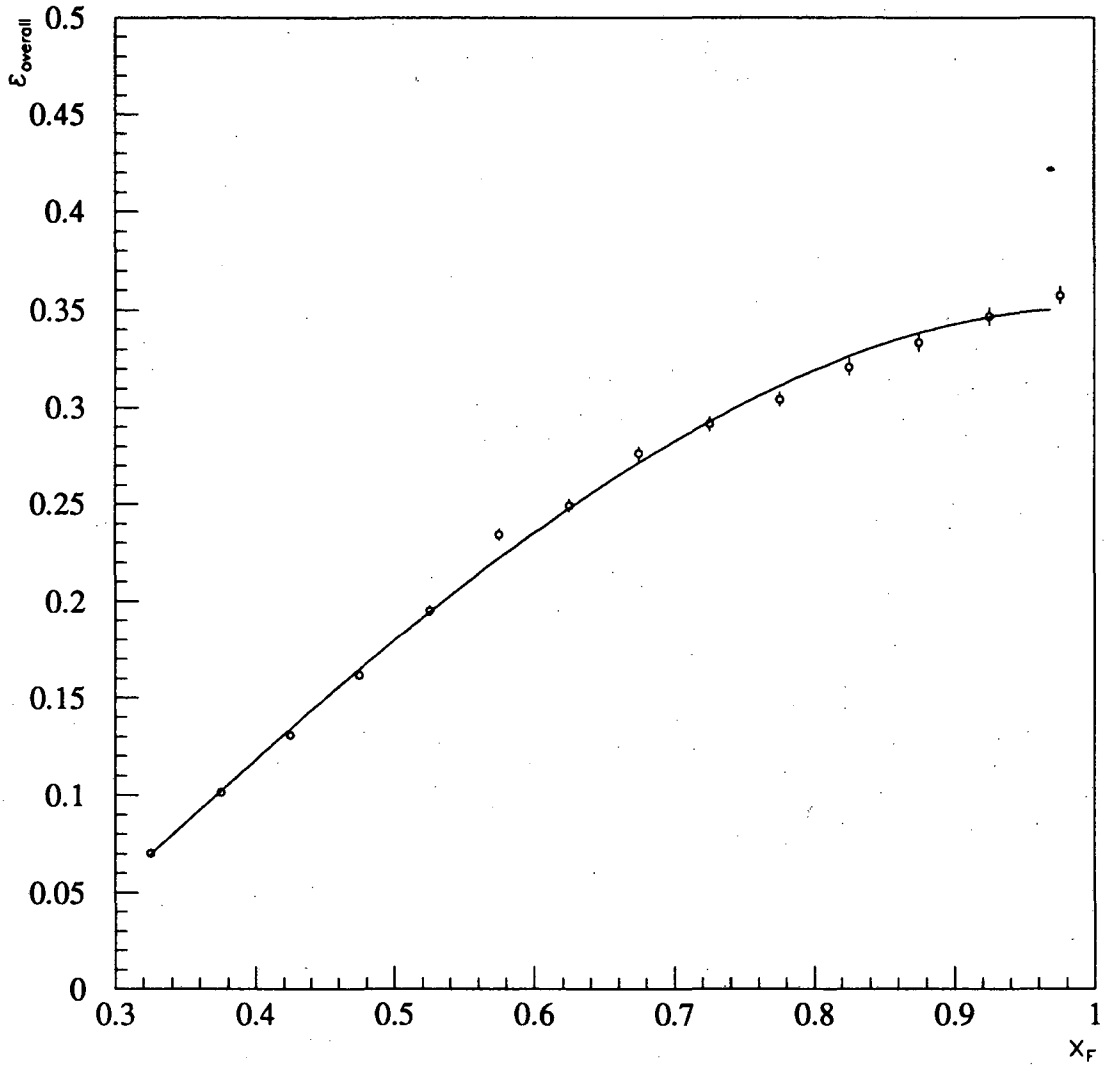

Figure 3.18: Overall acceptance for copper dump run. Points were determined by Monte Carlo using equation (3.19), with 10^4 triggered events simulated for each point. The smooth curve is the result of a fit to a third-order polynomial.

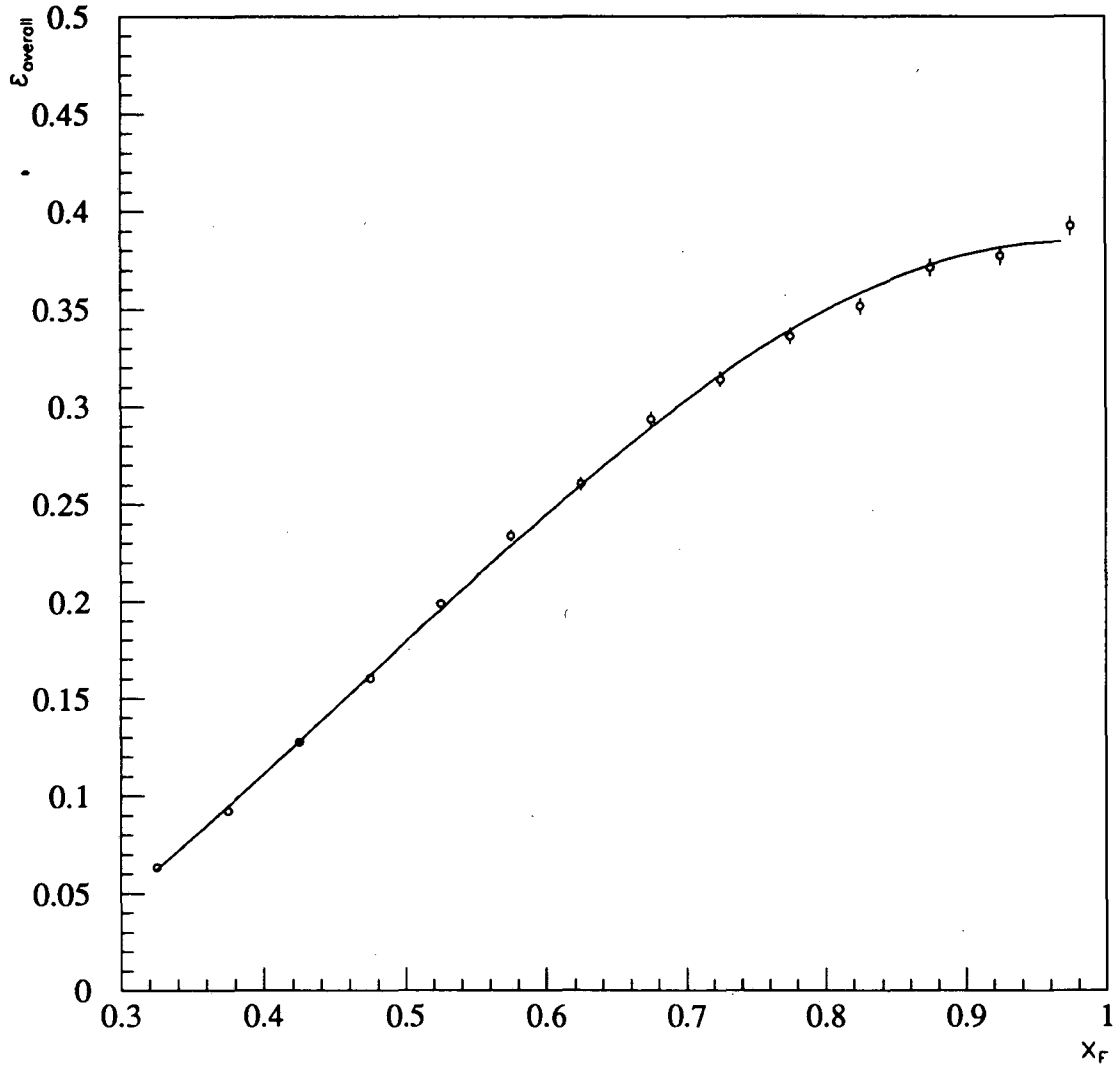

Figure 3.19: Overall acceptance for beryllium dump run. Points were determined by Monte Carlo using equation (3.19), with 10^4 triggered events simulated for each point. The smooth curve is the result of a fit to a third-order polynomial.

3.6 Absolute Normalization

The normalized differential cross section $d\sigma/dx_F$ was related to the number of observed J/ψ events by

$$\frac{d\sigma}{dx_F} = \frac{N_{obs}}{\epsilon_{overall}\epsilon_{live}\mathrm{B}\Delta_{x_F}\mathcal{L}}, \tag{3.20}$$

where N_{obs} is the number of $J/\psi \rightarrow \mu^+\mu^-$ events reconstructed in a given x_F bin, $\epsilon_{overall}$ is the overall (acceptance $\times$ trigger $\times$ reconstruction) efficiency determined by the Monte Carlo study, ϵ_{live} is the live time (discussed below), $B = 5.97 \pm 0.25\%$ is the branching ratio for the decay $J/\psi \rightarrow \mu^+\mu^-$ [12], $\Delta x_F = 0.05$ is the bin width in x_F, and $\mathcal{L}$ is the luminosity (also discussed below).

3.6.1 Live Time

To estimate the effect of dead time due to the event readout process, two spill scalers were dedicated to monitoring the number of triggers generated. The first of these scalers counted the total number of TFI triggers generated, N_{TFI}. The second scaler counted $N_{\mathrm{TFI}\bullet\overline{\mathrm{SB}}}$. This was the number of events collected, since the second level trigger, TGO, was inhibited during the event readout by the logic signal System Busy. Thus the trigger live time was determined by the ratio

$$\epsilon_{live} = \frac{N_{\mathrm{TFI}\bullet\overline{\mathrm{SB}}}}{N_{\mathrm{TFI}}}. \tag{3.21}$$

The live time, as shown in Figures 3.20 and 3.21, was anti-correlated with the beam intensity, so that the live time was lower when the beam intensity was higher. Thus, to accurately determine the live luminosity, the mean live time was determined by a weighted average over spills,

$$\epsilon_{live} = \frac{1}{N_{inc}} \sum_{i=1}^{N_{spills}} \epsilon^i_{live} N^i_{inc} \tag{3.22}$$

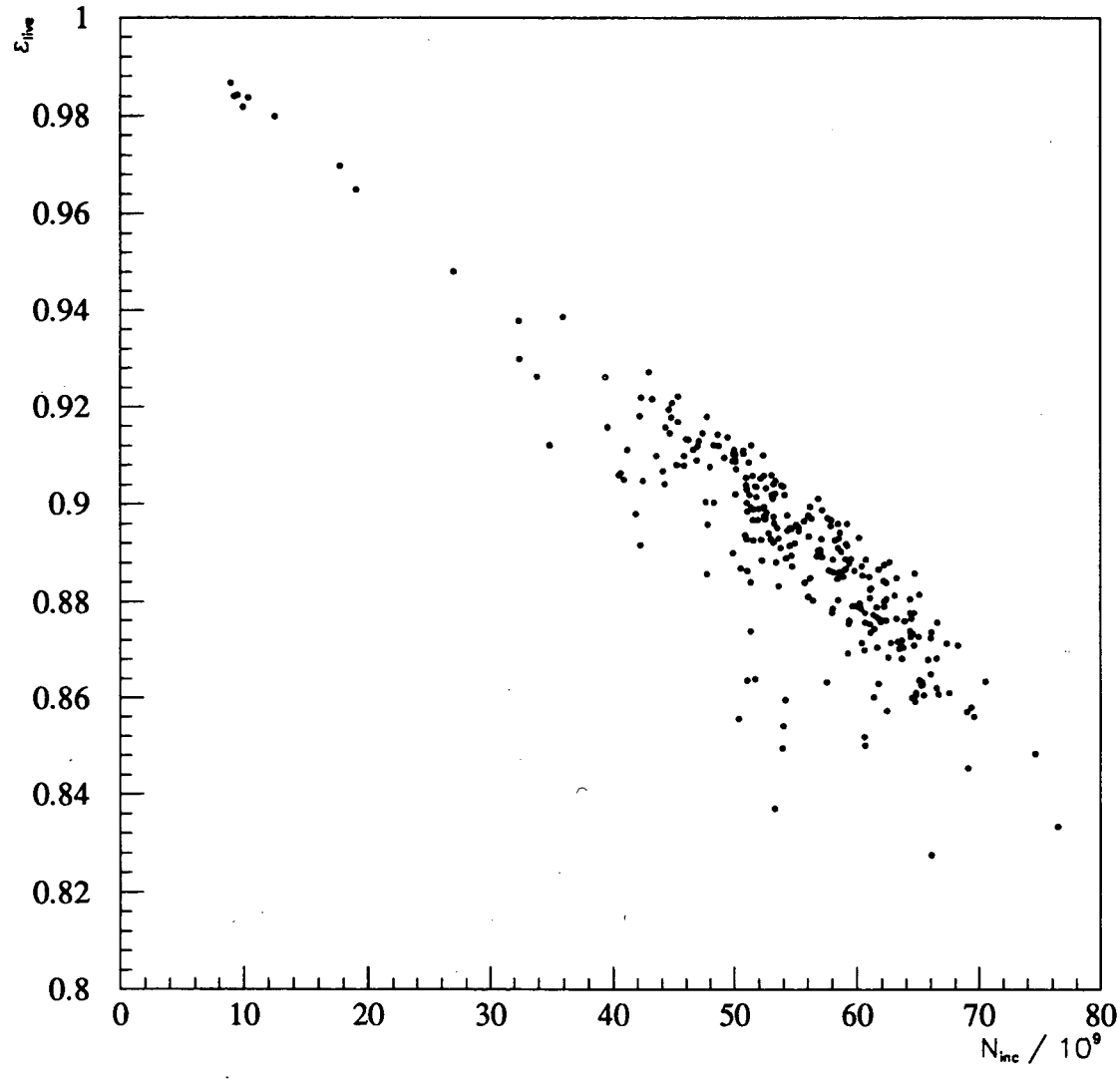

Figure 3.20: Live time for copper dump run. Each point shows the live time ϵ_{live} for a single spill of beam flux N_{inc}. ϵ_{live} was determined from equation (3.21).

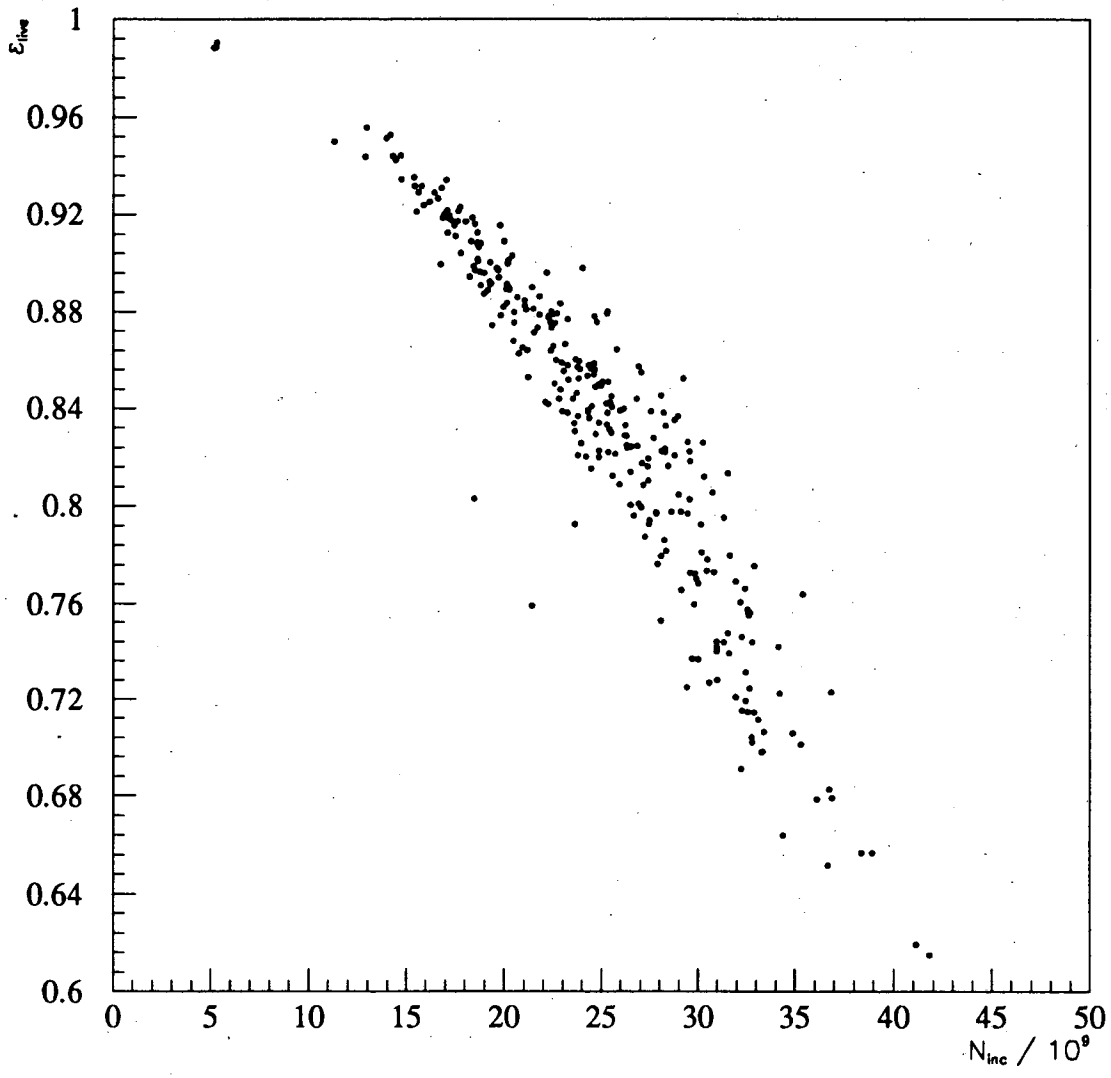

Figure 3.21: Live time for beryllium dump run. Each point shows the live time ϵ_{live} for a single spill of beam flux N_{inc}. ϵ_{live} was determined from equation (3.21).

where ϵ^i_{live} is the live time during spill i as determined by equation (3.21), N^i_{inc} is the incident beam flux during spill i, and N_{inc} is the total incident beam flux during the run.

3.6.2 Luminosity

For a beam dump experiment, the luminosity is related to the total inelastic cross section σ_I,

$$\mathcal{L} = \frac{N_B}{\sigma_I}, \tag{3.23}$$

where N_B is the beam flux interacting in the beam dump. The inelastic cross sections for copper and beryllium were obtained from References 12 and 36, and are shown in Table 3.2. Note that for the beam dump running, the targeting efficiency $\epsilon_{tgt} = 1$.

For the beryllium dump run, a correction must be applied to N_B to account for the finite thickness of the target. Thus,

$$N_B = N_{inc}(1 - f), \tag{3.24}$$

where N_{inc} is the beam flux *incident* on the beryllium target, and $f = \exp(-\Delta Z_{tgt}/\lambda_I)$ is the fraction of the beam flux which *does not* interact in the target (ie, the punch-through fraction). For the beryllium run, $f = 0.106$, whereas for the copper run $f = 0$.

The integrated luminosities for the copper dump and beryllium dump runs are summarized in Table 3.2

3.7 Backgrounds

There are two categories of background processes, namely continuum and resonance, which can produce dimuon events in the mass region of the J/ψ. The continuum

Table 3.2: Integrated Luminosity

	Copper	Beryllium
N_{inc}	1.72×10^{13}	7.65×10^{12}
N_B	1.72×10^{13}	6.84×10^{12}
ϵ_{live}	0.886	0.816
σ_I/A	12.3 mb	22.1 mb
$\int \mathcal{L}dt$	$1.40 \times 10^{6}\text{nb}^{-1}$	$3.10 \times 10^{5}\text{nb}^{-1}$

background contributed a continuous distribution to the dimuon mass spectrum, and could be estimated by interpolation from the side-lobes of the J/ψ mass peak. Resonance backgrounds were J/ψ events produced by secondary hadrons or punch-through beam protons.

3.7.1 Continuum background

There are several processes that contributed to the continuum background of dimuons in the present data. Accidental dimuon pairs were present at the 3–4 percent level, based on the number of like-sign dimuon pairs found during the analysis. Open charm pair production could also contribute to the dimuon continuum through pairs of semi-leptonic decays. Finally, there was also the underlying direct production of dimuon pairs through the Drell-Yan mechanism. In the lower x_F and $m_{\mu\mu}$ bins, semi-leptonic decays of open charm are expected to dominate the continuum, while in the higher x_F and $m_{\mu\mu}$ bins, Drell-Yan is expected to dominate. The continuum was well fitted by a simple exponential, which provided a smooth interpolation of the background near the J/ψ mass from the sidebands of the J/ψ mass peak.

3.7.2 Resonance background

A potentially more troublesome background was secondary production of J/ψ. For the beryllium dump runs, we know that $\sim$10% of the beam flux punched through the beryllium into the copper. These beam protons could then produce J/ψ events, adding a real background to the J/ψ events directly produced in the beryllium. However, this background could be estimated and subtracted from the raw beryllium data, as was described in § 3.4.1. Recall that the punch-through events were reconstructed, on the average, with an invariant mass $\sim$500 MeV below the J/ψ mass, so the subtraction mostly affected the side-lobe of the J/ψ distribution.

Another potential source of resonance background was J/ψ production by secondary pions in the hadronic shower. An estimate of the J/ψ yield due to secondary pions produced in the first four interaction lengths of the copper dump was performed, the result of which can be seen in Figure 3.22. An empirical formula for thick target particle yields was used to estimate the secondary pion flux generated by the primary proton beam [37]. The differential production cross section $d\sigma/dx_F(\pi+N \rightarrow J/\psi+X)$ was taken from Ref. 38, and checked against the results of Ref. 24. As can be seen from the figure, contamination from secondaries is expected to be below 1% in the lowest x_F bin of this study, and drops off rapidly at larger x_F.

3.8 Uncertainties

There are two categories of error associated with the determination of the differential cross section, statistical uncertainty and systematic uncertainty. Statistical errors are totally uncorrelated between the bins, while the systematic errors tend to be

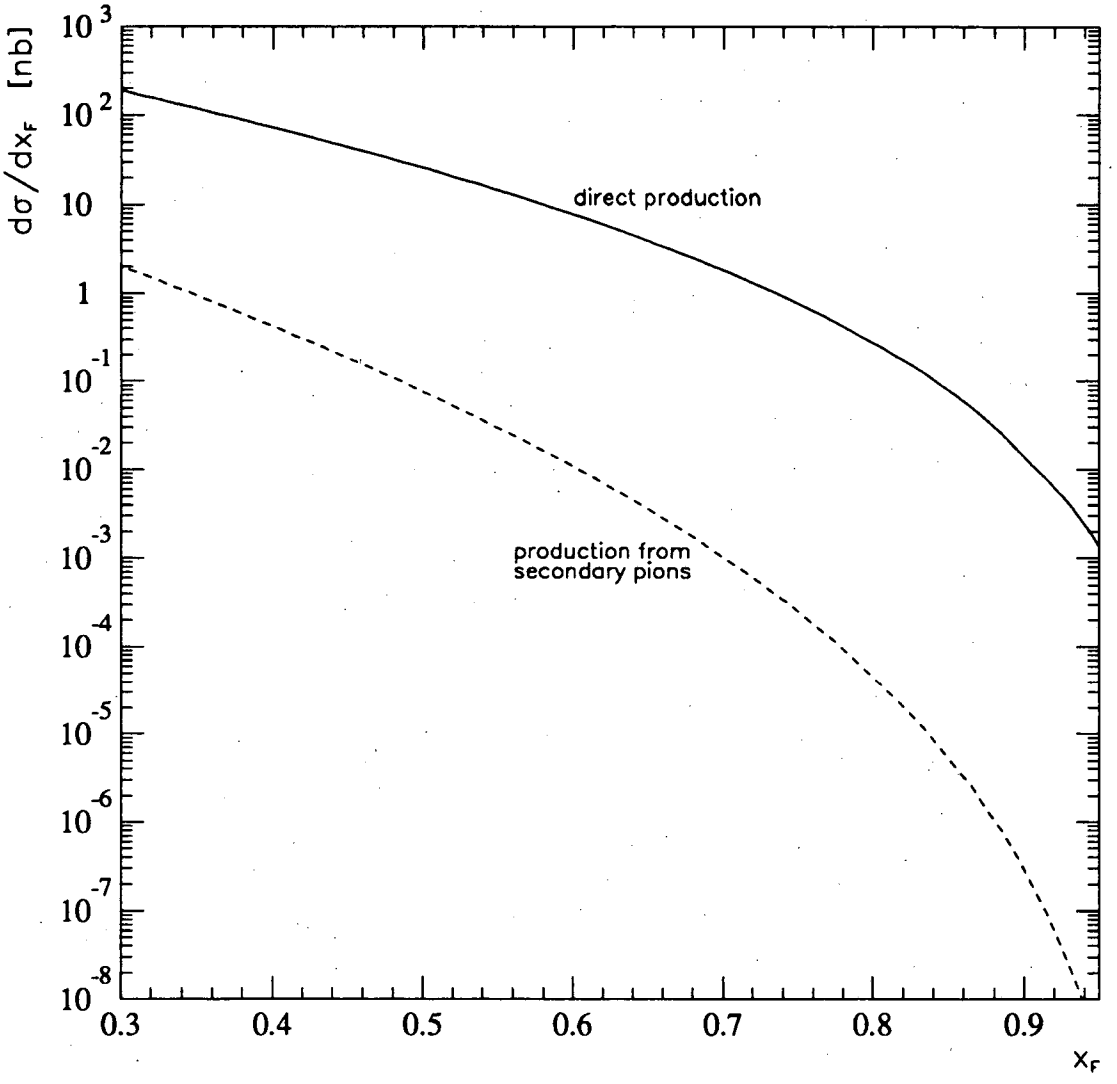

Figure 3.22: Estimation of J/ψ production by secondary pions from the process $p + N \rightarrow \pi + X$; $\pi + N \rightarrow J/\psi + X'$. x_F in this plot is determined with respect to the 800 GeV proton beam momentum, and not with the secondary pion's momentum. The prediction of the semilocal parton duality model for direct production of J/ψ events by beam protons (see Figure 1.4) is also plotted for comparison.

Table 3.3: Fitted number of $J/\psi \rightarrow \mu^+\mu^-$ observed

x_F	N_{fit}(p+Cu $\rightarrow J/\psi \rightarrow \mu^+\mu^-$)	N_{fit}(p+Be $\rightarrow J/\psi \rightarrow \mu^+\mu^-$)
.325	54301 ± 199	11044 ± 90
.375	45656 ± 185	9881 ± 86
.425	34845 ± 169	7973 ± 80
.475	25057 ± 147	6034 ± 71
.525	16705 ± 124	4060 ± 62
.575	10462 ± 97	2728 ± 51
.625	6076 ± 82	1638 ± 44
.675	3413 ± 71	833 ± 36
.725	1454 ± 50	474 ± 23
.775	648 ± 39	164 ± 16
.825	228 ± 17	93 ± 22
.875	61 ± 11	35 ± 7
.925	14 ± 4	

highly correlated between bins. These different sources of errors are discussed below, and summarized in tabular form.

3.8.1 Statistical Uncertainty

When performing the maximum likelihood fits described in § 3.4, an estimate of the error in the fit parameters is obtained by finding the contour in the fit-parameter space that decreases the logarithm of the likelihood function by 1/2. The statistical weight of each bin in the mass histogram, however, is what determines the likelihood function. Thus, the estimated error in N_{fit} from the likelihood method is the appropriate measure of the statistical uncertainty in the number of J/ψ events counted in the bin. Table 3.3 lists the fitted values for N_{fit} along with the statistical uncertainties determined by the maximum likelihood method, for both the copper and the beryllium data sets.

3.8.2 Systematic Uncertainty in the Differential Cross Section

The systematic uncertainties fall into two categories, the uncertainty in the luminosity, branching ratio, and live time, and the uncertainty in the overall efficiency, $\epsilon_{overall}$. The first category only affects the overall normalization of the data, while the second category can result in bin-dependent uncertainties.

The absolute normalization uncertainty is dominated by the calibration error in the beam monitor, ME3IC. This was estimated to be $\pm 10\%$. The next largest contribution comes from the uncertainty in the branching ratio for $J/\psi \rightarrow \mu^+\mu^-$ ($\pm 4\%$), followed by the uncertainty in the inelastic cross section ($\pm 3\%$). Note that uncertainty due to the inelastic cross section is slightly larger for the beryllium data set, since it affects the punch through subtraction as well as the normalization. The determination of the live time by the method of § 3.6.1 should not introduce more than $\pm 1\%$ additional uncertainty in the absolute normalization. These uncertainties are summarized in Table 3.4.

To understand the uncertainties in $\epsilon_{overall}$, a series of Monte Carlo studies were performed in which different parameters were varied to determine their impact on $\epsilon_{overall}$. Table 3.5 lists the results of these studies, which are discussed below.

Table 3.4: Systematic Uncertainties in the Normalization

	Copper	Beryllium
Beam Intensity	10%	10%
Branching Ratio	4%	4%
σ_I	3%	4%
ϵ_{live}	1%	1%
Total Uncertainty	11%	12%

The largest error came from the estimated $\pm 1\%$ uncertainty in the absolute normalization of the SM12 field map. The SM3 field map normalization, although uncertain to $\pm 1\%$, had a much smaller impact on the acceptance.

As was discussed in §3.5.1, the Monte Carlo $p_\perp$ distributions reproduced the observed $p_\perp$ distributions well, with an rms in the fitted p_0 of 4.3%. The uncertainty in $\epsilon_{overall}$ due to the Monte Carlo $p_\perp$ generation was therefore studied by varying the scale factor p_0 in equation (3.18) by $\pm 5\%$. This systematic uncertainty was similar in magnitude to that introduced by the SM12 field map uncertainty.

There was moderate uncertainty in $\epsilon_{overall}$ due to the J/ψ decay distribution. If the μ^+ angular distribution in the J/ψ rest frame is given by

$$d\sigma \propto (1 + \lambda \cos^2 \theta^*) d\cos\theta^* \tag{3.25}$$

where θ^* is the angle between the μ^+ and the J/ψ momentum direction (the helicity axis), then λ parameterizes the J/ψ polarization. $\lambda = 0$ corresponds to uniform, isotroptic decay. In Ref. 35, Siskind *et al.* reported a value of 0.16 ± 0.08 for λ with J/ψ's produced by 400 GeV protons. Their sample had about 11% contamination due to the Drell-Yan continuum, which has $\lambda = 1$ in the angular distribution [39]. The measured value of λ would imply a uniform decay for the J/ψ. The Monte Carlo events were therefore generated with the assumption of $\lambda = 0$. To determine the systematic uncertainty in $\epsilon_{overall}$ due to this assumption, λ was varied to ± 0.1.

3.8.3 Systematic Uncertainty in the Nuclear Dependence

Many of the systematic errors in the differential cross section cancel in the ratio of copper to beryllium production. This was true for the field map uncertainties as well as the uncertainty due to the branching ratio, $p_\perp$ and $\cos\theta^*$ generation. Even with minor calibration drifts taken into account, the calibration uncertainty in the beam

Table 3.5: Systematic Uncertainties in $\epsilon_{overall}$

	$\Delta\epsilon/\epsilon$ in %				
x_F	SM12	SM3	$p_\perp$	decay	Total
.325	4.7	2.3	3.4	2.9	6.9
.375	3.1	1.4	2.7	2.9	5.2
.425	2.0	1.0	2.3	2.9	4.3
.475	1.7	1.0	2.1	2.9	4.1
.525	1.7	0.9	1.8	2.8	3.8
.575	1.7	0.9	1.5	2.7	3.6
.625	1.6	0.7	1.3	2.6	3.4
.675	1.5	0.6	1.2	2.4	3.1
.725	1.5	0.5	1.1	2.0	2.8
.775	1.4	0.5	1.0	1.8	2.5
.825	1.1	0.5	1.0	1.8	2.4
.875	0.9	0.5	1.0	1.8	2.3
.925	0.8	0.5	1.0	1.7	2.2

flux monitor ME3IC will largely cancel from the ratio. There is no cancelation in the error from the inelastic cross section. Furthermore, the uncertainty in the inelastic cross section of p+Be leads to an additional uncertainty due to the beam punch-through correction. Thus, there is an estimated overall systematic uncertainty of 5% in the differential cross section ratio. This is equivalent to a constant systematic uncertainty in α of ± 0.025.

CHAPTER 4

RESULTS

The differential cross sections $d\sigma/dx_F$ and A-dependence have been measured for the processes p+Cu $\rightarrow J/\psi + X$ and p+Be $\rightarrow J/\psi + X$. In this chapter the results of the measurements are presented, along with comparisons to the theoretical models discussed in Chapter 1.

4.1 DIFFERENTIAL CROSS SECTION

The differential cross sections $d\sigma/dx_F$ for J/ψ production in p+Cu and p+Be collisions at 800 GeV are presented in Table 4.1, and plotted in Figures 4.1 and 4.2. In the figures, only the statistical uncertainties are shown.

4.1.1 FIT TO $(1 - x_F)^n$

The shape of the differential cross section is often quoted in terms of the exponent n for the distribution $d\sigma/dx_F \propto (1 - x_F)^n$. Figure 4.3 shows this fit for the copper dump data. Since the data are not well described by a single exponent n, several regions have been separately fitted in the figure. If the lowest two points in x_F are excluded from the fit, as in Figure 4.3 (b), the exponent is fitted as $n = 5.46 \pm 0.02$, but with a very poor $\chi^2/\text{NDF} = 20$. This result changes very little if we restrict the

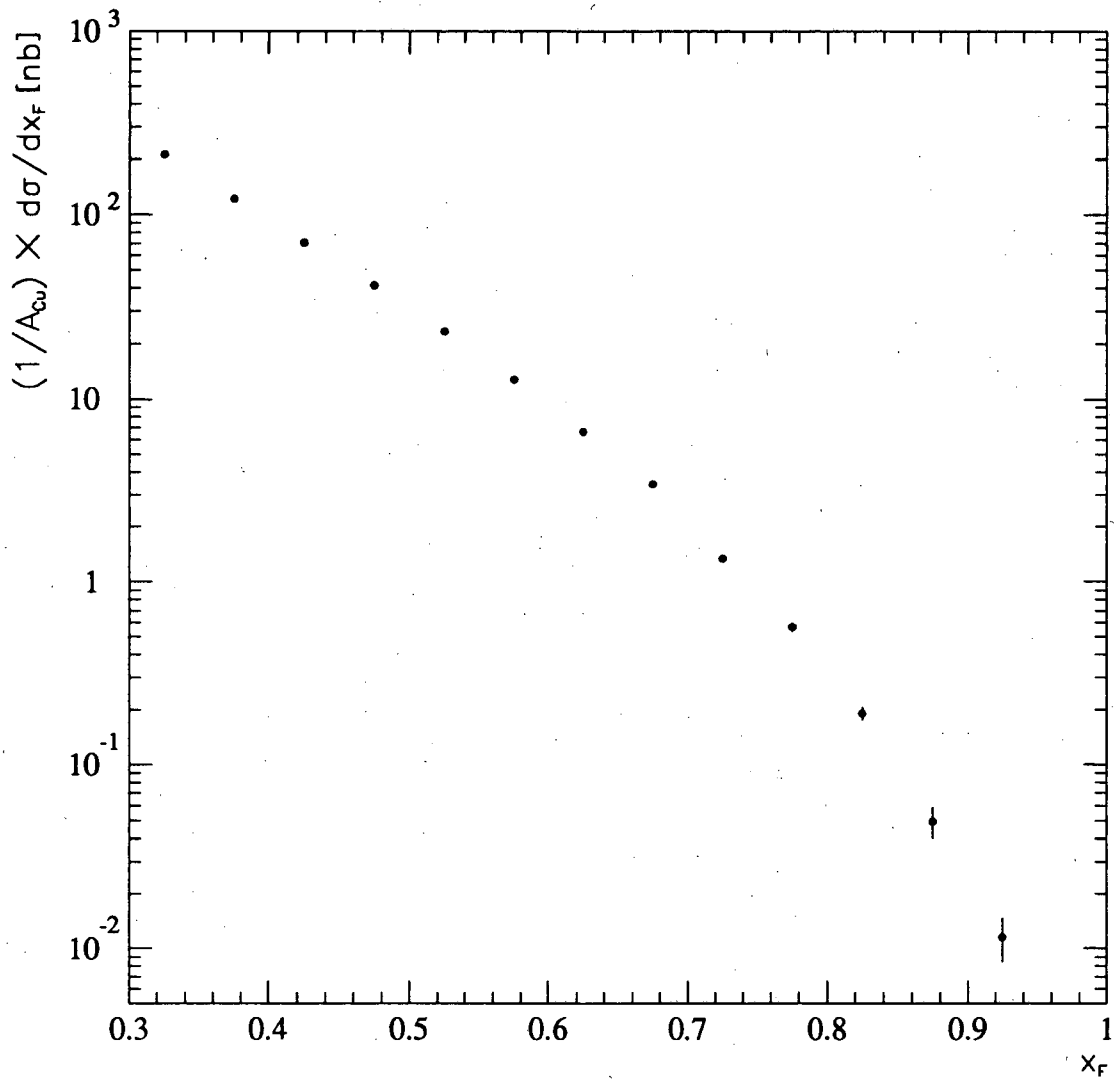

Figure 4.1: Differential cross section for p+Cu $\rightarrow J/\psi + X$. Note that only statistical errors are shown.

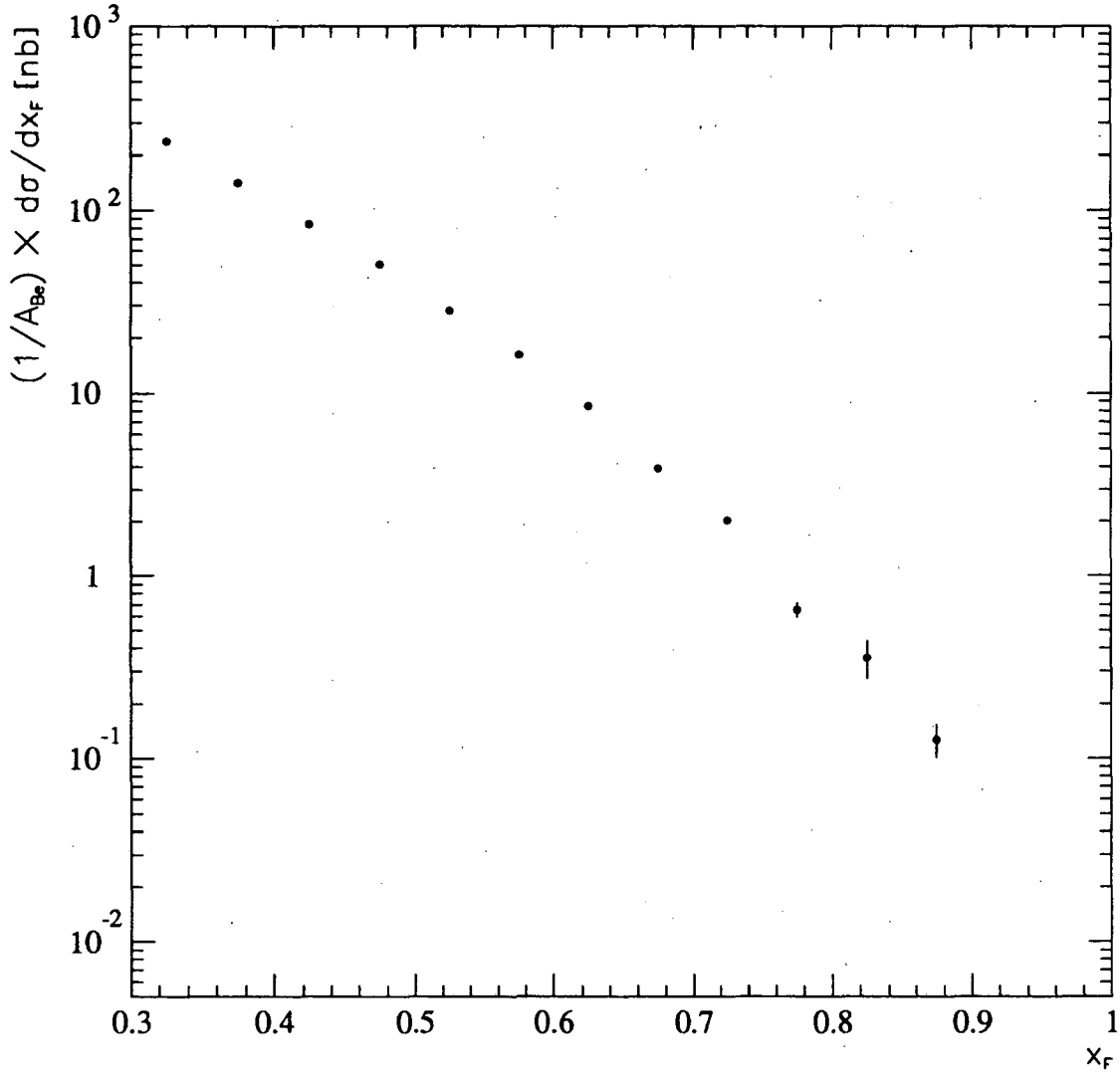

Figure 4.2: Differential cross section for p+Be $\rightarrow J/\psi + X$. Note that only statistical errors are shown.

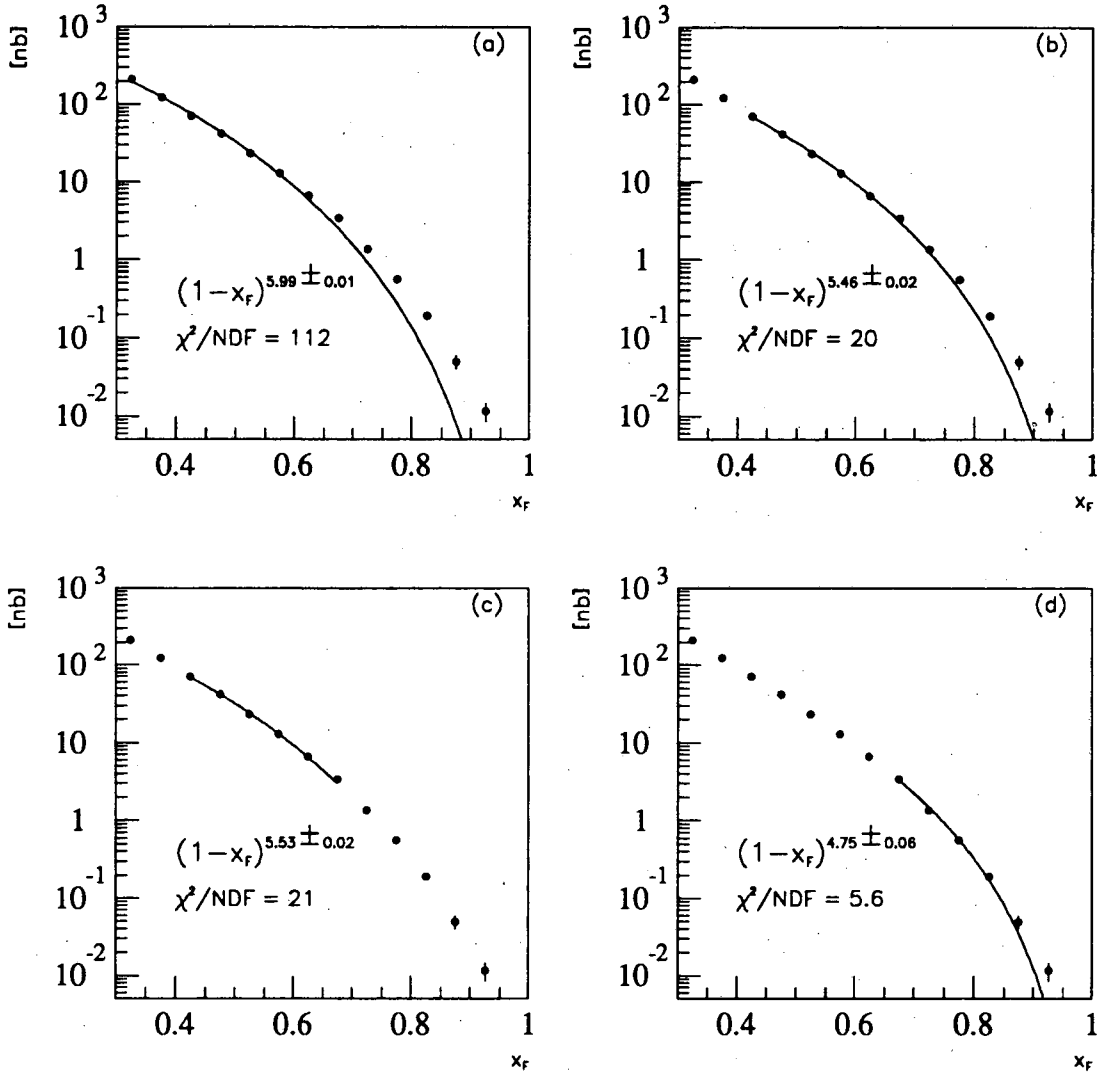

Figure 4.3: Fits to $(1 - x_F)^n$ for p+Cu data. (a) shows the fit to the entire range in x_F, (b) excludes the first two points, (c) is fit to the range $0.40 < x_F < 0.70$, and (d) is fit for $x_F > 0.65$.

Table 4.1: Differential Cross Sections (nb/nucleon)

	p+Cu$\rightarrow J/\psi + X$	p+Be$\rightarrow J/\psi + X$
x_F	$(1/A)d\sigma/dx_F \pm$ (stat) $\pm$ (sys)	$(1/A)d\sigma/dx_F \pm$ (stat) $\pm$ (sys)
.325	211.39 $\pm$ .78 $\pm$ 15.	238.4 $\pm$ 1.9 $\pm$ 16.
.375	121.20 $\pm$ .49 $\pm$ 6.3	140.8 $\pm$ 1.2 $\pm$ 7.4
.425	70.55 $\pm$ .34 $\pm$ 3.0	84.07 $\pm$ .85 $\pm$ 3.6
.475	41.26 $\pm$ .24 $\pm$ 1.7	50.32 $\pm$ .60 $\pm$ 2.1
.525	23.33 $\pm$ .17 $\pm$ .90	28.03 $\pm$ .43 $\pm$ 1.1
.575	12.78 $\pm$ .12 $\pm$ .47	16.12 $\pm$ .30 $\pm$ .59
.625	6.65 $\pm$ .09 $\pm$ .23	8.51 $\pm$ .23 $\pm$ .29
.675	3.41 $\pm$ .07 $\pm$ .11	3.89 $\pm$ .17 $\pm$ .12
.725	1.35 $\pm$ .05 $\pm$ .04	2.03 $\pm$ .10 $\pm$ .06
.775	.565 $\pm$ .034 $\pm$ .014	.653 $\pm$ .064 $\pm$ .017
.825	.190 $\pm$ .015 $\pm$ .004	.354 $\pm$ .083 $\pm$ .008
.875	.0493 $\pm$ .0095 $\pm$ .0011	.127 $\pm$ .026 $\pm$ .003
.925	.0116 $\pm$ .0031 $\pm$ .0003	

fit to the region $0.4 < x_F < 0.7$. If only points at $x_F > 0.65$ are fitted, then the fit improves to give $n = 4.75 \pm 0.06$ with $\chi^2/\text{NDF} = 5.6$.

4.1.2 Comparison with Semilocal Parton Duality

The semilocal parton duality model is quite successful in describing the data across four decades in cross section. Figures 4.4 and 4.5 shows the result of fitting the copper dump data, and the beryllium dump data, to the model prediction with $m_c = 1.5$ GeV and target parton shadowing, in the range $0.40 < x_F < 0.95$. The lowest two points in x_F were excluded from the fit due to the larger uncertainty in acceptance there. There is only one free parameter in this fit, which is the overall normalization factor F in equation (1.8).

The fit to the copper dump data yielded $F = 1/(6.07 \pm 0.02)$ with a $\chi^2/\text{NDF} = 4.0$ based on the statistical errors only, while the fit to the beryllium dump data gave $F = 1/(5.73 \pm 0.04)$ with a $\chi^2/\text{NDF} = 2.2$. Comparing the copper and beryllium

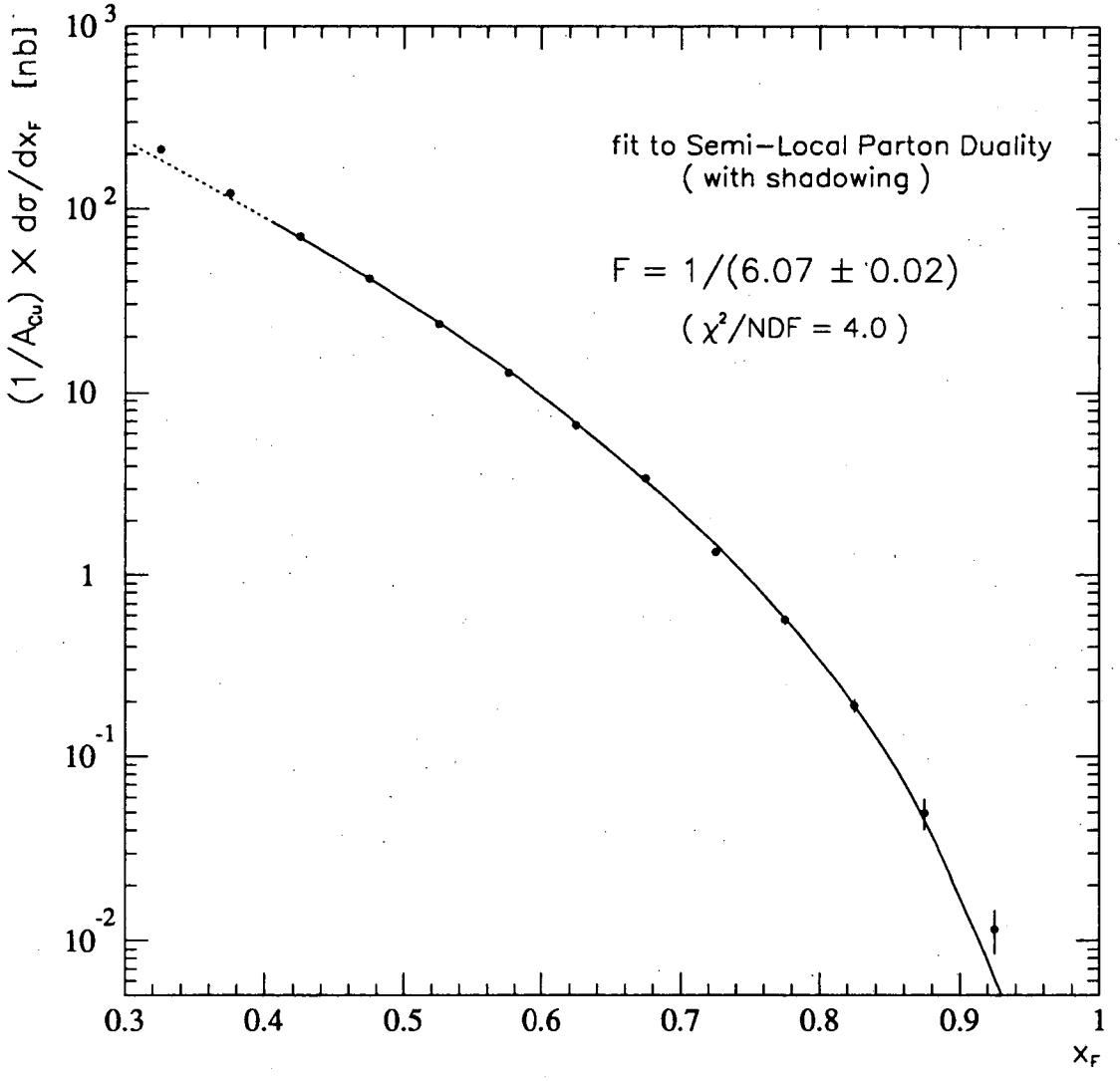

Figure 4.4: Fit of the semilocal parton duality model to the differential cross section for p+Cu $\rightarrow J/\psi$. The points at $x_F < 0.40$ were excluded from the fit.

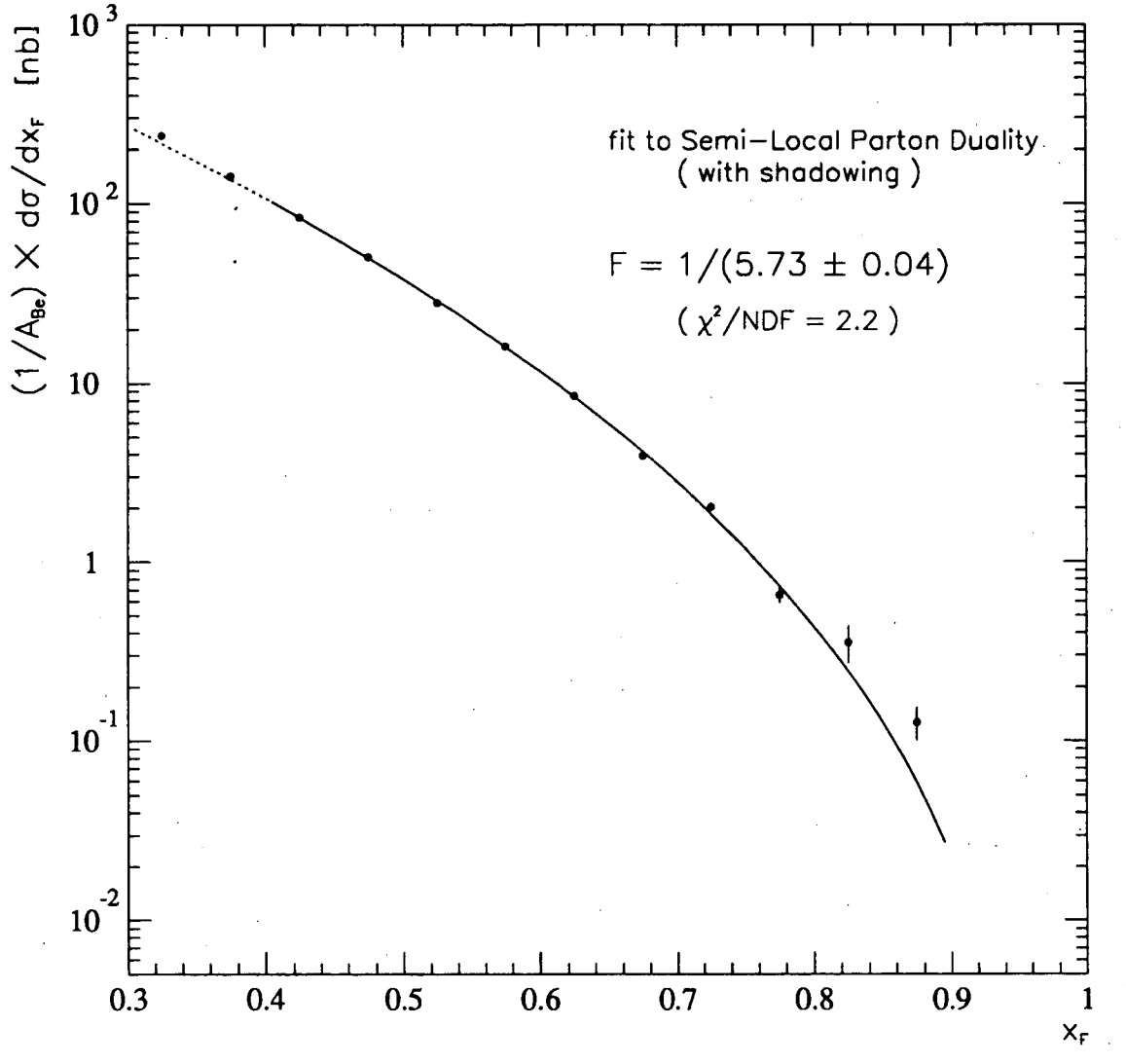

Figure 4.5: Fit of the semilocal parton duality model to the differential cross section for p+Be $\rightarrow J/\psi$. The points at $x_F < 0.40$ were excluded from the fit.

data, we have

$$\frac{F(\mathrm{p}+\mathrm{Cu})}{F(\mathrm{p}+\mathrm{Be})} = 0.94 \pm 0.01 \pm 0.05 \tag{4.1}$$

where the second error is the systematic uncertainty in the relative normalization between the copper and beryllium data sets. This ratio is consistent with unity. In addition, by including the overall normalization uncertainty of 11% (12%) in the copper (beryllium) data, we obtain $F = 1/(6.1 \pm 0.7)$ in copper, and $F = 1/(5.7 \pm 0.7)$ in beryllium. The last point in the copper dump data, at $x_F = 0.925$, lies 2.4 standard deviations above the fitted curve. The last point in the beryllium dump data also lies above the fitted curve, by 2.6 standard deviations.

4.1.3 Comparison with Intrinsic Charm

The data show no evidence for any intrinsic charm contribution in the differential cross sections. To quantify this statement, a two-component fit to the data was performed to determine the magnitude of a possible intrinsic charm admixture. The differential cross sections from the copper dump and beryllium dump runs were fitted to a function of the form

$$\frac{d\sigma}{dx_F} = F\frac{d\sigma_0}{dx_F} + C\frac{d\sigma_{ic}}{dx_F} \tag{4.2}$$

where $d\sigma_0/dx_F$ is the semilocal parton duality prediction, given by equation (1.8), $d\sigma_{ic}/dx_F$ is the intrinsic charm contribution, shown in Figure 1.6, and F and C are free parameters of the fit. The parameters F and C were bounded from below by zero. The fits found $F = 1/(6.07 \pm 0.02)$ and $C = (0.^{+2.4}_{-0.}) \times 10^{-3}$ with $\chi^2/\mathrm{NDF} = 4.5$ for the copper dump data, and $F = 1/(5.75 \pm 0.04)$ and $C = (1.0^{+1.4}_{-1.0}) \times 10^{-2}$ with $\chi^2/\mathrm{NDF} = 2.4$ for the beryllium dump data. These imply 95% confidence level upper limits on the total intrinsic charm contribution to the forward J/ψ production cross

section,

$$\sigma_{IC}(\mathrm{p} + \mathrm{Cu} \rightarrow J/\psi + X) < 8.6 \times 10^{-3}\,\mathrm{nb/nucleon} \tag{4.3}$$

$$\sigma_{IC}(\mathrm{p} + \mathrm{Be} \rightarrow J/\psi + X) < 8.8 \times 10^{-2}\,\mathrm{nb/nucleon.} \tag{4.4}$$

Comparing these limits to the values in equations (1.19) and (1.20), we see that any intrinsic charm contribution to J/ψ production must be less than 0.5% of the originally predicted level in copper, and less than 3% of the originally predicted level in beryllium.

4.2 Nuclear Dependence

The A-dependence of J/ψ production by 800 GeV protons has been measured at large x_F in p+Cu and p+Be collisions. From the values shown in Table 4.1, we define the production ratio for J/ψ as

$$R = \frac{(1/A_{Cu})d\sigma/dx_F(\mathrm{p} + \mathrm{Cu} \rightarrow J/\psi)}{(1/A_{Be})d\sigma/dx_F(\mathrm{p} + \mathrm{Be} \rightarrow J/\psi)}. \tag{4.5}$$

From R, we can determine the exponent α from equation (1.10) as

$$\alpha = 1 + \frac{\ln R}{\ln(A_{\mathrm{Cu}}/A_{\mathrm{Be}})}. \tag{4.6}$$

Table 4.2 lists the A-dependence relative to x_F, both in terms of R and α. See also Figures 4.6 and 4.7. Only statistical errors are shown. There is an overall systematic uncertainty in R of $\pm 5\%$. This is equivalent to a constant systematic uncertainty in α of ± 0.025.

4.2.1 Comparison with E772 and Theory

Figure 4.8 is a comparison of the predictions of the parton shadowing model and the intrinsic charm model with the data. The results of E772 are also shown. Within

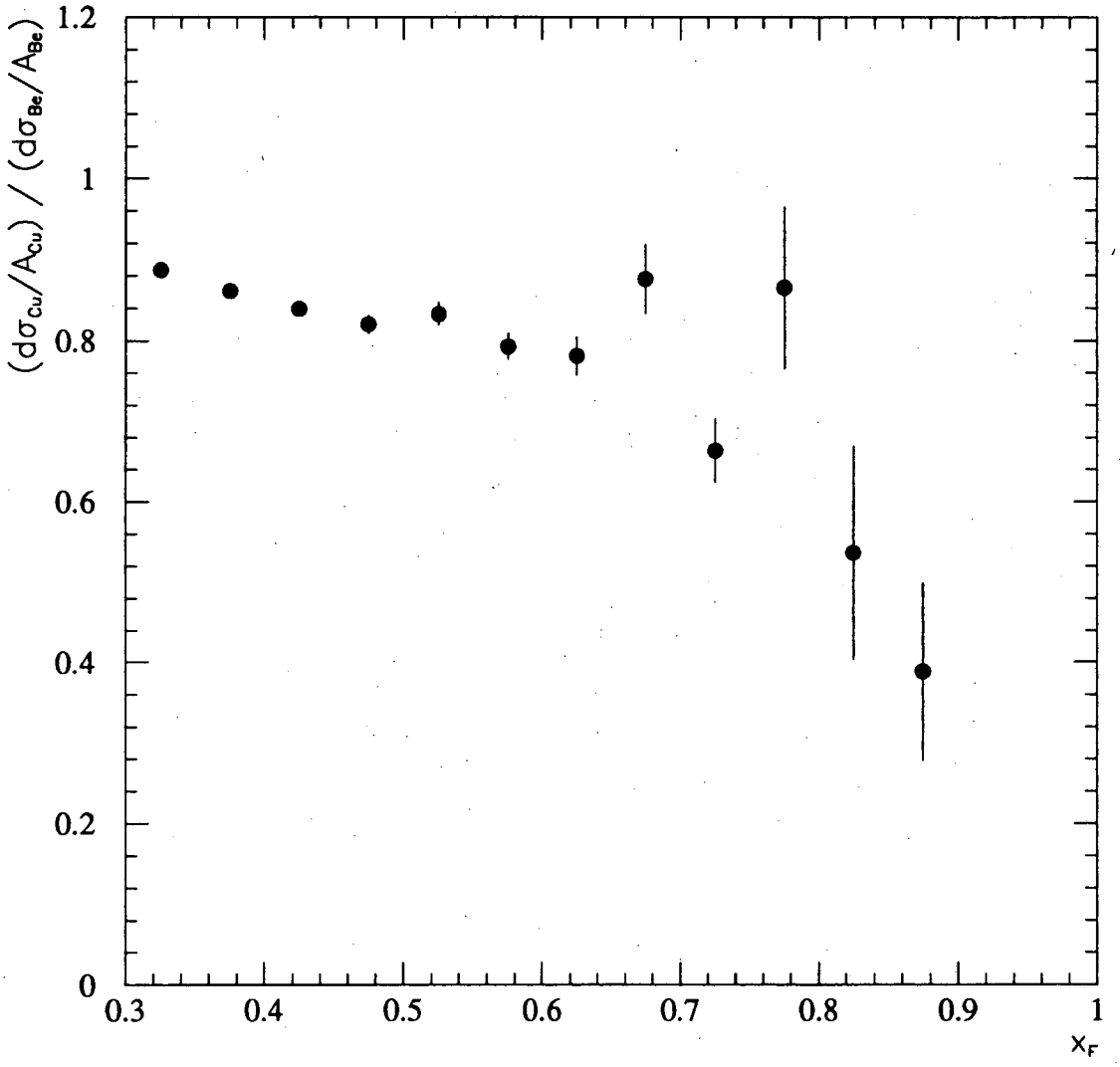

Figure 4.6: Ratio of the differential cross sections for J/ψ production in 800 GeV p+Cu and p+Be collisions. Only statistical errors are shown. The systematic uncertainty in the ratio is 5%.

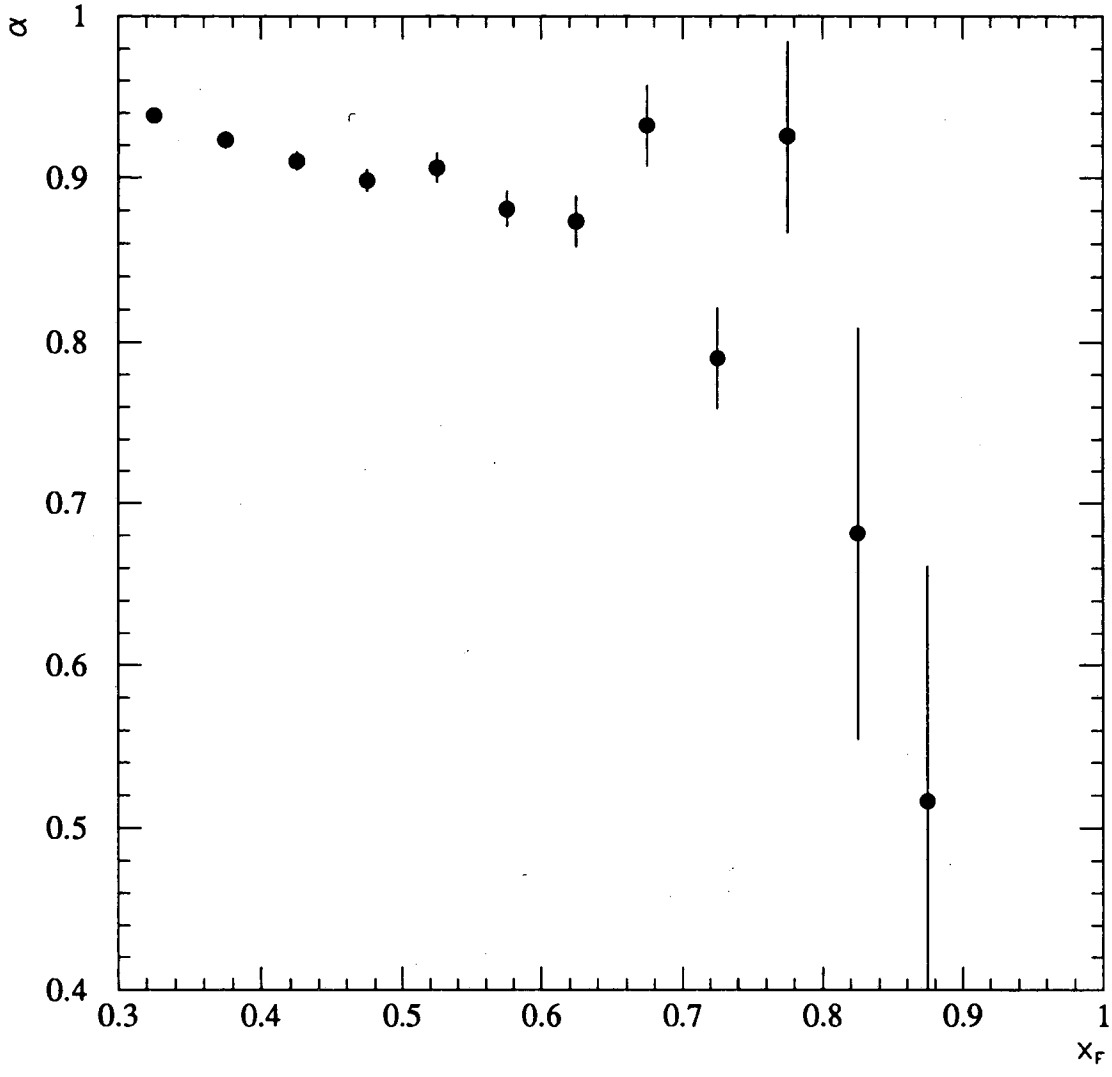

Figure 4.7: Nuclear dependence of J/ψ production in terms of the exponent α, where $d\sigma_A/dx_F \sim A^\alpha$. Only statistical errors are shown. The systematic uncertainty in α is ± 0.025.

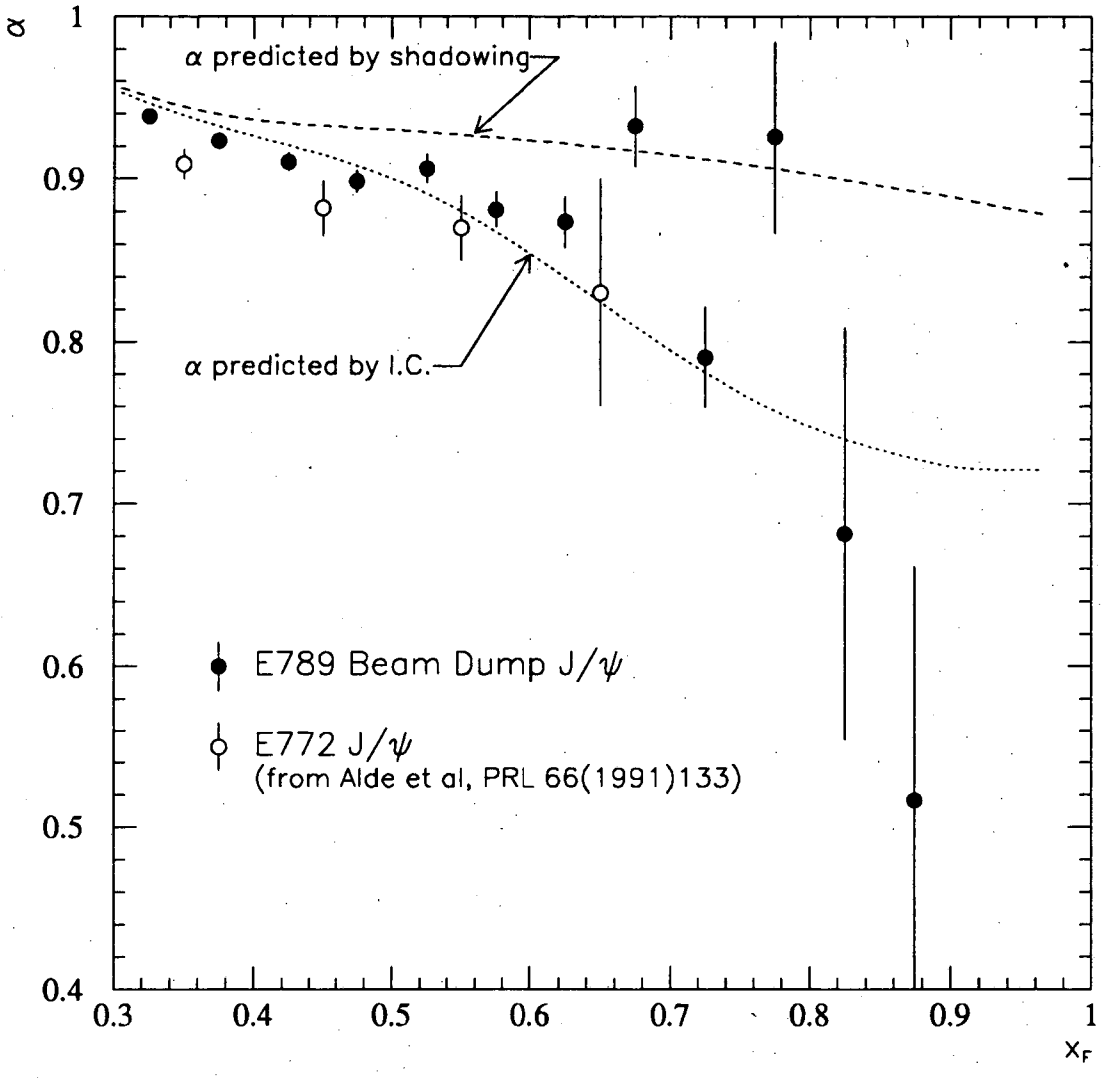

Figure 4.8: Comparison of theories with data for the A-dependence of J/ψ production. The solid points are the present study, while the hollow points are from E772. Only statistical errors are shown. The dashed curve shows the prediction of the semilocal parton duality model including the effect of target parton shadowing, from Figure 1.5. The dotted curve shows the prediction of the intrinsic charm model, from Figure 1.9. The systematic uncertainty in α for this study is ± 0.025, while for the E772 points it is ± 0.008.

Table 4.2: A–dependence. Only statistical errors are listed.

x_F	R	α
.325	.887 ± .008	.938 ± .005
.375	.861 ± .008	.923 ± .005
.425	.839 ± .009	.910 ± .006
.475	.820 ± .011	.898 ± .007
.525	.833 ± .014	.906 ± .009
.575	.793 ± .017	.881 ± .011
.625	.781 ± .024	.873 ± .016
.675	.876 ± .043	.932 ± .025
.725	.664 ± .040	.790 ± .031
.775	.865 ± .099	.926 ± .059
.825	.537 ± .133	.682 ± .127
.875	.389 ± .110	.516 ± .145

the systematic uncertainty of the current measurement, the nuclear dependence observed for J/ψ production is marginally consistent with the E772 results. It should be pointed out again that the current measurement used only copper and beryllium targets, while E772 used tungsten, iron, calcium, carbon, and liquid deuterium targets to extract the A–dependence. The different $p_\perp$ acceptances of the two experiments could also affect the comparison. The parton shadowing model roughly resembles the behaviour of the data at relatively low and moderate x_F, but cannot reproduce the degree of suppression seen in the data when $x_F > 0.7$. The intrinsic charm model, with its contribution to the cross section scaling like $A^{.71}$ and dominating at high x_F, can explain the data well. However, this agreement should be viewed in light of the fact that the intrinsic charm model was tuned to the experimental data for nuclear suppression from NA3 and E772. Furthermore, this model is ruled out based on the shape of the differential cross section (see §4.1.3). To summarize, there is no satisfactory theoretical framework that explains the observed A–dependence in J/ψ production at moderate to large x_F.

CHAPTER 5

CONCLUSIONS AND FUTURE PROSPECTS

The differential cross section $d\sigma/dx_F$ of J/ψ production by 800 GeV protons in collision with copper and beryllium has been measured from $0.30 < x_F < 0.95$, and $0 < p_\perp < 5$ GeV. The differential cross sections in copper and beryllium were in good agreement with the predictions of the semilocal parton duality model using the MRS set S_0 parton distribution functions, modified to account for parton shadowing in the nuclear target. This model predicts that gluon-gluon fusion dominates the production cross-section at $x_F < 0.7$, while quark-antiquark annihilation dominates at $x_F > 0.7$ (see Figure 1.4). The data were found to agree with the model across both of these kinematic regions. The intrinsic charm model of J/ψ production was strongly contradicted by the data.

The nuclear dependence of J/ψ production was measured over the range $0.3 < x_F < 0.9$, with $p_\perp$ integrated over the range from 0 GeV to 5 GeV. Within the systematic uncertainties of this measurement, the results were marginally in agreement with the previously published results from E772. The discrepancy could be due to the different target materials and $p_\perp$ range covered in the two experiments. The results were marginally explained by the target parton shadowing model.

Quarkonium production is a relatively mature field. However, there remain several persistent mysteries —

- The nuclear dependence is not understood.
- The details of the hadronization process (buried in F) are not understood.
- Some evidence exists for the polarization of J/ψ in π+N$\rightarrow J/\psi + X$ at $x_F > 0.95$ (see §1.3.2).

The days of fixed-target high energy physics experiments are waning, but there may yet be opportunities to further study heavy quarks near the limits of phase space.

A new dedicated experiment using 800 GeV protons should be able to collect several hundred times more data than was collected for this study in a single fixed-target running period. Such an experiment would use a low–Z material for the hadron absorber, say beryllium or carbon, instead of copper. This would significantly reduce the amount of multiple scattering the muons would suffer, thus improving the mass resolution. A good range of target materials could be employed to better measure the A–dependence and to test the A^α assumption at large x_F. This experiment could accumulate sufficient statistics at very large x_F to be able to search for polarization effects, as has been seen in the reaction $\pi + N \rightarrow J/\psi + X$, or other evidence for QCD higher-twist contributions to charmonium production.

More interestingly, such an experiment could have some sensitivity to high x_F production of Υ. Figure 5.1 shows the semilocal parton model prediction for 800 GeV p+N $\rightarrow J/\psi + X$ together with a similar calculation for p+N $\rightarrow \Upsilon + X$. The F factor used for the Υ calculation was taken to be $F = 1/28.5$, consistent with the measured production cross section for 800 GeV p+N $\rightarrow \Upsilon + X$ at $x_F = 0$ [31]. $m_b =$ 4.7 GeV was assumed for the bottom quark mass. If an experiment could be built with substantially better mass resolution at high x_F than the present study, it may

be possible with several hundred-fold greater luminosity to observe Υ production out to x_F of 0.7 or 0.8. This is an entirely unexplored region of phase space for beauty.

Even more intriguing is the possibility of a fixed-target program at the Superconducting Super Collider Laboratory (SSCL). It would be experimentally challenging to study large x_F quarkonium from direct production with the primary 20 TeV proton beam, since the decay muons from such events would be in the multi-TeV energy range where radiative effects would dominate. The conventional approach of identifying muons with shielding would not be practical. However, a fully supported fixed-target program at SSCL could provide experimental facilities such as 1 TeV pion beam lines. This would be an ideal setting for studying high x_F heavy quark production. Figure 5.2 shows the semilocal parton duality predictions for 1 TeV π+N inclusive production of J/ψ and Υ. The much harder parton distribution functions of the pion would give several orders of magnitude enhancement in the production cross section of quarkonium at large x_F, relative to that obtained from the proton.

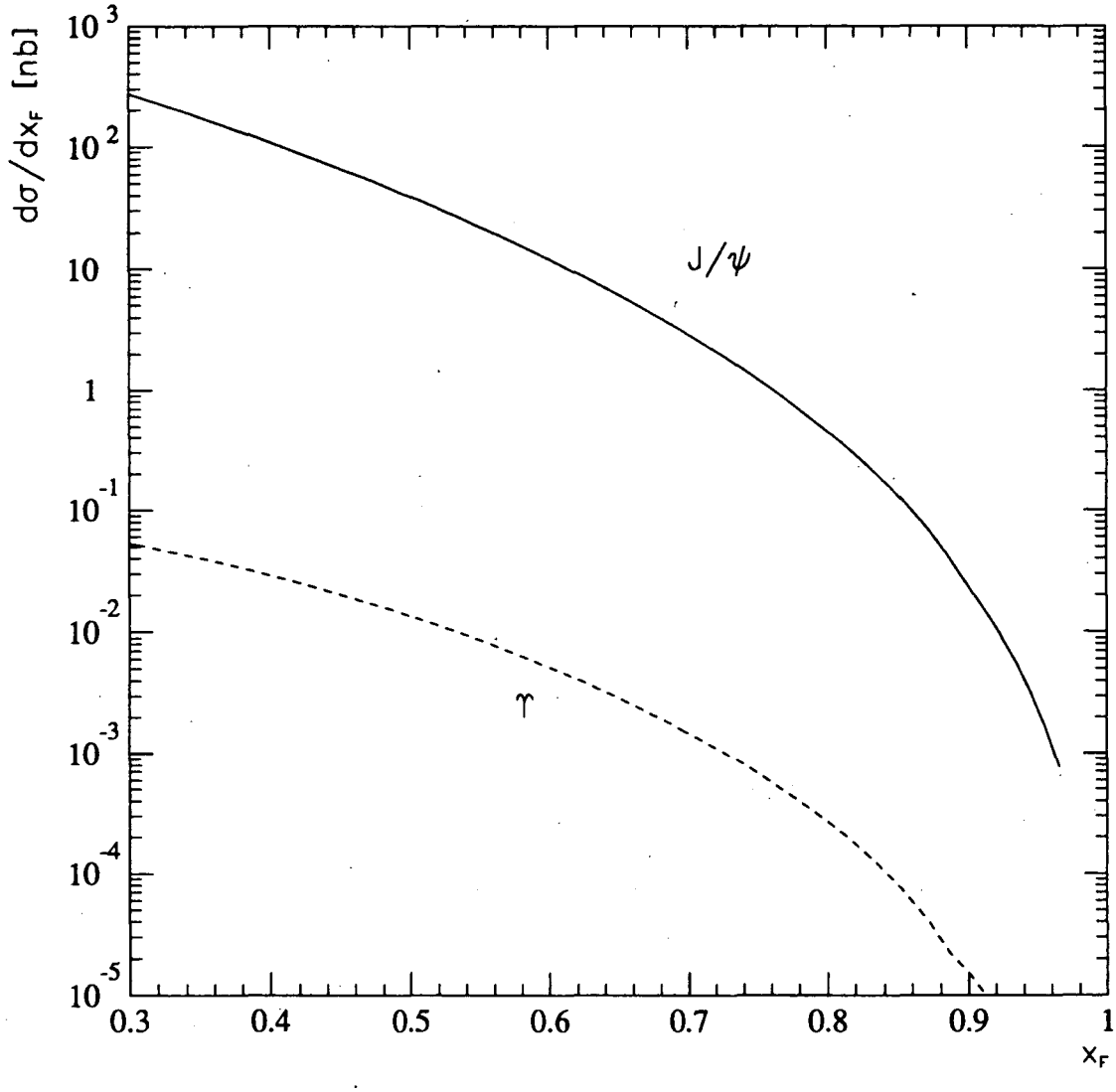

Figure 5.1: Semilocal parton duality prediction of J/ψ and Υ production by 800 GeV protons. Equation (1.8) was used to calculate the J/ψ production, with $m_c = 1.5$ GeV. For the Υ calculation, $m_b = 4.7$ GeV was used as the bare quark threshold, and $m_B = 5.28$ GeV was assumed as the open flavor threshold.

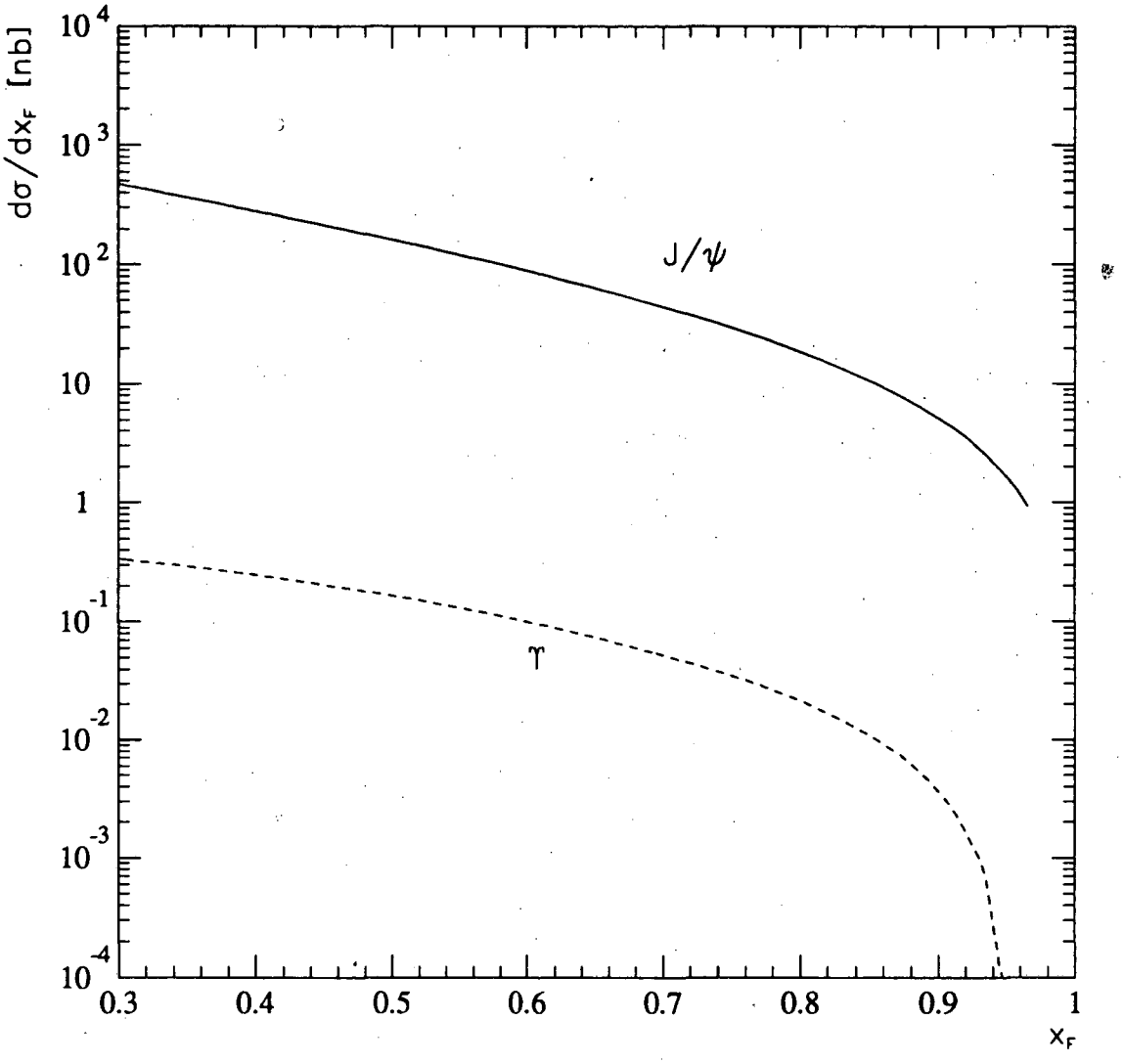

Figure 5.2: Semilocal parton duality prediction for J/ψ and Υ production by 1 TeV pions. The SMRS–P Set 2 pion structure functions was used, along with the MRS Set S0 structure function for the nucleon target. Equation (1.8) was used to calculate the J/ψ prodction, with $m_c = 1.5$ GeV. For the Υ calculation, $m_b = 4.7$ GeV was used as the bare quark threshold, and $m_B = 5.28$ GeV was assumed as the open flavor threshold.

REFERENCES

[1] J. J. Aubert *et al.*, Phys. Rev. Lett. **33**, 1404 (1974).

[2] J.-E. Augustin *et al.*, Phys. Rev. Lett. **33**, 1406 (1974).

[3] B. J. Bjørken and S. L. Glashow, Phys. Lett. **11**, 255 (1964).

[4] Robert N. Cahn and Gerson Goldhaber, *The Experimental Foundations of Particle Physics* (Cambridge University Press, Cambridge, 1989), Chap. 9, pp. 257–272.

[5] V. Barger, W. Y. Keung, and R. J. N. Phillips, Z. Phys. C **6**, 169 (1980).

[6] G. Altarelli and G. Parisi, Nuc. Phys. **B126**, 298 (1977).

[7] A. D. Martin, W. J. Stirling, and R. G. Roberts, University of Durham Preprint No. DTP/92/16 (1992).

[8] H. Plothow-Besch, "PDFLIB: Structure Functions and α_s Calculation User's Manual," CERN-PPE, 1992.07.22, W5051 PDFLIB (1992).

[9] Harald Fritzsch, Phys. Lett. **67B**, 217 (1977).

[10] Y. Lemoigne *et al.*, Phys. Lett. **113B**, 509 (1982).

[11] R. L. Jaffe (private communication).

[12] K. Hikasa *et al.*, "Review of Particle Properties," Phys. Rev. D **45**, Part 2 (June 1992).

[13] D. M. Alde *et al.*, Phys. Rev. Lett. **66**, 133 (1991).

[14] M. J. Leitch *et al.*, presented at the A.P.S. Division of Nuclear Physics meeting, Santa Fe, NM (1992).

[15] Jianwei Qiu, Nuc. Phys. **B291**, 746 (1987).

[16] R. Vogt, S. J. Brodsky, and P. Hoyer, Nuc. Phys. **B360**, 67 (1991).

[17] S. J. Brodsky *et al.*, Phys. Lett. **93B**, 451 (1980).

[18] S. J. Brodsky, C. Peterson, and N. Sakai, Phys. Rev. D **23**, 2745 (1981).

[19] S. J. Brodsky and P. Hoyer, Phys. Rev. Lett. **63**, 1566 (1989).

[20] R. Vogt (private communication).

[21] J. Badier *et al.*, Z. Phys. C **20**, 101 (1983).

[22] C. Biino *et al.*, Phys. Rev. Lett. **58**, 2523 (1987).

[23] J. S. Conway *et al.*, Phys. Rev. D **39**, 92 (1989).

[24] J. G. Heinrich *et al.*, Phys. Rev. D **44**, 1909 (1991).

[25] D. M. Alde *et al.*, Phys. Rev. Lett. **64**, 2479 (1990).

[26] D. M. Alde *et al.*, Phys. Rev. Lett. **66**, 2285 (1991).

[27] D. M. Kaplan and J. C. Peng, spokesmen, Fermilab Proposal 789, October 1988 (unpublished).

[28] C. N. Brown (private communication).

[29] D. M. Kaplan, "Introduction to the E605 Readout System," E605 Memorandum, 10 August 1982 (unpublished).

[30] T. A. Carey, P. M. Ho, and M. S. Kowitt, to be published.

[31] G. Moreno *et al.*, Phys. Rev. D **43**, 2815 (1991).

[32] R. Brun *et al.*, CERN Program Library Q121, PAW version 1.14 (1992).

[33] R. Brun and D. Lienart, CERN Program Library Y250, HBOOK version 4 (1988).

[34] G. Moreno, Ph.D. thesis, University of Mexico, 1989, (unpublished).

[35] E. J. Siskind *et al.*, Phys. Rev. D **21**, 628 (1980).

[36] A. S. Carroll *et al.*, Phys. Lett. **80B**, 319 (1979).

[37] A. J. Malensek, Fermilab Report FN-341/2941.0000, 12 October 1981 (unpublished).

[38] L. Lyons, Prog. Part. Nucl. Phys. **7**, 169 (1981).

[39] see, e.g., Donald H. Perkins, *Introduction to High Energy Physics,* 2nd ed. (Benjamin/Cummings, Menlo Park, California, 1982), pp. 311–316.

LAWRENCE BERKELEY LABORATORY
UNIVERSITY OF CALIFORNIA
TECHNICAL INFORMATION DEPARTMENT
BERKELEY, CALIFORNIA 94720